ANALYSIS AND FAULT TOLERANT CONTROL OF A FIVE-PHASE AXIAL FLUX PERMANENT MAGNET SYNCHRONOUS MACHINE

A THESIS SUBMITTED TO
THE GRADUATE SCHOOL OF NATURAL AND APPLIED SCIENCES
OF
MIDDLE EAST TECHNICAL UNIVERSITY

BY

GÖKSENİN HANDE BAYAZIT

IN PARTIAL FULFILLMENT OF THE REQUIREMENTS
FOR
THE DEGREE OF MASTER OF SCIENCE
IN
ELECTRICAL AND ELECTRONICS ENGINEERING

SEPTEMBER 2021

Approval of the thesis:

ANALYSIS AND FAULT TOLERANT CONTROL OF A FIVE-PHASE AXIAL FLUX PERMANENT MAGNET SYNCHRONOUS MACHINE

submitted by **GÖKSENİN HANDE BAYAZIT** in partial fulfillment of the requirements for the degree of **Master of Science in Electrical and Electronics Engineering Department, Middle East Technical University** by,

Prof. Dr. Halil Kalıpçılar
Dean, Graduate School of **Natural and Applied Sciences** _____

Prof. Dr. İlkay Ulusoy
Head of Department, **Electrical and Electronics Engineering** _____

Assoc. Prof. Dr. Ozan Keysan
Supervisor, **Electrical and Electronics Engineering, METU** _____

Examining Committee Members:

Assist. Prof. Dr. Emine Bostancı Özkan
Electrical and Electronics Engineering, METU _____

Assoc. Prof. Dr. Ozan Keysan
Electrical and Electronics Engineering, METU _____

Prof. Dr. Muammer Ermiş
Electrical and Electronics Engineering, METU _____

Assist. Prof. Dr. Taner Göktaş
Electrical and Electronics Engineering, Dokuz Eylül University _____

Prof. Dr. Hulusi Bülent Ertan
Mechatronics Engineering, Atılım University _____

Date: 06.09.2021

I hereby declare that all information in this document has been obtained and presented in accordance with academic rules and ethical conduct. I also declare that, as required by these rules and conduct, I have fully cited and referenced all material and results that are not original to this work.

Name, Surname: Göksenin Hande Bayazıt

Signature :

ABSTRACT

ANALYSIS AND FAULT TOLERANT CONTROL OF A FIVE-PHASE AXIAL FLUX PERMANENT MAGNET SYNCHRONOUS MACHINE

Bayazıt, Göksenin Hande
M.S., Department of Electrical and Electronics Engineering
Supervisor: Assoc. Prof. Dr. Ozan Keysan

September 2021, 138 pages

This study investigates the fault-tolerance capability of an air-cored, axial flux, five-phase permanent magnet synchronous machine. The air-cored stator is designed by adopting a novel winding topology that is called flat winding. The coils of flat winding are made by bending and grouping one within another of the flat wires made of a laser-cut thin aluminum sheet. This topology provides superior current ratings, better cooling performance, and a robust structure for the stator.

As the coils are covered with epoxy resin afterward, inter-turn short circuit risk, which is the most common stator fault in electrical machines, is completely eliminated. Therefore, in this study, the main focus is the analysis and mitigation of winding open-circuit fault. Another advantage of the proposed topology is its multiphase structure. The phase number, which is five, is chosen as an optimum point between minimum over-rating of phase currents in fault mitigation operation and the overall system complexity.

In the scope of this study, the design of a five-phase winding structure, analysis of

the sizing of the 1.4 kW, 26 Nm, 525 RPM machine are made. Analytical models for both healthy five-phase and open-circuit faulted four-phase machines are derived, and the simulation models for these drive operations are developed. Open-circuit fault mitigation strategies are investigated, and reduced-order Clarke transformation matrix method without third-order harmonic injection is adopted. On top of that, these analytical models and simulations are verified experimentally on the manufactured prototype. Closed-loop speed control is performed for normal and faulted operation modes with standard field-oriented control, using conventional PI controllers. Finally, it is concluded that the machine is advantageous for its robust structure, low electrical time constant. Still, niche measurement, acquisition devices and driver are necessary due to the air-cored machine's low phase inductance.

Keywords: fault tolerance, multiphase electric machine, permanent magnet synchronous machine, axial-flux, air-cored stator, five-phase, field-oriented control, open circuit fault, fault remedial strategies

ÖZ

BEŞ FAZLI EKSENEL AKILI SABİT MIKNATISLI SENKRON MAKİNENİN ANALİZİ VE HATA TOLERANSLI KONTROLÜ

Bayazıt, Göksenin Hande
Yüksek Lisans, Elektrik ve Elektronik Mühendisliği Bölümü
Tez Yöneticisi: Doç. Dr. Ozan Keysan

Eylül 2021 , 138 sayfa

Bu çalışma, hava nüveli, eksenel akılı, beş fazlı sabit mıknatıslı senkron bir makinenin hata tolerans kapasitesini araştırmaktadır. Hava nüveli stator, yassı sargı adı verilen yeni bir sarım topolojisi benimsenerek tasarlanmıştır. Yassı sargı bobinleri, lazerle kesilmiş ince bir alüminyum levhadan yapılmış yassı tellerin bükülmesi ve birbiri içinde gruplandırılmasıyla yapılır. Bu topoloji, stator için yüksek akım taşıma kapasitesi, daha iyi soğutma performansı ve sağlam bir yapı sağlar.

Bu topolojde bobinler epoksi reçine ile kaplandığı için elektrik makinelerinde en sık görülen stator arızası olan sargılar arası kısa devre riski tamamen ortadan kalkar. Bu nedenle, bu çalışmada ana odak, sargı açık devre arızasının analizi ve azaltılmasıdır. Önerilen topolojinin bir başka avantajı da çok fazlı yapısıdır. Bir açık devre arızası durumunda, geleneksel üç fazlı makinelerden farklı olarak, kalan sağlıklı fazlar ile düşük dalgalı çıkış torku oluşturmak mümkündür. Beş olan faz sayısı, arıza azaltma işleminde faz akımlarının minimum aşımı ile genel sistem karmaşıklığı arasında optimum bir nokta olarak seçilir.

Bu çalışma kapsamında beş fazlı bir sargı yapısının tasarımı, 1.4 kW, 26 Nm, 525 rpm makinenin boyutlandırma analizi yapılmıştır. Hem sağlıklı beş fazlı hem de açık devre arızalı dört fazlı makineler için analitik modeller türetilmiş ve bu sürüş sistemleri için simülasyon modelleri geliştirilmiştir. Açık devre arıza azaltma stratejileri araştırılmış ve üçüncü dereceden harmonik enjeksiyon olmadan indirgenmiş dereceli Clarke dönüşüm matrisi yöntemi benimsenmiştir. Bunlara ek olarak, bu analitik modeller ve simülasyonlar, GaN tabanlı bir evirici tarafından sürülen prototip üzerinde deneysel olarak doğrulanmıştır. Kapalı çevrim hız kontrolü, geleneksel PI kontrolcüleri kullanılarak standart alan yönlendirmeli kontrol ile normal ve hatalı çalışma modları için gerçekleştirilmiştir. Son olarak, makinenin sağlam yapısı, düşük elektriksel zaman sabiti sebebiyle avantajlı olduğu sonucuna varılmıştır. Yine de, hava çekirdekli makinenin düşük faz endüktansı nedeniyle niş veri ölçümü ve toplama cihazları ve yüksek kapasiteli sürücü devresi ile motor kontrolü kolaylaştırılabilir.

Anahtar Kelimeler: hata toleransı, çok fazlı elektrik makinesi, sabit mıknatıslı senkron makine, eksenel akı, hava nüveli stator, beş fazlı, alan yönlendirmeli kontrol, açık devre hatası, hata düzeltme stratejileri

To my dear parents, Leyla and Yıldırım

and

in the loving memory of my dear friend Oytun

ACKNOWLEDGMENTS

I would like to begin my words with an apology in advance, in case I forget to mention anyone that deserves a credit with a quote by J. R. R. Tolkien: “I don’t know half of you half as well as I should like; and I like less than half of you half as well as you deserve.”

First of all, I would like to thank my supervisor, Dr. Ozan Keysan. Amazed by his excellent teaching skills and kind personality as a junior undergraduate student, I started following the (EE361) lectures more carefully and realized that I belonged here. If I hadn’t met him, I probably wouldn’t have chosen to work in this field. I thank him for encouraging me, guiding me and teaching me how to be a better researcher at that time. I thank him for accepting me as an M.Sc. student, including me among PowerLab, which is an invaluable opportunity for my academic growth by letting me work with many extraordinary people doing fantastic stuff collaboratively. I also thank him for his guidance and his notable suggestions in preparation of this thesis.

The biggest of the thanks goes to Dr. Emine Bostancı. She had always time for me whatever and whenever I needed. The completion of this thesis would be impossible without the technical/non-technical discussions we have made and without her guidance. I might have treated her as the Wailing Wall most of the time, but her solutions, suggestions, counsel and help made the hardest times bearable. She is so smart, helpful, cheerful, wise, full of joy and love. I am extremely lucky to have met and worked with someone like her. I know that she will not remain a former advisor of mine, but a dear friend instead.

A huge appreciation is for Gökhan; for sharing his knowledge, his design so that I can modify it for my research topic. While we were working on the manufacturing steps of our prototypes (poor Gökhan had already built two of them at that time), Gökhan was always telling me that the next step of the production was easier and more

enjoyable. Gökhan, none of these steps were easy or enjoyable but your company truly was :) All the procedure would have been nothing but a hassle without your help and effort. I wish you all the best in your future life and the success that you deserve.

Another colleague that I am truly grateful is Furkan (Karakaya). While I was desperately looking for a commercial driver for my motor, he offered to make one (which was in fact similar to the one he designed for his thesis), just voluntarily and gratuitously. He guided me through the power electronics part throughout my experiments, he always had answers and time for my problems. He is the person that I am amazed the most, for his knowledge, his research enthusiasm and his discipline. I am sure he will do anything he wants in the future, and he will be extremely successful without a shadow of doubt. He deserves to.

Özgür (or rather Zgryzc), I should cut my diploma in four and give one quarter of it to you. He is one of the most brilliant people I know, probably the person with the best intuition: so good that continuously re-inventing already invented things by himself :) I'm grateful to him for always explaining me what I didn't understand, helping me with the debugging; as well as for our "trash movie trash food" nights, for never asking the question with the eagles and for being a true Frodo hater. Özgür is an incredible person and an amazing friend, my time in the office wouldn't be the way as it is without him.

It was so great to be a part of PowerLab. I want to express my gratitude to every former and current member of PowerLab, and in particular to Barış, Yusuf, Furkan (Tokgöz), Nail and Enes. I really enjoyed every moment we spent together, and I'm grateful for their support both as colleagues and as friends. I also want to thank Hakan (Saraç) for helping me with the introduction to embedded programming. I couldn't complete the coding part in such a short time without him telling me the key points and his help with the code debugging. Another person that I bombarded with questions is (S)İlker Hocam. I also thank him for our technical/non-technical chats in the lab and in the office. It was so great to know someone like him, who is the only one of his kind.

Some heroes don't wear capes. I can't thank Ekin (Tanır) enough for helping me out

with the transistor supply, in the middle of the lockdown. I wish her the best for her future career and goals. Likewise, a huge appreciation is for our technicians Mesut Abi, Mehmet Ali Abi and Bünyamin Abi for their help with the lab equipment and with the mechanical parts. Also, a heartfelt thank you to my old friends İsot and Emre (Doğan), and to my not-so-old friend Zafer for their support, encouragement and for being with me.

I cannot forget four of my dearest friends, who have been my lovely companions at least for some part of this journey. Of course, this paragraph is for my cats. Mia, the princess, the precious; thank you for turning me into a hopefully-not-crazy-cat-lady, and thank you for accompanying mom and dad at home, in my absence. Robin and Rümo, the double trouble; you were the most incredible duo that I could've ever met. I still miss you, you will always be in my heart. Küçük Sümo; thank you for your company for all this time. You made my time in the office more enjoyable and the most problematic times bearable. Keep up with the good work in Eindhoven too. The Flying Dutchcat Sümo.

This paragraph is for someone that my words fall short to express my gratitude. Someone who has been by my side (literally) since day one, someone who has always doubled my cheers and dashed away my tears, someone who has always been my greatest support while I was sitting in the lab, in the office, in front of the C building with questions in my mind and with a "sweet smile of pain" on my face. He is the most helpful and generous person that I have known and will ever know: he didn't hesitate helping me with the mysterious problems of the experimental setup while he was supposed to study for the Qualification Exam, and he didn't give up until he solved them! Mehmet, another quarter of the diploma is for you :) I feel extremely lucky that our paths have crossed, it is horrible even to think of the things I would miss, if they wouldn't. I'm grateful for every moment we spent together, every good and bad things we've been through. You're irreplaceable.

The last personal, and probably the most emotional paragraph (because you always hug the most loved ones at the very end) will be in Turkish, so that its collocutors can fully comprehend my thoughts and feelings. Canım anneciğim, canım babacığım; teşekkürlerin, takdirlerin ve minnetin en büyüğünü siz hak ediyorsunuz. Hayatta

her zaman beni önceliklerinizde en öne koydunuz, bütün planlarınızı benim en iyi/mutlu olacağım şekilde yaptınız. Neredeyse tüm gücünüzü, emeğinizi benim iyi yürekli, düzgün, özgür, bağımsız ve mutlu bir insan olabilmem için harcadınız ve yeri geldiğinde çokça fedakarlık yaptınız. İnsanın hayatta başına ne gelirse gelsin, iyi ve kötü zamanlarda, her koşulda arkasında sizin gibi iki kişinin desteğini esirgemeyeceğini bilerek yaşaması büyük bir şans, büyük bir güven. Bugün ben burada tam olarak ne yaptım bilmiyorum, yaptım bir şeyler, sanırım güzel bir şeyler. Bugüne kadar güzel ne yaptıysam, ileride güzel ne yapacaksam, bilin ki bu sizin sayenizdedir. Her şey için minnettarım, iyi ki varsınız, ikinizi de çok seviyorum. (*Eng.* Dear mom, dear dad; you deserve the greatest of thanks, appreciation and gratitude. You always put me at the top of your priorities in life, you made all your plans in a way that would make me my best and make me happy. You spent almost all your strength and effort to make me a good-hearted, decent, free, independent and happy person, and you sacrificed a lot where necessary. It is a great chance, a great confidence to live knowing that no matter what happens in my life, in good and bad times, under any circumstance, you will always be my greatest support. I don't know exactly what I did here today, I did something, I think I did something nice. Whatever I have done well until today, and what I will do well in the future, keep in mind that it is thanks to you. Thank you for everything, I'm glad to have you, I love you both so much.)

I also thank The Scientific and Technological Research Council of Turkey for their financial support during my graduate studies.

As a closure, I should acknowledge that I believe, as a Turkish woman engineer and scientist, I owe a deep gratitude to M. Kemal Atatürk. I have been and will be a well-educated, free and independent woman; and will be a scientist thanks to his visionary and egalitarian revolutions. Until now and till the end, science has been and will always be my truest guide in life.

This thesis is dedicated to my dear parents and to Oytun, whom I lost last summer, who was one of my closest friends and a great support during my undergrad years. May his soul rest in peace.

TABLE OF CONTENTS

LIST OF TABLES

TABLES

LIST OF FIGURES

FIGURES

LIST OF ABBREVIATIONS

1-Ph	Single-Phase
4-Ch	Four-Channel
5-Ph	Five-Phase
ADC	Analog to Digital Converter
AFPMSM	Axial Flux Permanent Magnet Synchronous Machine
DAC	Digital to Analog Converter
DC	Direct Current
DPT	Double Pulse Test
DSP	Digital Signal Processor
EMF	Electro-Motive Force
FOC	Field-Oriented Control
FTC	Fault Tolerant Control
HEMT	High-Electron-Mobility Transistor
IDE	Integrated Development Environment
ITSC	Inter-turn Short Circuit
MMF	Magneto-Motive Force
MPC	Model Predictive Control
OCF	Open Circuit Fault
PM	Permanent Magnet
PMSM	Permanent Magnet Synchronous Machine
PWM	Pulse Width Modulation
SMPM	Surface Mount Permanent Magnet
SPWM	Sinusoidal Pulse Width Modulation
THI	Third Harmonic Injection

LIST OF VARIABLES

P_{rated}	Rated power
T_{rated}	Rated torque
N_{rated}	Rated mechanical speed
V_{line}	Line-to-line voltage
I_{line}	Line current
r_i	Inner radius of the rotor
l_{yoke}	Length of the rotor yoke
l_g	Length of each air-gap
l_s	Thickness of the stator
l_{tot}	Total length of the machine in axial direction
l_m	Thickness of each magnet
μ_r	Relative permeability of the rotor steel
μ_s	Relative permeability of the stator
μ_m	Relative permeability of the magnets
μ_g	Relative permeability of the air-gap
$\mathcal{R}_r$	Reluctance of each rotor
$\mathcal{R}_s$	Reluctance of each the stator
$\mathcal{R}_m$	Reluctance of each magnet
$\mathcal{R}_g$	Reluctance of each air-gap
ϕ_r	Residual flux due to the magnets
B_r	Residual magnetism
H_c	Coercivity of the magnets
$\widehat{B}_{\delta,1}$	Peak fundamental flux density in the air-gap

$\widehat{B}_{\delta,3}$	Peak third order flux density in the air-gap
$\widehat{B}_g$	Peak flux density in the air-gap
k_{leak}	Leakage flux factor
k_{mag}	Magnet to pole area ratio
$\widehat{A}_1$	Electric loading due to fundamental current
$\widehat{I}_1$	Peak fundamental phase current
N_{tot}	Total number of turns
k_w	Fundamental winding factor
r_{mean}	Mean radius of the rotor
σ_{tan}	Tangential stress
T	Output torque / Product of Clarke and Park transformation matrices
P	Output power / Number of pole pairs
S_{rot}	Surface area of the rotor
E_1	Fundamental phase induced EMF
ω, ω_e	Electrical speed
$B_{\delta,1}$	Fundamental flux density in the air-gap
$\widehat{E}_1$	Peak fundamental phase induced EMF
L_s	Stator inductance matrix
L_l	Leakage inductance
L_{XX}, L	Self inductance of phase X
L_{XY}, M_1	Mutual inductance between phase X and Y (two adjacent phases)
L_{XZ}, M_1	Mutual inductance between phase X and Z (two non-adjacent phases)
$N_X(\phi)$	Winding function of phase X
N	Number of turns per phase
L_{m1}	Fundamental magnetizing inductance
$\vec{B}$	Magnetic flux density vector

λ_{PM}	Flux linkage due to PMs
R_s	Phase resistance, resistance matrix
v_X	Input voltage of phase X
i_X	Line current of phase X
λ_X	Flux linkage of phase X
$\boldsymbol{V_s}$	Input voltage vector
$\boldsymbol{I_s}$	Line current vector
$\boldsymbol{\Lambda_s}$	Total flux linkage vector
$\boldsymbol{\Lambda_{ss}}$	Flux linkage vector due to winding inductances
$\boldsymbol{\Lambda_{PM}}$	Flux linkage vector due to PMs
$\boldsymbol{X}^t$	Transpose of X vector / matrix
θ_r, θ	Electrical position of the rotor
$i_{\alpha 1}$	Fundamental current on the α axis
$i_{\alpha 3}$	Third order current on the α axis
$i_{\beta 1}$	Fundamental current on the β axis
$i_{\beta 3}$	Third order current on the β axis
i_{d1}	Fundamental current on the direct axis
i_{d3}	Third order current on the direct axis
i_{q1}	Fundamental current on the quadrature axis
i_{q3}	Third order current on the quadrature axis
i_0	Zero-space current
T_c	Clarke transformation matrix
T_p	Park transformation matrix
$\boldsymbol{I_{\alpha\beta}}$	$\alpha\beta$ current vector
$\boldsymbol{I_{dq}}$	DQ current vector
L_d	Inductance on the direct axis
L_q	Inductance on the quadrature axis

W'	Magnetic co-energy
$\boldsymbol{\Lambda_{dq}}$	DQ flux linkage vector
λ_{d1}	Fundamental flux linkage on the direct axis
λ_{d3}	Third order flux linkage on the direct axis
λ_{q1}	Fundamental flux linkage on the quadrature axis
λ_{q3}	Third order flux linkage on the quadrature axis
T_{mech}	Shaft torque
ω_{mech}	Shaft speed in rad/sec
P_{out}	Output power
P_{in}	Input power
V_{bus}	DC bus voltage
I_{bus}	DC bus current
η	Efficiency
t	Time
V_n, v_n	Voltage of the neutral point
i'_X	Line current of phase X when the machine is under OCF / is under FTC operation
i'_{X3}	Third harmonic current of phase X when the machine is under FTC operation
$\boldsymbol{I_{s1}}$	Phase current vector before the machine is under OCF
$\boldsymbol{I_{s2}}$	Phase current vector after the machine is under OCF
I_{peak}	Peak phase current
$\boldsymbol{V_n}$	Voltage vector of the neutral point
$\mathbb{Z}$	Impedance matrix
$\mathbb{Z}_1$, $\mathbb{Z}_2$	Impedance sub-matrices
$\boldsymbol{I_f}$	Fault current vector
$\boldsymbol{E}$	Phase difference vector
$\mathcal{F}$	MMF

$\mathcal{F}_X$	MMF due to phase X current
$\mathcal{F}_i$	MMF before the machine is under OCF
i_{z1}	Third space current vector
$i_{\alpha\beta 1}$	Fundamental $\alpha\beta$ current vector
$i_{\alpha\beta 3}$	Third order $\alpha\beta$ current vector
$T_{C1_{FTC}}$	Fundamental Clarke transformation matrix for FTC operation
$T_{C3_{FTC}}$	Third space Clarke transformation matrix for FTC operation
T_{e1}	Electrical torque due to fundamental components
T_{e3}	Electrical torque due to third order components
λ_{m1}	Fundamental flux linkage due to magnets
λ_{m3}	Third order flux linkage due to magnets
e_X	Induced EMF of phase X
I'_X	Remedial current of phase X
x	Reference phase angle
$T_{C,gen}$	Generalized Clarke transformation matrix for FTC operation
K_p	Proportional coefficient of PI controller
K_i	Integral coefficient of PI controller

CHAPTER 1

INTRODUCTION

Electric machines have widely been used for electric power generation, industrial and domestic applications since they were invented. Mainly for industrial applications, with an increasing number of automated systems, pneumatic and hydraulic systems are being replaced with electric drives, due to their better and faster controllability. Consequently, the reliability of electric drive systems gains importance because of their wide use of safety-critical industrial applications such as aviation, military systems, power generation and automotive. In a general sense, under fault occurrence, such electric drive systems should be able to maintain near-proper operation and its elements should be resistant to possible irreversible damages caused by system failures. This concept is called fault tolerance and such electric drives are named as fault tolerant drives [6, 7].

Besides, the use of electric drives in a wide range of application domains requires the design and adoption of machine topologies with various characteristics. For example, traction drives are required to be compact, reliable and efficient. They are designed with high torque and torque density concerns and they are expected to operate in a wide speed range. As another example, wind turbine generators operate at low speed and high torque, where some other industrial applications require a drive operation at high speed and lower torque production. Further examples may be cited.

For industrial systems that require higher torque and lower speed, axial flux machines are a preferred choice over radial flux ones thanks to their large diameter and higher torque densities. On top of that, adopting an air-cored structure for axial flux machines introduces further benefits such as decreased structural mass and reduced cogging torque for possible industrial systems. However, there are few studies on the

reliability and fault tolerance of air-cored axial flux machines that may be possibly used in safety-critical applications. These studies usually tackle the more commonly used radial flux machine and iron-cored topologies.

Considering the mentioned gap in the electrical machinery literature and with the intent of filling this gap, this study investigates the fault tolerance of an air-cored axial flux permanent magnet synchronous machine with a novel winding topology, by means of both the design and the control of it.

The outline of this thesis can be summarized as follows:

- **Chapter 2:** This chapter covers the previous work related to this study in the literature. The main subjects which will be discussed in the literature review are fault tolerance in electric drives, redundant and/or multiphase drive systems, axial flux machines and air-cored machines. Also, their advantages and disadvantages will be stated whenever applicable.
- **Chapter 3:** This chapter will present an axial flux machine design with a novel winding topology. This winding, which is composed of flat aluminum wires, has prominent characteristics such as short circuit protection, high current carrying capability and easy manufacturing process. Another feature of the machine is its multiphase structure. The design procedure of the machine will also be explained in this chapter. The proposed design is simulated and validated using finite element modeling. Finally, the experimental results of the manufactured machine prototype will be presented and compared with the analytically and numerically found results.
- **Chapter 4:** This chapter will summarize the analytical modelling procedure of a five-phase electric drive. Initially, the variables and equations of the five-phase drive will be introduced. After that, the simulation results of a five-phase drive model that is built based on the analytical model will be given. Finally, the experimental results of the five-phase machine that operates in motoring mode under different operating conditions will be shown and both results will be discussed.
- **Chapter 5:**This chapter will mainly focus on open circuit fault of one phase

in the five-phase machine. As an introduction, the currents drawn by healthy phase windings when the machine is under an open circuit fault will be analytically obtained. Following that, fault mitigation strategies will be discussed. Conventional methodologies that had been proposed for open circuit fault recovery will be given and an alternative and easier method to determine the remedial phase currents will be presented. Also, the modifications that should be made on the control loop will be discussed. Similar to the Chapter 4, these control strategies will be applied on the drive simulation model and the machine prototype. Both results will be compared and the incompatible results will be discussed.

- **Chapter 6:** This chapter will summarize the findings of this study, will present the conclusions of the research. Also, further possible improvements on the study, experimental setup and the control approach will be presented.

CHAPTER 2

LITERATURE REVIEW

This chapter provides information about recent studies in electrical machinery. The selected topics in this chapter are mainly focused on fault tolerant drives and fault tolerance concept of electrical machines, axial flux electrical machines and ironless topologies. Throughout the chapter, the research topics have been mainly described, some previous work in the area have been summarized and the compared topologies/-concepts have been discussed.

2.1 Fault Tolerant Electric Drives

Faults may arise from different sources in electric drive systems, some of which are bearing faults, demagnetization of PMs, inverter faults and stator-related open circuit and short circuit faults. Possible faults in an electric drive are presented in the schematic given in Figure 2.1. Considering that an electric drive is a whole of numerous components, each component of the drive introduces its own failure risk that could violate the functional reliability of the system. To eliminate the effect of sensor failures, observer design [8,9] and to eliminate the effect of inverter leg faults, adding redundant legs or parallel switches to the system [10] are adopted methodologies for the sake of a reliable electric drive.

Looking from the electrical machine perspective, the failure types According to [11], stator-related faults in electrical machines has the second largest percentage, 36%, among all failure types. This ratio increases up to 65% as the rated voltage of the machine increases. Stator-related faults can mainly be classified as open and short-circuit faults, as given in Figure 2.1. In [12–14], it is stated that most of the short

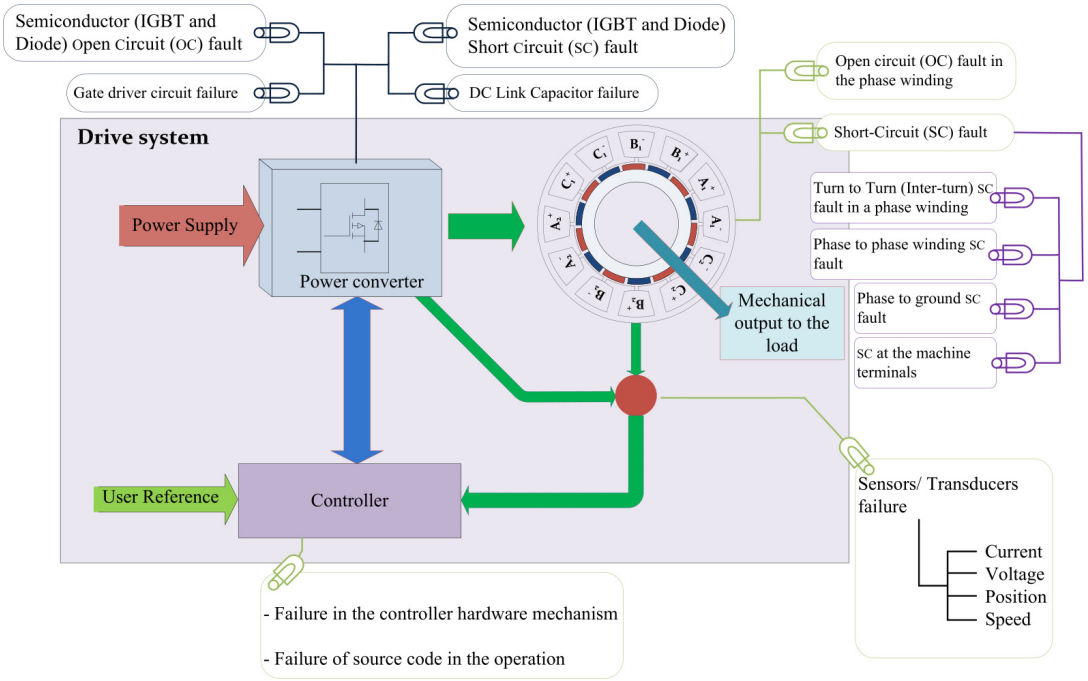

Figure 2.1: Fault Types in an Electric Drive System (retrieved from [1])

circuit faults start with a turn-to-turn (interturn) short circuit (ITSC) fault and then propagate to the whole winding [2]. The main reason for this fault is the thermal and electrical stress on the winding isolation. Continuous inverter switching, poor cooling and resultant high temperature operation are harmful for the winding. Some example short-circuit types are shown in Figure 2.2.

Aging of the isolation leads to ITSC fault especially in stranded windings. An alternative topology for this issue is hairpin winding. It is invented with the motivation of increasing the fill-factor and automatizing the manufacturing process [15–17]. Its basic structure and the difference between the conventional stranded winding and preformed hairpin winding are given in Figure 2.3. On top of its design motivation, its solid structure also less prone to generate an ITSC, when the isolation between the coils are thick enough [18].

When a short circuit occurs in a coil, large amount of inrush currents flow through it [14]. This is the main reason of the spread of one-turn ITSC to a whole phase winding as exponential growth. Therefore, the most common strategy in these studies is:

- The detection of the ITSC fault,

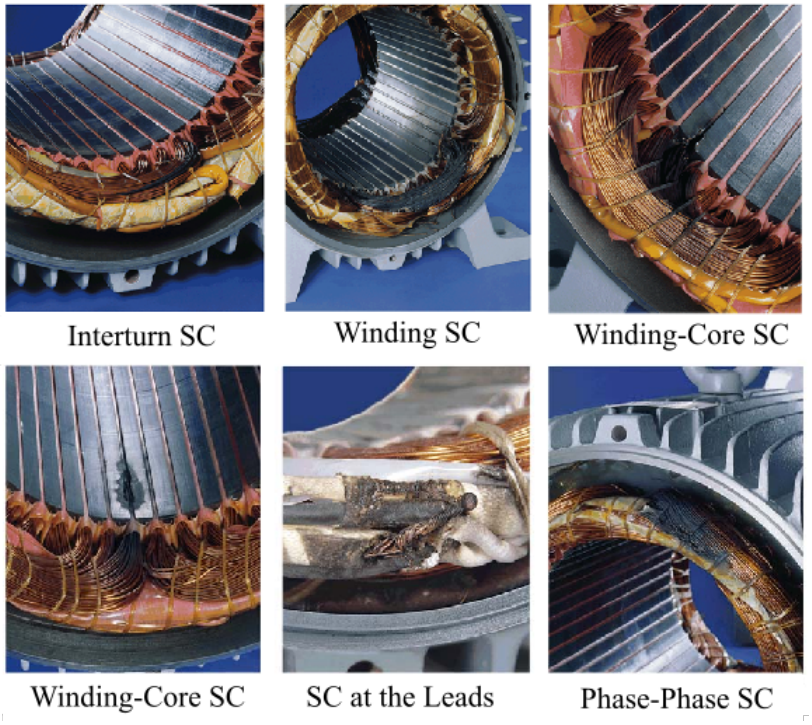

Figure 2.2: Short Circuit Fault Types in the Stator of a Machine (retrieved from [2])

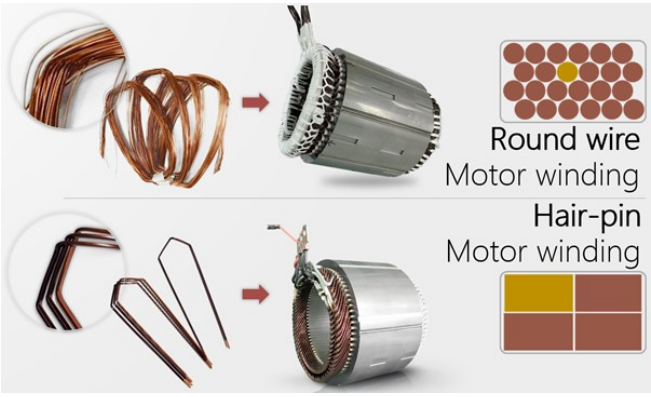

Figure 2.3: The Structure of Hairpin Winding (retrieved from [3])

- Deactivating the phase on which the fault occurs,
- (Optional) Short-time operation of the drive by following one of the various open circuit fault mitigation strategies.

Consequently, to be able to act upon this, the design of the machine should satisfy several conditions. In other words, a machine can be called as "fault tolerant" if it has the following features [19, 20]:

- **Electric isolation between phases:** Electrical isolation of the phase windings ensures the ability to control each phase separately and eliminates the flow of fault currents through healthy phases. Removal of the star connection and a driver composed of separate bridges are example solutions for this condition.
- **Magnetic isolation between phases:** To decrease the effect of the fault current on healthy phases, magnetic coupling between them should be low.
- **Mechanical isolation between phases:** The coils should be physically apart from each other, in order to prevent the spread of a fault to the other phases. The term "mechanical isolation" includes both physical and thermal constraints. Tooth wound coil is a good example that satisfies this criterion.
- **Limiting the Fault Current:** To prevent the large currents that could give damage to the system, phase inductance of the machine should be high.
- **Redundancy:** This is the main concept between modular and multiphase topologies. Stator modularity and number of phases larger than three introduces redundancy to the system. Thus, the machine can pursue its near-proper operation under fault conditions.

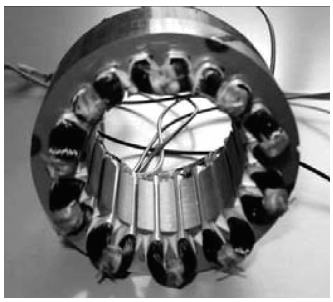

(a) Five-Phase (retrieved from [21])

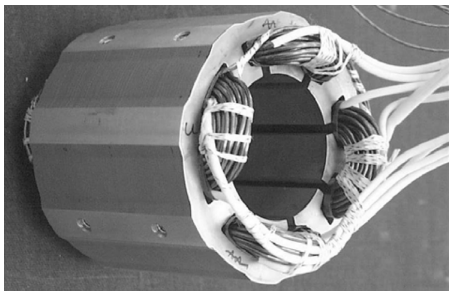

(b) Four-Phase (retrieved from [22])

Figure 2.4: Examples of Fault Tolerant Stator Winding Structure

Two example stator topologies that hold the abovementioned criteria are given in Figure 2.4. Both of these stators are composed of tooth windings. That is, the span of the coils are one tooth and they do not touch each other. The winding design for both are made to make sure that the magnetic coupling between phases are minimized.

Furthermore, phase numbers are chosen as four (in Figure 2.4a) and five (in Figure 2.4b) to provide the redundancy to the system.

2.2 Multiphase Electrical Machines and Modularity Concept

As a result of the redundancy concern in electrical machines, multiphase (which is a term that covers the phase numbers larger than 3) and modular electric machines have gained wide research interest recently. Many studies have been conducted on various machine types, such as induction machine, PMSM, synchronous reluctance and switched reluctance machines. The previous research on multiphase drive systems have been extensively reviewed in [23, 24] by means of general advantages, modeling methods, control methods, fault tolerance and suitable application areas. Major asset of the multiphase structure is the ability to carry less power per phase for the same total amount compared to a three-phase machine. Also, fault tolerance capability and torque enhancement capability using higher-order harmonics are some other benefits of these structures.

The multiphase machine studies on different phase numbers, as well as their advantages and drawbacks can be summarized as follows:

- **Even phase number:** Even phase number is usually not preferred in fault tolerance perspective. The main reason for that is as an open circuit fault occurs or a phase is deactivated after a short circuit fault, the system becomes asymmetrical for an even-phase-numbered system [25]. That is why, in most of the studies, phase numbers are selected as odd numbers. However, there are also several advantages of even-numbered systems.
  - **Four-phase** [21]: Four-phase machines are considered to have an extra phase leg for failure conditions. This selection brings the redundancy, as well as its drive complexity is less compared to its higher-phase-numbered alternatives.
  - **Six-phase** [26–28]: Six-phase machines have symmetrical and asymmetrical versions. The major advantage of the six-phase machines is the ability to use conventional three-phase inverters to drive the motor. Usually,

they are configured as two set of three-phase windings. Fault remedial strategies are applied by utilizing this modular structure on these topologies.

- **Odd phase number:** When the phase number is selected as an odd and prime number, the machine can be driven in fault remedial modes, as well as its output torque can be enhanced with higher order flux linkage and current harmonics.
  - **Five-phase** [29–32]: Five is an optimum number for phase number selection. Hence there are numerous studies that investigate the properties of five-phase machines. In addition to its two redundant phases, ability to produce torque with third-harmonic flux linkage is a major asset of five-phase machines. Furthermore, compared to seven-phase topologies, its driver and control structure are less complex and contain fewer switches.
  - **Seven-phase** [33]: Seven-phase machines hold similar advantages to that of five-phase machines. However, increased number of switches in the seven-phase inverter and complex control structure are the drawbacks of this phase number selection.

Other than multiphase machines, modular machine types are also a good alternative to provide the redundancy to the system. Especially for safety-critical applications such as transportation, modular machines and motor drives have been a popular research area. Some of these studies also propose combining the drive and the machine in the same package to obtain a more compact form that is suitable for mobile applications (this structure is called "integrated modular motor drive (IMMD)") [34–36]. Thanks to the partitioned topology of the machine and its partitioned inverter structure, it is possible to turn a module off completely in case of a fault occurrence and maintain derated operation with the remaining modules.

2.3 Comparison of Radial and Axial Flux Machines

The history of axial flux machine is older than the radial flux machine. In 1821, Faraday invented a disc-shaped machine which can be considered as the first axial

flux machine. 15 years later, Davenport obtained a patent for a radial flux topology. Since then, radial flux has become the conventional structure for electrical machines [37].

Axial flux is named after its flux passing direction. Figure 2.5 shows the basic structure and flux passing directions of the radial and axial flux machines.

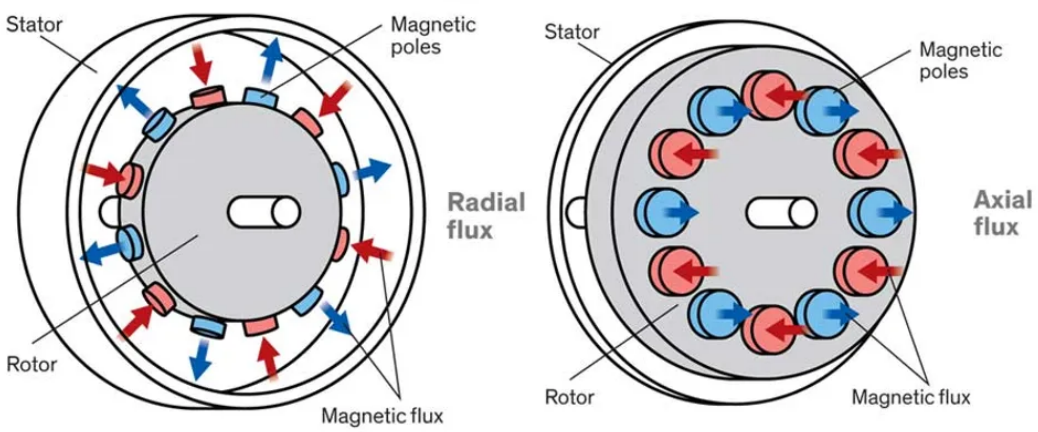

Figure 2.5: Comparison of Radial and Axial Flux Machines (retrieved from [4])

The prominent features of axial flux machines compared to radial flux machines based on the research in [5, 38–40] can be summarized as follows (The sign "**+**" stands for an advantage, where "**-**" stands for a disadvantage) :

+ Axial flux machines are more suitable for high torque low-speed applications thanks to their large diameter and capability to accommodate large pole numbers.

+ Axial flux machines have higher torque densities compared to their radial flux equivalents.

+ Axial flux machines can be stacked in axial direction. This introduces modularity and redundancy to the overall system and is favorable in the sense of fault tolerance.

- Because of its shape with large diameter, the machine can deflect due to the electromagnetic forces and rotation speed. This deflection may cause an uneven

air gap, which would result in a high torque ripple. Over time, the torque ripple may increase the mechanical stress on the bearings and may cause mechanical failure of the machine.

Axial flux machines have several different configurations based on their rotor/stator numbers and their placement order in axial direction. The stator of a machine that is composed of a single rotor and a single stator would get deflected over time because of the non-zero net force in the axial direction [5]. However, this would not be the case for the structures that are symmetrical in axial direction (such as double rotor or double stator topologies). Therefore these types of axial flux machine topologies are more preferred in the related studies.

2.4 Air-Cored Machines

In electric machines the stator material is conventionally chosen as steel to provide a smaller air gap and hence a magnetically less reluctant system. However, there are several disadvantages of iron-cored machines such as stator core loss, high total mass and cogging torque due to the slotting effect of the stator. These drawbacks of iron-cored topologies prompted to study on a different alternative, which is air-cored (also known as "coreless") machine [40–43].

The comparison between iron and air-cored machines by speaking of their major assets and drawbacks can be summarized as follows (The sign "**+**" stands for an advantage, where "**-**" stands for a disadvantage):

- **+** Air-cored machines produce less (and generally no) cogging torque since the stator is slotless and magnetically insalient.
- **+** Air-cored machines have less magnetic loading in the air-gap. Therefore, they almost never saturate. Resultantly, the machine parameters can be considered and modeled as linear parameters [40].
- **+** As the stator of the machine is not a ferromagnetic material, there will be no core losses in the stator of the machine.

+ Low magnetic loading also causes less deflection of the rotor core for axial flux machines. Therefore the mechanical structure elements of the machine that are supposed to keep the air gap at a constant value are less. This also decreases the overall mass of the machine.

+/- Air-cored machines have large effective air gap, high magnetic reluctance, hence; low inductance. Low inductance is an advantage by means of higher power factor, but also makes the control of the machine difficult.

CHAPTER 3

PROPOSED TOPOLOGY: DESCRIPTION AND THE CONSTRUCTION OF THE MACHINE AND THE MOTOR DRIVER

This chapter presents the proposed motor drive topology. Initially, the main motivation of adopting this air-cored axial-flux PMSM topology will be explained. The structure's assets and drawbacks will be discussed. The physical structure of the motor, and the novel flat winding design will be introduced and explained in detail. Also, the GaN-based inverter will be presented. The motor driver is built specifically for this five-phase machine.

After explaining the general structure of the five-phase motor drive of proposal, the design steps of the electrical machine will be revisited and its magnetic design will be verified, analytically. On top of that, these analytical calculations will be validated using finite element analysis. The matching and incompatible results will be discussed and compared.

Finally, the experimental results for the electric machine operating in generator mode and the inverter feeding an RL-load will be presented. The main purpose of these experiments are to show that the manufactured prototypes operate properly. That is, the design of the five-phase motor drive components have been successful, and the drive system is suitable for integration.

3.1 Motor Topology

In Section 2, the advantages of axial flux machines over radial flux machines have been extensively discussed. Also, considering the safety critical applications of the

axial flux machines such as (low power) traction applications needs investigation of these machines by means of fault tolerance. For that reason, by combining the requirements of a fault tolerant machine and the advantages of axial flux machines, the machine of for this study is selected as a five-phase axial flux PMSM. Also, considering the need for torque ripple elimination and current over-rating of fault mitigation applications, an air-cored stator with a novel winding design is adopted.

3.1.1 Prominent Characteristics of the Topology

In this study, an air-cored axial-flux permanent magnet synchronous machine (AF-PMSM) is selected The stator is placed between two identical rotor discs. Rotor discs are made of steel, and they are magnetically insalient: Permanent magnets are directly attached on the smooth surface of the rotor yoke. Considering that the stator core has also no magnetic saliency, it can be said that the motor has no capability to produce reluctance torque. Also, the air-cored structure of the machine will prevent the saturation in the rotor yoke, as the effective air-gap of the machine becomes quite large with two air-gaps and the air-cored stator between steel rotor discs. The explained topology is shown in Figure 3.1.

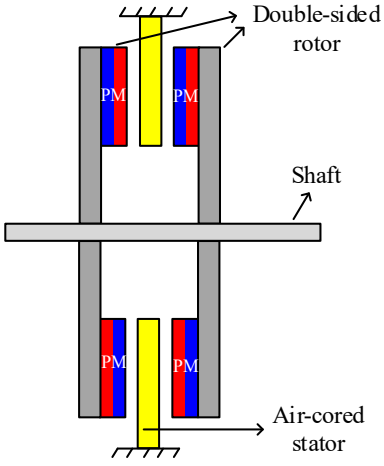

Figure 3.1: Double Rotor Air-Cored AFPMSM Topology (retrieved from [5])

The most innovative aspect of this machine topology is the structure of the stator, which is made of a novel coil topology, flat winding. Flat winding is a novel winding topology and is inspired by hairpin winding [44]. The production process and the

structure of a flat wire is shown in Figure 3.2.

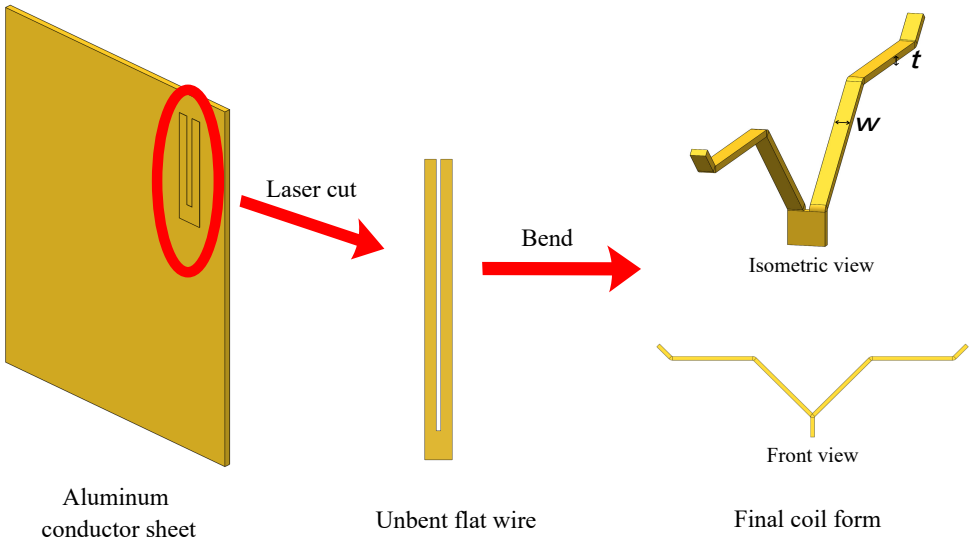

Figure 3.2: Making of a Flat Wire (retrieved from [5])

The motivation behind adopting this new type of winding structure can be summarized as follows:

- **Large current carrying capability:** One single flat wire has a large cross sectional area compared to conventional stranded winding cables. As an example, considering the skin effect limitation, one single aluminum flat wire with a cross-sectional area of $5\,mm^2$ is capable of safely carrying $25\,A$ of current at a maximum of $270\,Hz$. Due to this advantage, large amount of current can be carried in a single-strand flat winding, without the need of using paralleled winding structure.

- **Shorter end windings:** Flat wires are connected to each other using soldering and welding techniques [5]. This will result in shorter end-windings, lower phase resistance; hence higher efficiency.

- **Cooling performance:** The study in [5] shows that flat wires are capable of reaching a current density of $7\,A/mm^2$, where this value is only $4\,A/mm^2$ for conventional stranded-wound electrical machines.

- **Complete electrical isolation between the coils:** This is the most important aspect of the flat winding topology by means of fault tolerance. The most com-

mon faults in PMSMs are inter-turn short circuit faults, with a ratio of $30-40\%$ among all other failure types [12]. In this topology, as shown in Figures 3.3b and 3.5b, high-temperature insulation papers are placed between two neighboring flat wires. Finally, the assembly of coils are covered with the insulating epoxy resin. This manufacturing process ensures the electrical isolation between each flat wire and **completely** eliminates the inter-turn short circuit risk for a wide range of load current and operating temperature.

All above-mentioned assets make the flat winding topology favorable for the selection of the stator topology of a fault tolerant PMSM. On the other hand, there are some drawbacks of adopting this topology:

- **Low inductance:** As the machine is air-cored, effective air-gap is quite high compared to the conventional machines. A large air-gap means large reluctance, which results in low inductance. Lower inductance is a major challenge for the control of the machine, since low electrical time constant due to low inductance will require faster control loops. Also, low inductance coils are not very good at filtering the current fluctuations due to PWM of the inverter, current loop controllers and sensor noise.

- **High mutual coupling:** Due to the design of the flat winding, the axial area covered by the phase windings have large overlaps. This causes relatively high mutual inductance between phases. High mutual inductance is an unwanted property for a fault tolerant machine topology since it contradicts with the "complete isolation between phases" principle [6]. Especially for short circuit faults, large fault currents may affect the healthy phases too, when the mutual inductance between phases is high. However, for this structure, complete physical isolation between each coil eliminates the short circuit risk. Therefore, it can be concluded that this disadvantage hardly matters thanks to the general structure of the machine.

- **The need of a custom-designed driver circuit:** As an explicit version of the previous item, faster control and low electrical time constant require high switching frequency for the inverter of the machine. In order to achieve higher

Table 3.1: Evaluation of the Proposed Topology

Property	**Advantage**	**Disadvantage**	**Why?**
Air-cored	X	X	(+) No cogging torque (-) Low inductance
Axial-flux	X		(+) High torque density (+) Stackable
Flat winding	X		(+) Large cross-section, high current rating (+) More efficient (+) No need for extra isolation coating
Epoxy-covered stator	X		(+) No short-circuit risk (+) Thermal performance
Low inductance		X	(-) Challenging control (-) Almost no filtering (-) Custom inverter design
High mutual coupling		X	(-) Not favorable for fault tolerant topologies

switching frequencies, the use of Si-based conventional switches may not be possible and the use of wide band gap semiconductor devices becomes inevident.

- **Low number of turns:** As the diameter of the stator decreases, the number of flat wires that can be stacked becomes limited. This will result in lower number of turns for each phase; hence, lower phase induced voltage. For the same power rating, lower induced voltage would require higher phase current rating. For that reason, the custom-designed driver circuit should have the capability to carry high amount of currents.

To summarize, the assets and disadvantages of using this structure can be summarized as in Table 3.1.

3.1.2 Manufacturing Steps of the Machine Prototype

Another advantage of the flat winding is the ease of manufacturing. With the use of modern industrial manufacturing tools, mass production of this type of stator can be achieved in a quite short amount time, since the winding production would include only cutting and bending processes. For hand-craft manufacturing, bending and assembly of the stator is rather easier than a conventional stranded winding topology, albeit it is a time-consuming process without automation.

In Figure 3.2, the production steps of a flat wire are shown. Unbent U-shaped flat wires are laser-cut from a thin aluminum conductor sheet, and then are bent with some certain angles. These angles are determined by the rotor pole number, in order to cover the pole area at a maximum level.

The flat wires then are placed alongside each other, forming a full circle as in Figure 3.5a. In the proposed design, a maximum of 240 wires with a thickness of 1 mm can be assembled. The end points of each conductor are connected using electrical connectors and the connections are reinforced with solder, as given in Figure 3.3a. Using welding techniques can be another possible method for this purpose.

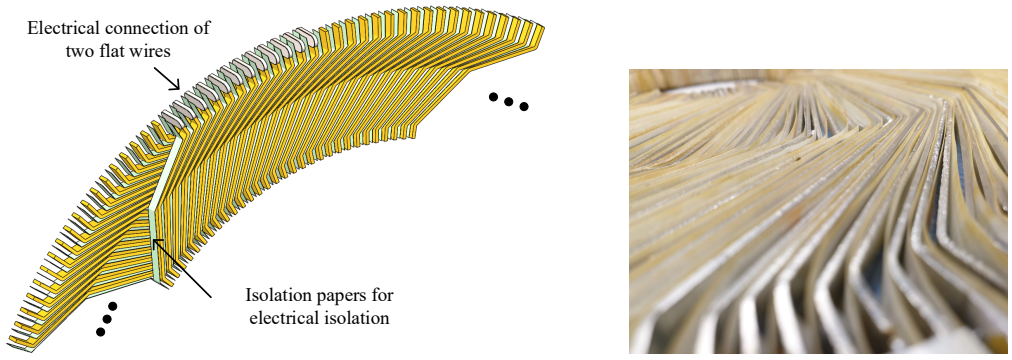

(a) Connection (retrieved from [5])

(b) Isolation Papers

Figure 3.3: Assembly Details of the Flat Winding

4 series-connected flat wires form a conductor loop, shown in Figure 3.4a; and for a five-phase machine, 12 of these loops are connected in series. The stator has a ten-phase structure. With external series connection, it becomes a five-phase one as given in Figure 3.4c. For the isolation between the conductors, insulation papers are placed

between each of them, as shown in Figure 3.3b.

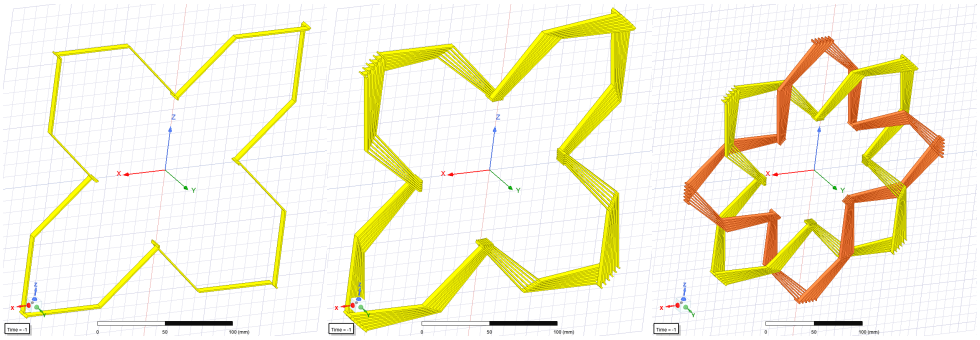

(a) One Loop of Flat Wires (b) Series of Loops (c) One Phase Winding

Figure 3.4: Flat Wire Loops Forming a Phase of the Machine

To ensure the mechanical robustness and electrical isolation, the flat winding assembly in Figure 3.5a is covered with epoxy resin and the stator of the machine is finalized as in Figure 3.5b.

(a) Flat Wire Assembly (b) Stator

Figure 3.5: Stator of the Machine Before and After Having Covered With Epoxy Resin

Rotor discs of the machine are magnetically insalient. The N42M grade NdFeB magnets are placed diagonally on the mid-circumference of the rotor. This structure is shown in Figure 3.6. The main reason for that is to make sure that one flat wire to be able to cover the whole flux area due to PMs, in order to maximize the flux linkage

[5]. The bending angles of each flat wire is therefore determined by number of poles of the machine. For an 8-pole structure, this angle becomes $135°$, as in Figure 3.2.

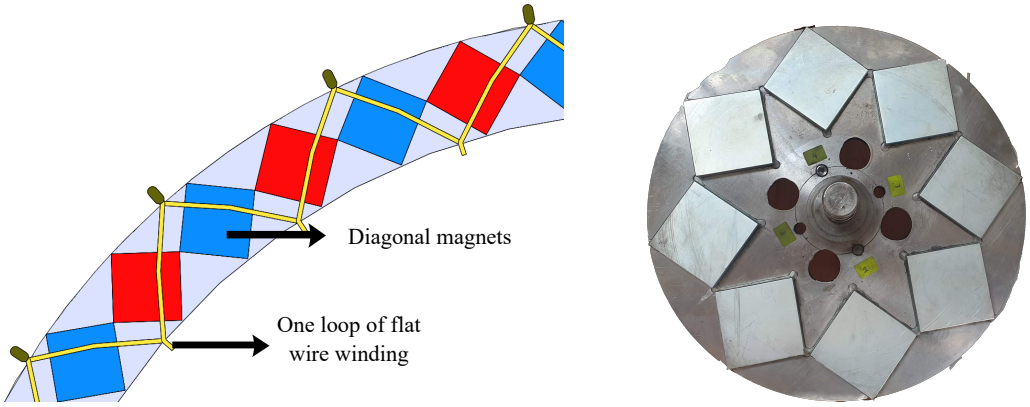

(a) Stator (b) Rotor

Figure 3.6: Rotor of the Axial Flux Air-Cored PMSM

The two rotor discs and the stator is mechanically assembled using wooden cases, bearings and screws. The final prototype becomes as in Figure 3.7. In the figure, it can be seen that the machine is not placed in a closed case, which is a supportive design decision for the cooling performance of the machine, without the need of forced cooling.

Table 3.2 includes some reference parameters for the design of a 3-phase version of this machine. In this study, the 5-phase machine with these dimensions and fixed design parameters will be evaluated.

3.2 Motor Driver

To control the machine current and voltage, a five-phase inverter is used. The driving circuit, which is given in Figure 3.8, composes of five cascaded half-bridge modules. As explained in Section 3.1, because of low phase inductance of the machine, the inverter's switching frequency must be high. Resultantly, this requires the use of wide band gap semiconductor devices. For that reason, the switching devices in each of these half-bridges are chosen as GaN HEMTs. GaN HEMTs have multiple advantages for motor drive applications. High switching speed, high power density

Figure 3.7: Final Prototype of the Five-Phase Axial Flux Air-Cored PMSM

Table 3.2: Design parameters of the machine

Parameter	**Value**
Rated power, P_{rated}	1.4 kW
Rated torque, T_{rated}	26 Nm
Rated speed, N_{rated}	525 rpm
Rotor inner radius, r_i	62 mm
Rotor outer radius, r_o	150 mm
Rotor yoke, l_{yoke}	20 mm
Air-gap length (each), l_g	2.3 mm
Stator thickness, l_s	11.4 mm
Total axial length, l_{tot}	80 mm
Pole number	8
Magnet thickness, l_m	12 mm
Magnet grade	N42M

and low conduction losses are major assets of these semiconductor devices [45]. Two GaN HEMTs are connected in parallel for each switching position, in order to satisfy

60 A maximum current. This is a safe limit for the machine, in order to be able to exceed the rated current value in fault or fault mitigating operations.

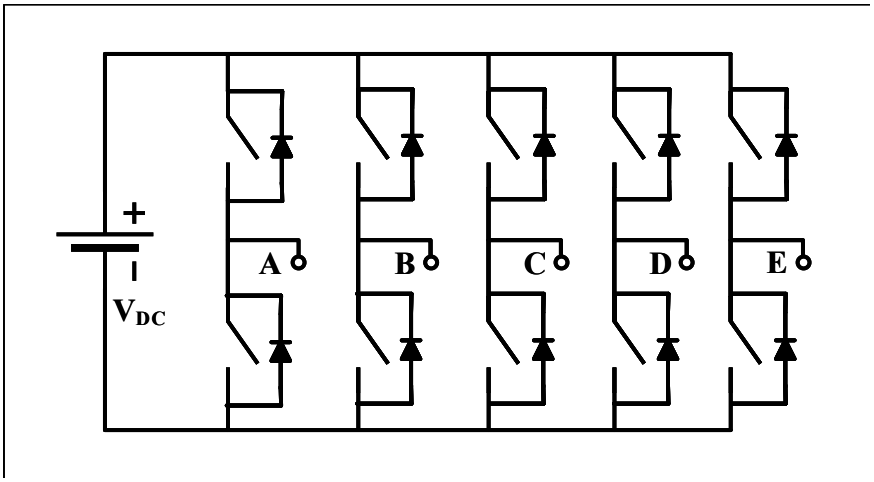

Figure 3.8: Structure of the Five-Phase Inverter

DC supply voltage is modelled as a single DC link capacitor, where star-connected motor windings are not connected to the negative side of the DC bus. For switching, carrier-based SPWM pattern with a switching frequency of 100 kHz is adopted. Because of this choice, the minimum level for DC bus voltage is 50 V, as only half of this voltage value is available as peak input phase voltage to the motor.

For the control of the inverter, the DSP of Texas Instruments, F28379D is preferred thanks to its high clock speed of 500 MHz and various built-in modules such as encoder reading (eQEP), communication and ADC/DAC conversion modules.

The five half-bridge modules, the DSP and four current sensors to measure the machine's phase currents are integrated on a custom-designed evaluation board. This board has several additional programmable functions to facilitate the user-device interaction, such as LED indicators, push buttons and potentiometers. The photographs of the evaluation board and F28379D are given in Figure 3.9.

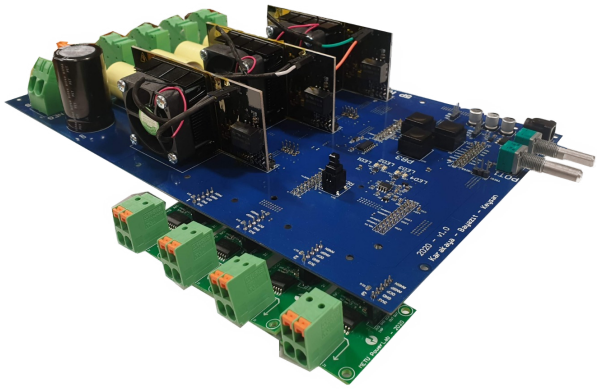

(a) Inverter

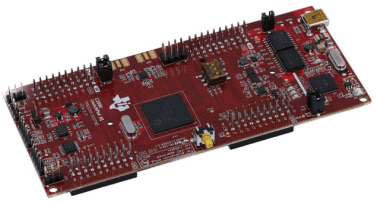

(b) TI Launchpad F28379D (retrieved from [46])

Figure 3.9: Motor Driver Circuit and the Controller

3.3 Verification of the Machine Specifications

Table 3.2 summarizes the fixed design parameters of the machine prototype. The design steps and the optimization procedure of the machine are clearly described in [5]. Based upon these constraints, the performance parameters of the machine is formulated throughout this section.

3.3.1 Verification of the Magnetic and Electrical Loading

The first step of the design and analysis of an electric machine is the determination of the electrical and magnetic loading values. As these values directly effect the output torque and power of the machine, design choices should be made to satisfy both feasibility and manufacturability concerns.

To determine the magnetic loading of the machine, initially, the magnetic equivalent circuit of the topology should be examined. In Figure 3.10, air-cored double rotor axial flux PMSM topology and its magnetic equivalent circuit is shown. On the figure, the relative permeability of the materials for each component are indicated. The relative permeability for the rotor, stator, magnets and air-gaps are shown with μ_r, μ_s, μ_m and μ_g, respectively, where their corresponding reluctance values are shown in the

magnetic equivalent circuit with $\mathcal{R}_r$, $\mathcal{R}_s$, $\mathcal{R}_m$ and $\mathcal{R}_g$, respectively. On the circuit, ϕ_r indicates the residual flux due to the magnets. It should also be noted that μ_s and μ_g are 1, as the topology is coreless and the permeability for those components are μ_0.

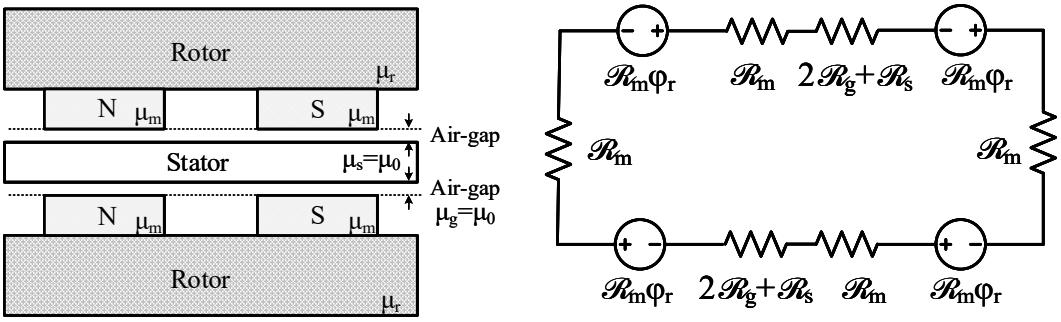

Figure 3.10: Double Rotor Axial Flux PMSM Topology and Its Magnetic Equivalent Circuit

Solving for this circuit, the flux density in the air-gap can be calculated as in (3.1), assuming a square-wave-shaped flux density distribution over a pole.

$$\begin{aligned} 4R_m\phi_r &= \phi_g\left(4R_m + 2R_s + 4R_g\right) \\ R_m B_r &= B_g\left(R_m + \frac{1}{2}R_s + R_g\right) \\ \frac{l_m}{\mu_m}B_r &= \left(\frac{l_m}{\mu_m} + \frac{l_s}{2} + l_g\right)B_g \\ B_g &= \frac{B_r\left(\frac{l_m}{\mu_m}\right)}{\frac{l_m}{\mu_m} + \frac{l_s}{2} + l_g} \end{aligned} \tag{3.1}$$

For this assumption, fundamental and third-order flux density components can be calculated as in (3.2) and (3.3), respectively.

$$\widehat{B}_{\delta,1} = \frac{4}{\pi}\widehat{B}_g \tag{3.2}$$

$$\widehat{B}_{\delta,3} = \frac{4}{3\pi}\widehat{B}_g \tag{3.3}$$

In this prototype, N42M grade magnets are used. As indicated in [5], the machine temperature is expected not to exceed $80°$C. The magnet properties are given in Table 3.3 for this operation region.

Table 3.3: N42M grade magnet properties at $80°$C

Parameter	**Value**
Residual magnetism (B_r)	1.29 T
Coercivity (H_c)	991 kA/m
Relative permeability (μ_m)	1.05

Replacing the variables in (3.2) with the parameters given in Table 3.2, the magnetic loading (for the fundamental frequency) of the machine is found as 0.966 T.

This value, however, is obtained by ignoring the leakage flux completely. Having a large air-gap in this air-cored topology substantially diminishes the already inaccurate magnetic equivalent circuit model's reliability. Therefore, it is necessary to take into account the leakage flux due to the magnets to obtain realistic performance parameters. In [47], a formulation for air-gap leakage flux is proposed for surface mounted PM machines, in terms of machine parameters and magnetic materials' properties. This leakage flux factor, shown as k_{leak}, can be defined as in (3.4).

$$\widehat{B}_{\delta,1} = \frac{\pi}{2}\, k_{leak}\, B_r \tag{3.4}$$

Another approximation that should be made is to assume uniform Maxwell stress distribution, which is the attraction force between the rotor and the stator, over whole rotor surface, rather than the actual trapezoidal shape by defining a constant k_{mag}, which is the ratio of magnet area to pole area [48]. This approximation is illustrated in Figure 3.11.

Applying this formulation to our topology, assuming a magnet to pole area ratio of 0.78 as indicated in [5] and using the machine dimensions, a leakage flux factor k_{leak} of 0.442, which makes the magnetic loading of the machine $\widehat{B}_{\delta,1}$ 0.896 T.

Electric loading calculation of axial flux machines differs from radial flux machines. As the whole stator surface touches the air-gap, linear current density value can change as a function of radius. In [49], linear current density is calculated on the mean radius, which is the effective maximum linear current density in the motor. In our topology, one fourth of each four-sided-loop on each conductor layer can be con-

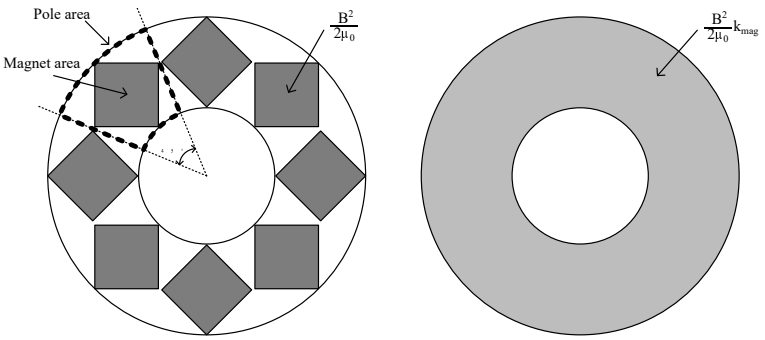

Figure 3.11: The Definition of k_{mag}, (retrieved from [5])

sidered as a turn in a slot. Therefore, resultant total turn number becomes the total number of flat wires. Following this approach, the electric loading of the machine can be calculated as in (3.5).

$$\widehat{A}_1 = \frac{N_{tot}\, k_w\, \widehat{I}_1}{2\pi r_{mean}} \tag{3.5}$$

For the given machine dimensions, the maximum number of flat wires (with 1 mm thickness and 5 mm^2 cross-section area, see Figure 3.2) that can fit in the stator is 240, as previously explained in Section 3.1.2. Also, choosing the current density value as 4 A/mm^2 will result in an RMS phase current of 20 A. With all these design decisions and by replacing (3.5) with the machine parameters, the electric loading is obtained as 10029 A/m.

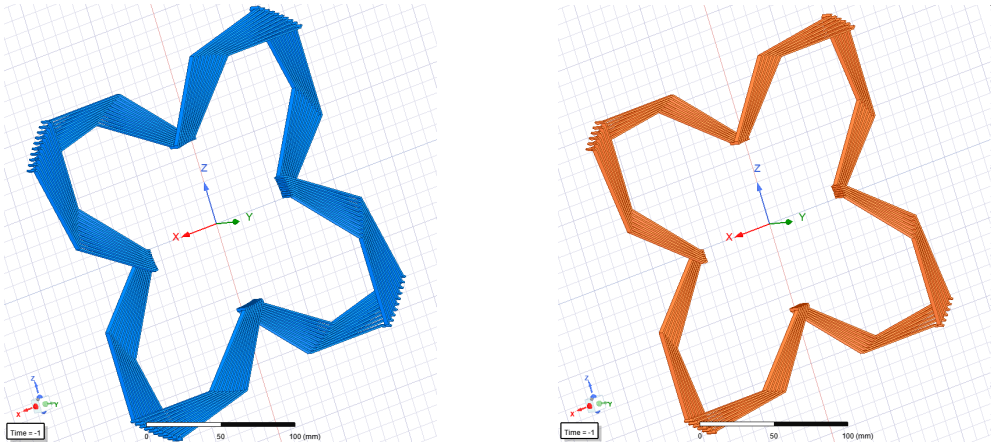

(a) Three-Phase

(b) Five-Phase

Figure 3.12: Connection of the Flat Winding for Different Phase Numbers

The winding of the machine is also modified as a five-phase stator. For the three-phase version, each phase winding composes of 10 series connected loops, which are made by connecting 4 flat wires with 90° symmetry in space. This configuration results in 6 set of windings, which is electrically equivalent to three-phase. For three-phase case, the winding factor becomes 0.955.

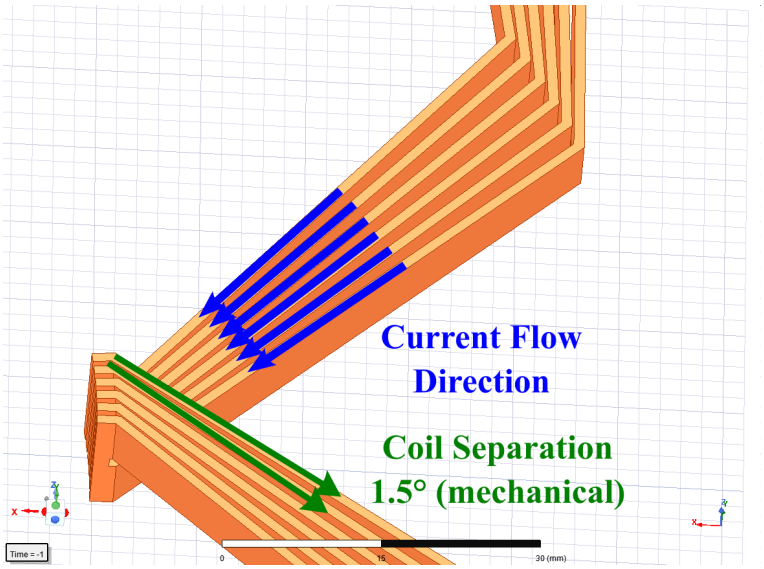

Figure 3.13: Calculation of the Winding Factor of a Flat Winding

Similarly, for the five-phase design, series-connected loop number becomes 6, as illustrated in Figure 3.4, with a total of 10 set of winding, electrically equivalent to five-phase. Both connections are shown in Figure 3.12 in order to better visualize. For each phase group, the direction of current flow and separation angles between the coils are shown in Figure 3.13. The winding factor can be calculated considering that there are 6 coils connected in series, and they are separated with an electrical angle of $6°$. Eventually, the winding factor becomes 0.984 with an increase of $3\,\%$ compared to the three-phase design.

3.3.2 Verification of the Torque and Power

The maximum torque that can be produced by this machine is related to the tangential stress due to electric and magnetic loading of the machine. Maximum tangential stress

can be defined as in (3.6).

$$\sigma_{tan} = \frac{\widehat{A}_1 \, \widehat{B}_{\delta,1}}{2} \tag{3.6}$$

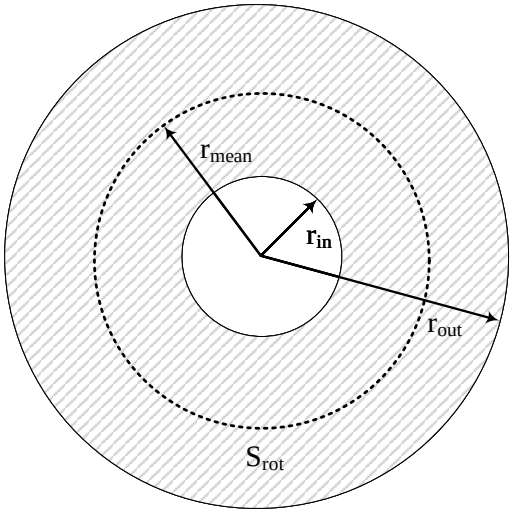

Figure 3.14: Rotor Dimension Variables

The machine torque can be calculated with two approaches that result in the same solution. First approach is to use the tangential stress, and the second is to calculate by using the air-gap power. In (3.7) and (3.8), the torque and power relations are shown. Figure 3.14 shows the dimension variables of the rotor to clarify the equations.

$$\begin{aligned}
T &= \sigma_{tan} \, r_{mean} \, S_{rot} \\
&= \frac{1}{2} \widehat{A}_1 \, \widehat{B}_{\delta,1} r_{mean} \pi \left(r_o^2 - r_i^2 \right) \\
&= \frac{5}{2} \frac{\widehat{B}_{\delta,1} N_{ph} k_w \widehat{I}_1}{\cancel{2\pi r_{mean}}} \cancel{\pi r_{mean}} \left(\underbrace{(r_o + r_i)}_{2r_{mean}} (r_o - r_i) \right) \\
&= 5 I_1 B_{\delta,1} N_{ph} k_w r_{mean} \left(r_o - r_i \right) \\
&= \frac{5 I_1 E_1}{\omega}
\end{aligned} \tag{3.7}$$

$$P = T\omega = 5 I_1 E_1 = 5 I_1 B_{\delta,1} \omega N_{ph} k_w r_{mean} \left(r_o - r_i \right) \tag{3.8}$$

Using (3.7), induced back EMF for first order frequency can also be obtained as in (3.9).

$$E_1 = B_{\delta,1} \omega N_{ph} k_w r_{mean} \left(r_o - r_i \right) \tag{3.9}$$

It should be noted that in (3.9), the term $r_o - r_i$ represents the radial projection of the conductive flat wire on the velocity vector, which is in the circumferential direction [50].

Using these relations that are between (3.4)-(3.9), the performance parameters for a rotor speed value of choice can be determined. For a mechanical speed of 525 rpm, (i.e. 35 Hz, electrical), the machine performance parameters can be summarized as in Table 3.4.

Table 3.4: Five-Phase Axial Flux PMSM Parameters

Parameter	**Value**
Electrical speed (ω)	70π rad/sec
Phase current (I_1)	20 A
Phase induced back EMF ($\widehat{E}_1$)	21.7 V
Torque (T)	28.3 Nm
Power (P)	1.5 kW

An important remark about this analytical approach is that the assumptions bring out the inaccuracy. Neglecting the higher-order-terms for the field (hence, induced back EMF) and the phase current, possible estimation errors in the leakage flux may cause a lower torque, induced back EMF and output power.

3.3.3 Inductance Calculation for the Five-Phase Topology

The total inductance matrix is composed of two main parts: Leakage inductance and magnetizing inductance matrices. Diagonal entries of the magnetizing inductance matrix shows the self inductance of each coil and denoted by L_{XX}, where X is an arbitrary phase of the machine. The other entries of the matrix includes the mutual inductance between each phase winding. The mutual inductances can be represented in two groups: mutual inductance between two adjacent coils and non-adjacent coils,

denoted by L_{XY} and L_{XZ}.

$$L_s = \begin{bmatrix} L_l & 0 & 0 & 0 & 0 \\ 0 & L_l & 0 & 0 & 0 \\ 0 & 0 & L_l & 0 & 0 \\ 0 & 0 & 0 & L_l & 0 \\ 0 & 0 & 0 & 0 & L_l \end{bmatrix} + \begin{bmatrix} L_{AA} & L_{AB} & L_{AC} & L_{AD} & L_{AE} \\ L_{BA} & L_{BB} & L_{BC} & L_{BD} & L_{BE} \\ L_{CA} & L_{CB} & L_{CC} & L_{CD} & L_{CE} \\ L_{DA} & L_{DB} & L_{DC} & L_{DD} & L_{DE} \\ L_{EA} & L_{EB} & L_{EC} & L_{ED} & L_{EE} \end{bmatrix} \tag{3.10}$$

In order to calculate the self and mutual inductances for each coil pair, the reluctance of the system should be defined. In Figure 3.15, the reluctance parameters of an air-cored axial-flux PMSM, such as inner and outer radii, air-gap length and core permeability are clearly shown. Having obtained the reluctance, the winding positions in the space and the winding functions of each coil should be considered. Figure 3.15 also shows the placement of the coils in the space. As previously mentioned, each coil is coupled to two adjacent coils with a spatial angle displacement of $72°$, and to two non-adjacent coils with a spatial angle displacement of $144°$.

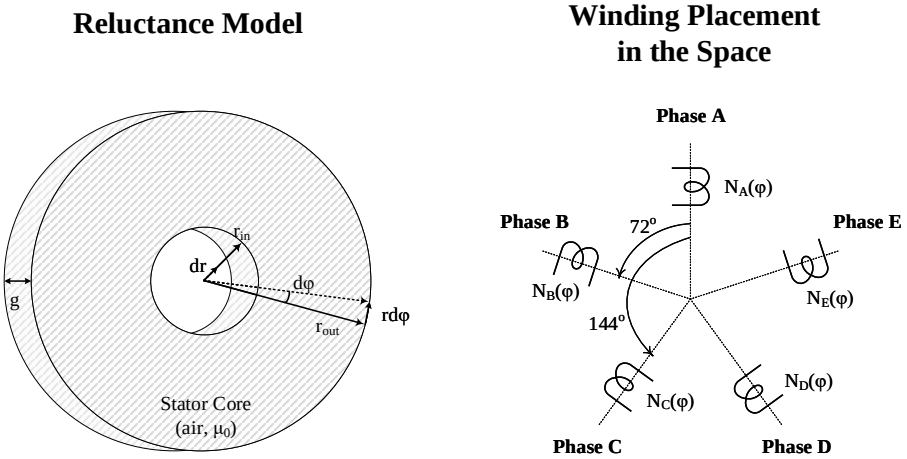

Figure 3.15: Reluctance Model of the Core and Winding Placement Schematic

Adopting the model given in Figure 3.15, inductance terms can be formulated as follows:

- Self inductance term:

$$L_{XX} = \frac{\mu_0}{g} \int_{r_i}^{r_o} \int_0^{2\pi} N_X^2(\phi) r \, d\phi \, dr \tag{3.11}$$

- Mutual inductance between two adjacent phase coils:

$$L_{XY} = \frac{\mu_0}{g} \int_{r_i}^{r_o} \int_0^{2\pi} N_X(\phi) N_Y(\phi) r \, d\phi \, dr \tag{3.12}$$

- Mutual inductance between two non-adjacent phase coils:

$$L_{XZ} = \frac{\mu_0}{g} \int_{r_i}^{r_o} \int_0^{2\pi} N_X(\phi) N_Z(\phi) r \, d\phi \, dr \tag{3.13}$$

Here, $N_x(\phi)$ is defined as the winding function of a phase. It is dependent on the spatial angle, ϕ, of a winding in the stator and can be approximated to a square wave with a period of 2π electrical radians, as given in Figure 3.16. Consequently, this square wave can be expressed in the form of Fourier series expansion, as given in Eq. (3.14).

$$N(\phi) = \sum_{n=1}^{\infty} \frac{4}{n\pi} \frac{N}{2} \sin\left(\frac{n\pi}{2}\right) \sin\left(n\phi\right) \tag{3.14}$$

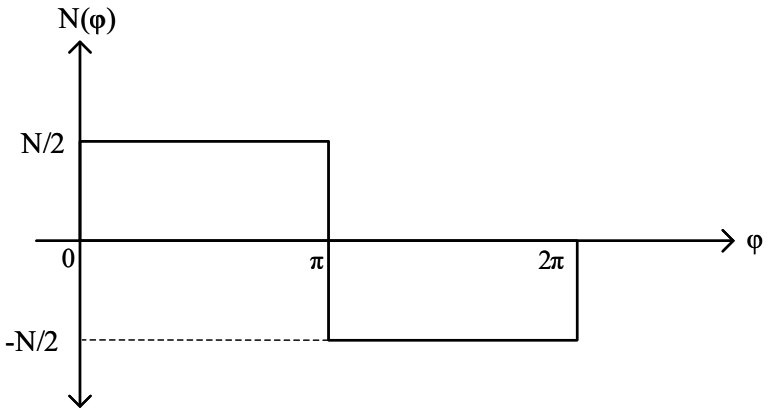

Figure 3.16: Winding Function of a Phase

The reference machine has a trapezoidal induced EMF that can be approximated by using fundamental and third order harmonics. For this case, harmonics with an order higher than 5 is negligible and all other electromagnetic parameters of the machine can be written in terms of fundamental and third order components. Also, considering

a symmetric form of the winding function for the sake of simplicity [51], the winding function for a single-phase can be approximated to:

$$N(\phi) = \frac{4}{\pi}\frac{N}{2}\left(\cos\phi - \frac{1}{3}\cos 3\phi\right) \tag{3.15}$$

where N is number of turns per pole per phase and ϕ can be replaced with $\phi \pm \frac{2\pi}{5}$ or $\phi \pm \frac{4\pi}{5}$ considering the corresponding phase angle.

Replacing (3.15) into (3.11), (3.12) and (3.13); we obtain:

$$L_{XX} = L_{m1} + L_{m3} \tag{3.16a}$$

$$L_{XY} = L_{m1}\cos(\frac{2\pi}{5}) + L_{m3}\cos(\frac{6\pi}{5}) \tag{3.16b}$$

$$L_{XZ} = L_{m1}\cos(\frac{4\pi}{5}) + L_{m3}\cos(\frac{2\pi}{5}) \tag{3.16c}$$

where

$$L_{m1} = 9\,L_{m3} = \frac{\mu_0(r_o^2 - r_i^2)}{g}\frac{2}{\pi}N^2 \tag{3.17}$$

As a result, the total inductance matrix, L_s can be expressed as in (3.19). Here, it is observed that the mutual inductance between two adjacent coils is positive, where the mutual inductance between two non-adjacent coils is negative. Resultantly, it can be deduced that for a phase winding, the current changes in the adjacent phases will have an additive effect, where this is vice versa for a non-adjacent phase winding.

$$L_s = \begin{bmatrix} L_l & 0 & 0 & 0 & 0 \\ 0 & L_l & 0 & 0 & 0 \\ 0 & 0 & L_l & 0 & 0 \\ 0 & 0 & 0 & L_l & 0 \\ 0 & 0 & 0 & 0 & L_l \end{bmatrix} \tag{3.18}$$

$$\begin{aligned} &+L_{m1} \begin{bmatrix} 1 & \cos\left(\frac{2\pi}{5}\right) & \cos\left(\frac{4\pi}{5}\right) & \cos\left(\frac{4\pi}{5}\right) & \cos\left(\frac{2\pi}{5}\right) \\ \cos\left(\frac{2\pi}{5}\right) & 1 & \cos\left(\frac{2\pi}{5}\right) & \cos\left(\frac{4\pi}{5}\right) & \cos\left(\frac{4\pi}{5}\right) \\ \cos\left(\frac{4\pi}{5}\right) & \cos\left(\frac{2\pi}{5}\right) & 1 & \cos\left(\frac{2\pi}{5}\right) & \cos\left(\frac{4\pi}{5}\right) \\ \cos\left(\frac{4\pi}{5}\right) & \cos\left(\frac{4\pi}{5}\right) & \cos\left(\frac{2\pi}{5}\right) & 1 & \cos\left(\frac{2\pi}{5}\right) \\ \cos\left(\frac{2\pi}{5}\right) & \cos\left(\frac{4\pi}{5}\right) & \cos\left(\frac{4\pi}{5}\right) & \cos\left(\frac{2\pi}{5}\right) & 1 \end{bmatrix} \\ &+L_{m3} \begin{bmatrix} 1 & \cos\left(\frac{6\pi}{5}\right) & \cos\left(\frac{2\pi}{5}\right) & \cos\left(\frac{2\pi}{5}\right) & \cos\left(\frac{6\pi}{5}\right) \\ \cos\left(\frac{6\pi}{5}\right) & 1 & \cos\left(\frac{6\pi}{5}\right) & \cos\left(\frac{2\pi}{5}\right) & \cos\left(\frac{2\pi}{5}\right) \\ \cos\left(\frac{2\pi}{5}\right) & \cos\left(\frac{6\pi}{5}\right) & 1 & \cos\left(\frac{6\pi}{5}\right) & \cos\left(\frac{2\pi}{5}\right) \\ \cos\left(\frac{2\pi}{5}\right) & \cos\left(\frac{2\pi}{5}\right) & \cos\left(\frac{6\pi}{5}\right) & 1 & \cos\left(\frac{6\pi}{5}\right) \\ \cos\left(\frac{6\pi}{5}\right) & \cos\left(\frac{2\pi}{5}\right) & \cos\left(\frac{2\pi}{5}\right) & \cos\left(\frac{6\pi}{5}\right) & 1 \end{bmatrix} \end{aligned} \tag{3.19}$$

With the given machine dimension parameters in Table 3.2, the terms of the inductance matrix are obtained as in (3.20). In (3.20), the term g denotes the air-gap length, which includes the air-gap at both sides of the stator, and the coreless stator itself.

$$\begin{aligned} L_{m1} &= \frac{\mu_0(r_o^2 - r_i^2)}{g}\frac{2}{\pi}N^2 \\ &= 33.6\,\mu H \\ L_{m3} &= \frac{L_{m1}}{9} = 3.7\,\mu H \end{aligned} \tag{3.20}$$

Replacing the magnetizing inductance coefficients calculated in (3.20) in (3.19), the inductance matrix (without considering the leakage inductances) can be found as in (3.21). If the leakage inductance is considered, the diagonal entries in the matrix (3.21) are expected to increase 5-10 μH. Evaluating the results, it can be concluded that the machine has quite a low phase inductance, whereas there is high magnetic coupling between the phase windings.

$$L_s = \begin{bmatrix} 37.3 & 7.4 & -26 & -26 & 7.4 \\ 7.4 & 37.3 & 7.4 & -26 & -26 \\ -26 & 7.4 & 37.3 & 7.4 & -26 \\ -26 & -26 & 7.4 & 37.3 & 7.4 \\ 7.4 & -26 & -26 & 7.4 & 37.3 \end{bmatrix} \mu H \tag{3.21}$$

3.3.4 Finite Element Modelling

In the previous section, the design of a five-phase air-cored AFPMSM is presented.With both fixed and calculated variables of the air-cored AFPMSM, a 3D model is built in ANSYS Maxwell environment. This model, which is shown in Figure 3.17 with isometric and axial views, is one-fourth of the machine, as we can take advantage of the magnetic symmetry property of this 8-pole topology.

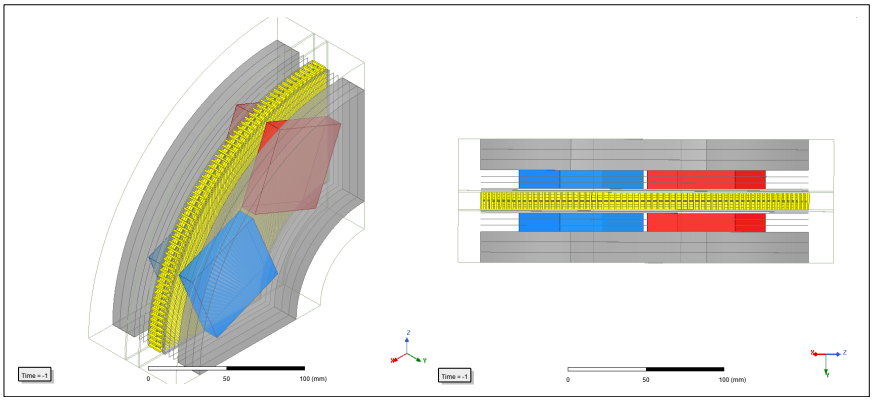

Figure 3.17: Structure of the FE Model of the AFPMSM

It is worth to mention one more time that this analysis technique takes several hard-to-analytically-compute aspects of the machine parameters into account. Hence, nearly the same results as the physical system's can be obtained using FEA method and these results are more reliable than analytically calculated ones. For this reason, especially the magnetic variables of the machine, such as air-gap magnetic flux density, induced back EMF of each phase, phase self and mutual inductances and output torque have been verified and the discrepancy between analytical results have been observed.

In Figure 3.18, the distribution of the magnetic flux density vectors ($\vec{B}$) are present.

In Figure 3.18, it can be observed that the maximum of the $\vec{B}$ is around 0.75 T and the distribution is far from being pure sinusoidal. This is also presented in Figure 3.19a in graphical form as the $\vec{B}$ distribution at the mean rotor radius.

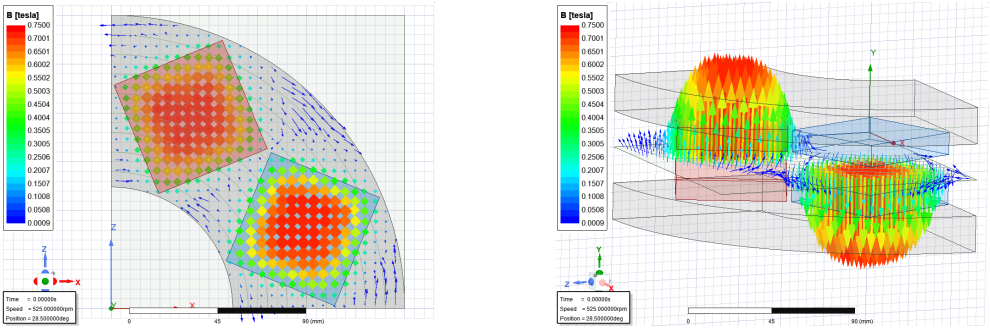

(a) Front View

(b) Isometric View

Figure 3.18: Distribution of Air-gap Magnetic Flux Density Vectors in the Machine

The distribution in 3.18 can also be shown graphically. These $\vec{B}$ vectors should be obtained over an arc in Maxwell. In the model, this arc is located in the middle of the air-gap in axial direction and on the mid-radius of the rotor. Figure 3.19a shows air-gap $\vec{B}$ field as a function of mechanical rotor angle. In the figure, it can be seen that peak flux density is 0.73 T. However, as given in Figure 3.19b that shows the harmonic spectrum of the magnetic flux density, the third harmonic component of this trapezoidal waveform is 16% of the fundamental component. Resultant fundamental peak air-gap flux density is 0.83 T. Comparing this value with the analytically obtained one using (3.4), a discrepancy of 7% is present, which is within the acceptable boundaries.

Air-gap magnetic flux density distribution can also be shown for different rotor radii. Figure 3.20 shows $\vec{B}$ field as a function of mechanical rotor angle at the radii of 70, 80, 90 and 100 mm. In the figure, it can be seen that the amount of harmonic components and resultant field waveform changes with changing radius. Based on these results, the optimum point without the higher order terms can be found. On this arc, magnet to pole area ratio can be calculated; and this value can be used while designing an axial flux PMSM with sinusoidal induced back EMF.

Being in relation with the air-gap magnetic field, induced back EMF and output torque

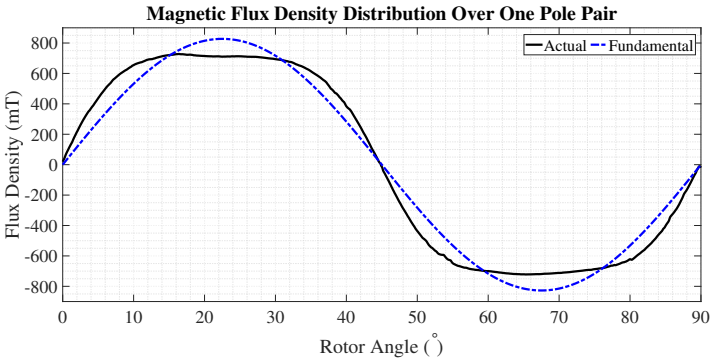

(a) $\vec{B}$ as a Function of Rotor Angle at the Mean Rotor Radius

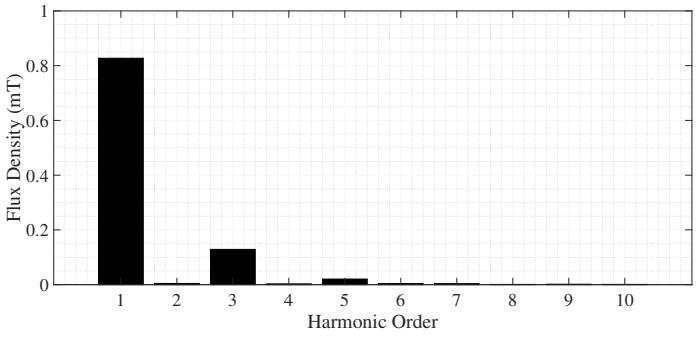

(b) Harmonic Spectrum of $\vec{B}$

Figure 3.19: Air-gap Magnetic Flux Density and Its Spectral Analysis, Obtained with FEA

of the machine is also expected to deviate from the analytically calculated ones. Figure 3.21 shows the induced back EMF for each phase of the machine at full speed, 70π rad/sec, and at full load, with a current excitation of 20 A_{rms}. For this operation region, the output torque is expected to be 26.5 Nm with almost no ripple. Induced back EMF, which is also trapezoidal, for each phase is expected to have a peak of 18 V with a peak fundamental voltage of 20.7 V. These torque and induced back EMF values have also a discrepancy of 6-7$\%$ compared to calculated values, and they are in good agreement with the analytical calculations.

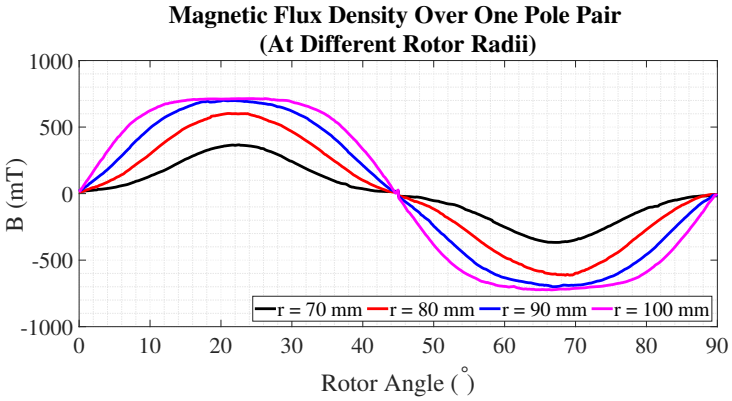

(a) $\vec{B}$ as a Function of Rotor Angle at the Mean Rotor Radius

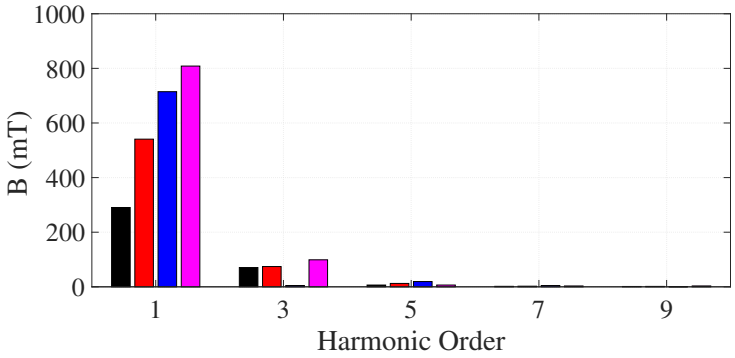

(b) Harmonic Spectrum of $\vec{B}$

Figure 3.20: Air-gap Magnetic Flux Density and Its Spectral Analysis At Different Rotor Radii, Obtained with FEA

Another machine parameter that needs to be verified with FEA is the machine inductance. (3.22) shows the inductance matrix obtained with FEA. Both self and mutual inductances are compatible with the analytically calculated ones given in (3.21). The leakage inductance for each phase is seen to be 6.8 μH.

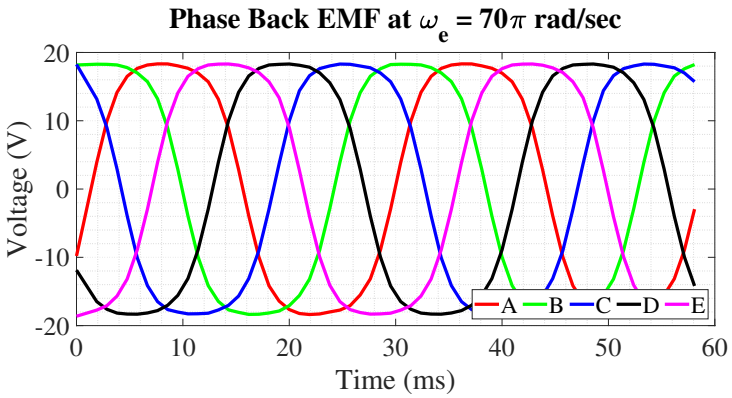

(a) Induced Back EMF

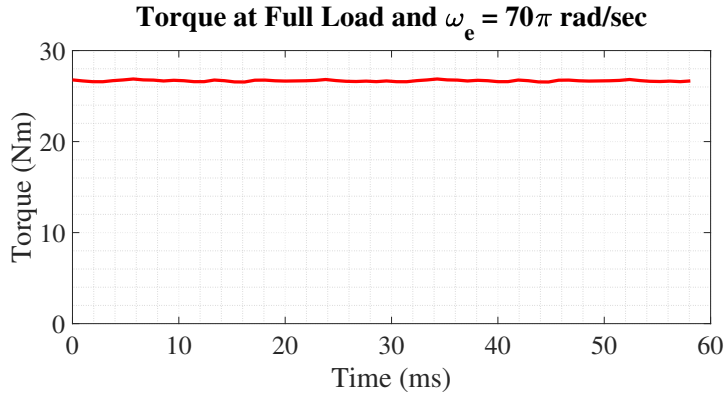

(b) Torque

Figure 3.21: Machine Performance Parameters Under Full Load, Obtained with FEA

$$L_s = \begin{bmatrix} 44.1 & 7.6 & -25.2 & -25.0 & 7.8 \\ 7.6 & 44.1 & 7.6 & -25.0 & -25.0 \\ -25.2 & 7.6 & 44.1 & 7.7 & -25.1 \\ -25.0 & -25.0 & 7.7 & 44.1 & 7.5 \\ 7.8 & -25.0 & -25.1 & 7.5 & 44.1 \end{bmatrix} \mu H \tag{3.22}$$

To summarize, the electromagnetic quantities that are analytically calculated and obtained with FEM are tabulated as in Table 3.5. Based on the discrepancy values, analytical calculations are compatible with the FEM results; except for the poorly estimated third order flux density distribution and ignored leakage inductance.

Table 3.5: Comparison of the Analytical Calculations and FEM Results

Parameter	**Analytical**	**FEM**	**Discrepancy**
$\widehat{B}_{\delta,1}$	0.89 T	0.83 T	7%
$\widehat{B}_{\delta,3}$	0.29 T	0.13	123%
$\widehat{E}_1$	21.7 V	20.7V	6-7%
L_{XX}	$37.3\,\mu H$	$44.1\,\mu H$	15%
L_{XY}	$7.4\,\mu H$	$7.7\,\mu H$	4%
L_{XZ}	$-26\,\mu H$	$-25.2\,\mu H$	3%
Torque	28.3 Nm	26.5 Nm	7%

3.4 Experimental Verification of the Machine Prototype in Generating Mode

In this section, the test results of the five-phase air-cored axial flux PMSM prototype in generating mode are presented. Machine tests have been performed under both full-load and no-load. Findings of the test results have been shown and their reasoning have been discussed in detail.

Figure 3.22 shows the setup on which the tests have been performed and the data has been obtained. In Figure 3.22b, the machine prototype is shown. The prototype is mechanically coupled to a DC motor, which is used as a prime mover in the tests. The prime mover DC machine is separately excited. Both its field and armature are fed by two separate variacs and two separate bridge rectifiers. The winding terminals of the prototype are connected to a five-phase bridge rectifier with a resistive load. All phase voltage and currents have been monitored using wattmeters and a 4-Ch DSO. In Figure 3.22a, all these equipment are available.

3.4.1 No-Load Tests

No-load experiments of the machine prototype is performed by measuring inductance values and phase induced EMF of the machine. (3.23) shows the inductance measurements of the motor. In the matrix, it can be observed that L_{XX}, L_{XY} and L_{XZ} values are not single, because of manufacturing tolerances.

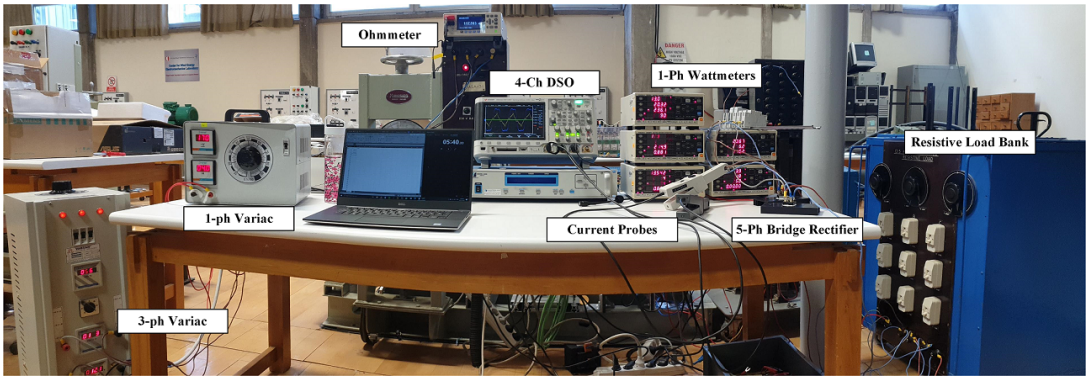

(a) Data Acquisition Devices

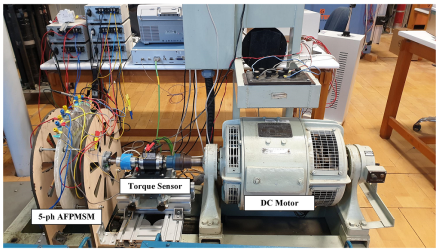

(b) 5-Ph Axial Flux PMSM and the Prime Mover DC motor

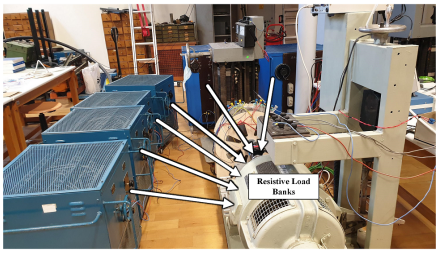

(c) Resistive Load Banks

Figure 3.22: Test Bench for Generating Mode Tests

$$L_s = \begin{bmatrix} 42.4 & 8.5 & -22.3 & -25.2 & 4.9 \\ 8.5 & 40.8 & 4.2 & -22.4 & -21.4 \\ -22.3 & 4.2 & 40.9 & 8.4 & -21.4 \\ -25.2 & -22.4 & 8.4 & 42.4 & 5.2 \\ 4.9 & -21.4 & -21.4 & 5.2 & 40.6 \end{bmatrix} \mu H \tag{3.23}$$

Table 3.6 shows a brief comparison of the inductance values obtained with analytical calculation, FEA and experimental measurement. Also, the deviation of the measurements from the FEA results is shown. It can be said that the inductance values of the prototype lie within the acceptable limits of tolerance.

Firstly, the prototype machine is operated in generating mode, under no-load condition, at rated speed 525 rpm (i.e. 35 Hz, electrical); and the phase induced EMF waveform has been obtained. This result is compared to the one obtained using finite

Table 3.6: Comparison of Analytical and Experimental Inductance Values

Parameter	**Analytical**	**FEA**	**Experiment (Min.)**	**Experiment (Max.)**	**Deviation from FEA (Min & Max)**
L_{XX}	37.3 μH	44.1 μH	40.6 μH	42.4 μH	3.9% - 7.9%
L_{XY}	7.4 μH	7.7 μH	4.9 μH	8.5 μH	10.4% - 36.4%
L_{XZ}	-26 μH	-25.2 μH	-21.4 μH	-25.2 μH	0 - 15.1%

element analysis. Both waveforms have been plotted on the same graph, for comparison, as given in Figure 3.23. As it was not possible to rotate the prime mover at exactly 525 rpm, a small difference between each waveforms can be observed. This difference is less than 1% of the rated speed.

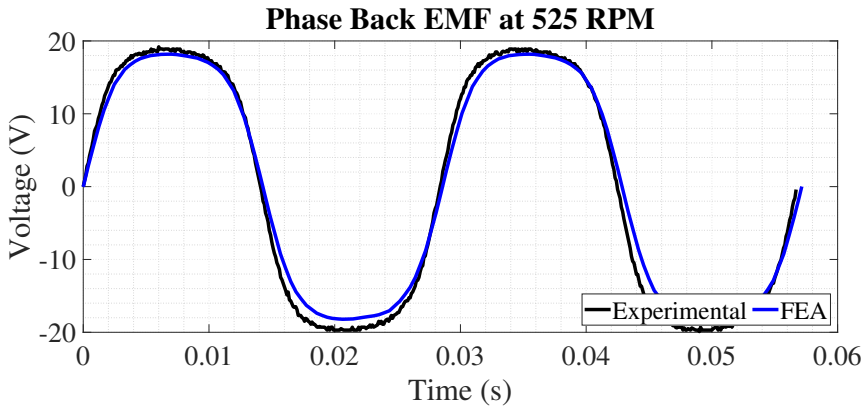

Figure 3.23: Phase Back EMF of the Machine: Comparison of the FEM and Experimental Results

Further, this operation is also repeated for different rotor speeds and the peak phase back EMF vs. electrical frequency curve given in Figure 3.24 is obtained. Obviously, the graph is almost fully linear, no saturation is observed, as expected.

Phase back EMF waveform is also analyzed in the frequency domain and its harmonic components have been obtained, using Simscape toolbox of MATLAB/Simulink. Experimantal voltage harmonics have been compared with FEA results, which are given in Figure 3.25. The experimental results are compatible with the design and are as expected.

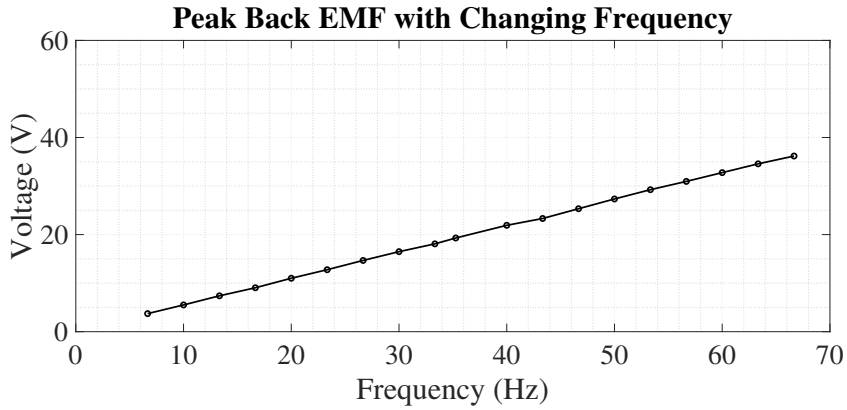

Figure 3.24: Phase Back EMF of the Machine as a Function of Electrical Frequency

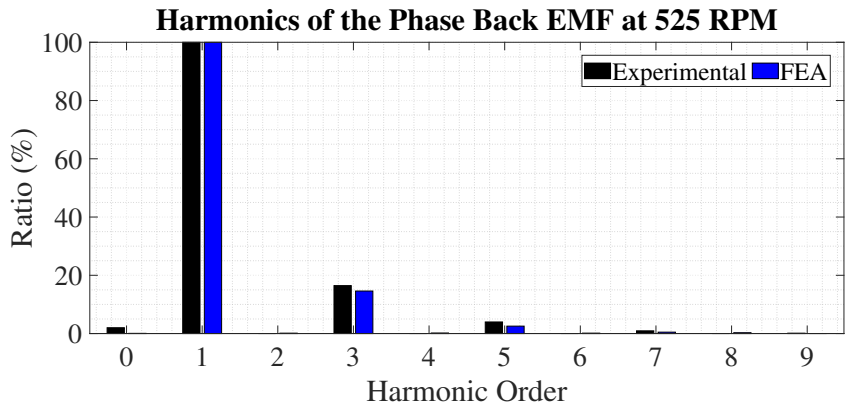

Figure 3.25: Harmonic Components of the Back EMF as a Ratio of the Fundamental Component

3.4.2 Full-Load Tests

To observe whether the machine operates within the desired thermal limits in loaded case, the machine terminals have been loaded electrically and operated for 60 minutes.

The main difficulty faced during this experiment was the lack of high-power, low-resistance electrical load in the laboratory. To overcome this issue, initial solution was to use a transformer, in order to increase the motor terminal voltage and decrease the necessary load current in the load bank side. Unfortunately, the use of two different 3-phase transformers led to an unbalance in the line inductance and resistance between

the machine phases, which resulted in unbalanced phase currents as given in Figure 3.26.

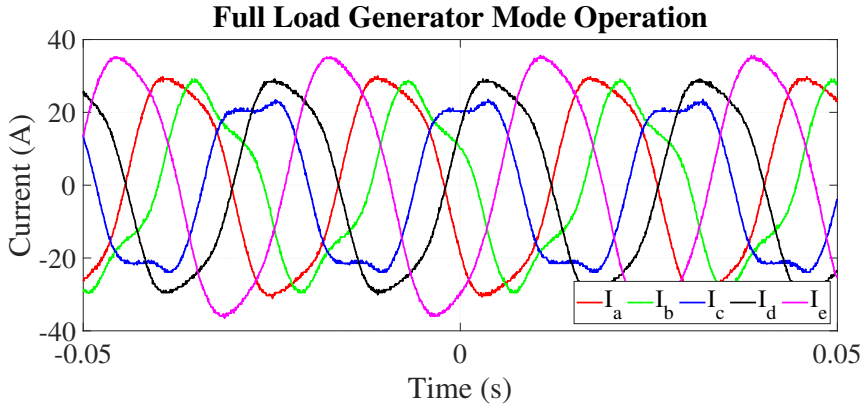

Figure 3.26: Unbalanced Phase Currents at Full Load Generation with Two Different 3-Ph Step-up Transformers as Load

Another solution was to rectify the 5-phase generator voltage with a 5-phase diode bridge, and connect a resistive load bank accordingly. This approach has become successful and balanced 5-phase current waveforms have been obtained as in Figure 3.27. For a more reliable thermal test, balanced phase currents is a necessity.

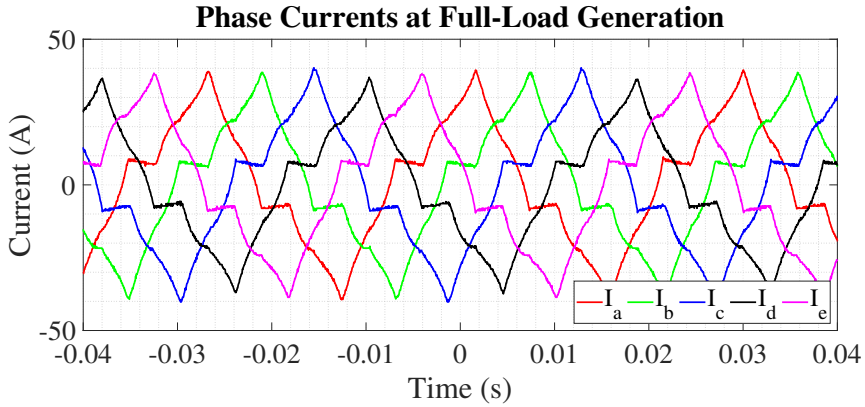

Figure 3.27: Balanced Phase Currents at Full Load Generation, with a 5-Ph Diode Rectifier as Load

The back EMF and current for a single phase is given in Figure 3.28.

In phase current waveform, the effect of commutation is observed. The duration of

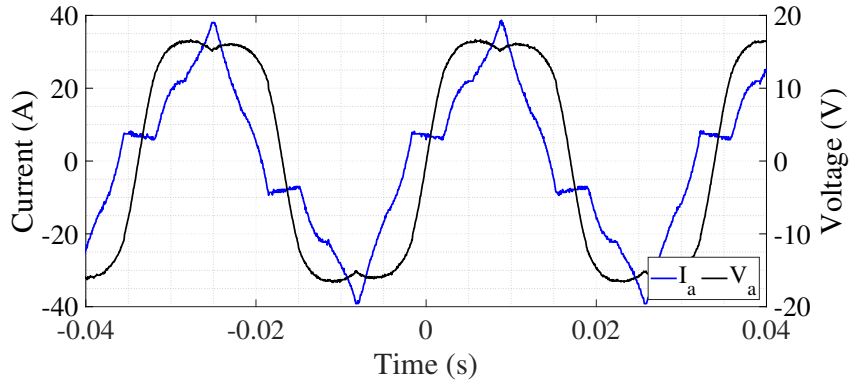

(a) Phase Current and Induced Voltage

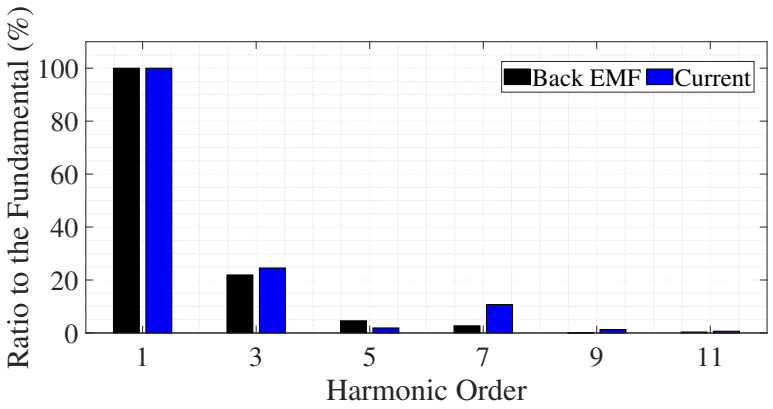

(b) Harmonic Distribution

Figure 3.28: Experimental Phase Current, Induced Voltage and Their Harmonic Distribution at Full Load, Generating Mode

the flat-spots around the 0 A level increase with increasing electrical frequency and increasing load current. We also observe that higher order harmonic components are introduced because of five-phase bridge rectifier of the load. For both phase back EMF and phase current waveforms, spectral analysis is performed using Simscape toolbox of MATLAB/Simulink. These results are shown in Figure 3.28b.

Phase back EMF at full-load (see Figure 3.28a) differs from the one at no-load (see Figure 3.23), and also includes higher order frequency components. The main reason for this difference is because the measured voltage is not the actual back EMF, but also includes the voltage drop on the resistance and inductance of the phase windings

(i.e. the measured voltage is terminal voltage). As the voltage drop on phase windings is related to the phase current, we observe the effect of higher order terms in the (so called) back EMF waveform.

During the 60-min-operation under full load, the temperature of the motor windings have been recorded using a PT100 temperature sensor placed under the flat wires while manufacturing the prototype, and a thermal camera.The curve of the temperature of the windings during the full-load operation is given in Figure 3.29.

The winding temperature reached to steady-state at $64°$C at the end of 60 minutes. It can be said that this temperature is within the safe region, considering the rigidness of the stator due to epoxy resin.

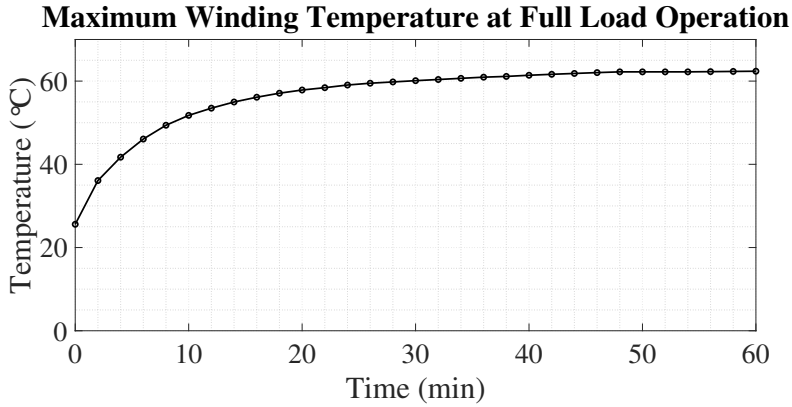

Figure 3.29: Temperature of the Motor Windings at Full Load Generation

The photographs have also been captured with a thermal camera to observe whether there are hot spots on the stator or not. These photographs are given in Figure 3.30. It is seen that the maximum temperature recorded by the thermal camera is around $54°$C. Therefore, it can be concluded that this tool is not a reliable option for sensitive measurements, as it could not measure the hot spots between flat wires in the stator winding.

As a result of both no-load and loaded tests (in generating mode), the operation of the manufactured prototype is verified to be in expected and safe boundaries, for both its electromagnetic quantities and thermal performance.

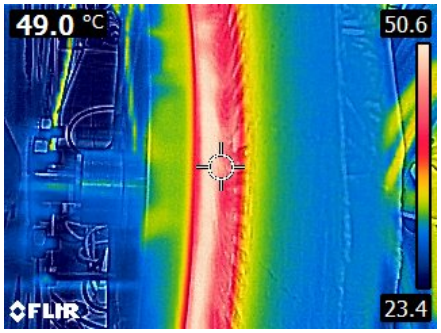

(a) Temperature distribution in the motor windings at t = 20 min.

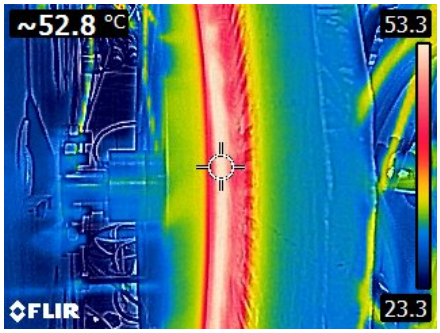

(b) Temperature distribution in the motor windings at t = 40 min.

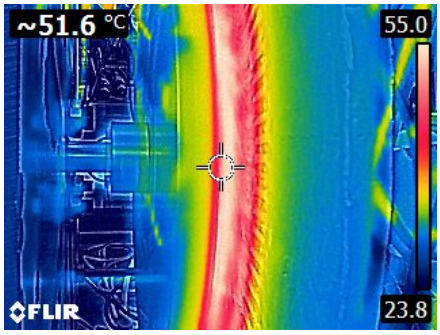

(c) Temperature distribution in the motor windings at t = 60 min.

Figure 3.30: Thermal Camera Pictures at Different Time Instants

3.5 Experimental Verification of the Motor Driver Circuit

Before the integration of the overall drive system, each element should be tested separately. Having verified the machine prototype, the operation of the inverter has to be checked too, using an RL load.

The pictures of one of the half-bridge modules on the inverter in both front and back views are shown in Figure 3.31. Five of these are mounted on the motherboard as given in Figure 3.9. The specifications of these half-bridge modules are summarized in Table 3.7, below.

Initially, to check the switching behavior of each switch on the half-bridge modules, double pulse test (DPT) is performed on the inverter. DPT is a test technique that

Table 3.7: Specifications of the Inverter

Parameter	Value
Maximum DC bus voltage, $V_{DC,max}$	120 V
Maximum switching frequency, $f_{sw,max}$	120 kHz
Phase current limit, $I_{OCP,phase}$	45 A
Switch number	4 (2 top, 2 bottom)
Continuous drain current, I_D	30 A (per switch)
Max. operating temp of the switch	150°C

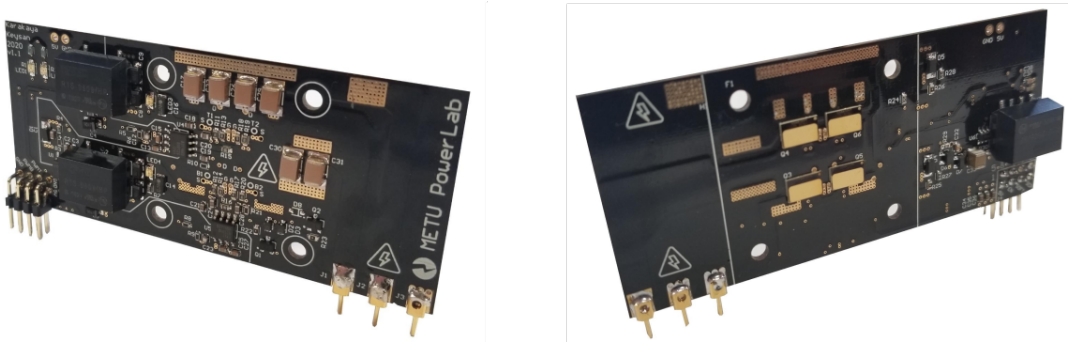

Figure 3.31: Picture of one Half-Bridge Module

determines the switching time and characteristics of a semiconductor switch by observing the current flowing through the load inductor [52].

Verification of the switches leads to synchronous switching of the half-bridge modules. As mentioned earlier, the main motivation of this test is to observe the synchronous operation of the five half-bridges and to observe the maximum temperature after the inverter operates at full load for a while.

As the electrical load, two three-phase RL load with low phase inductance and resistance (were available and) were chosen. Even if operation at high DC bus voltage was not possible because of low impedance of the load, the inverter reached to the rated phase current value. Phase currents for this experiment are shown in Figure 3.32. The magnitudes of phase currents are different from each other (In fact, the currents of phases D and E are higher than the other ones.). This is because the two three-phase loads were not identical; there is a difference of 8% between the impedance

values of the two loads.

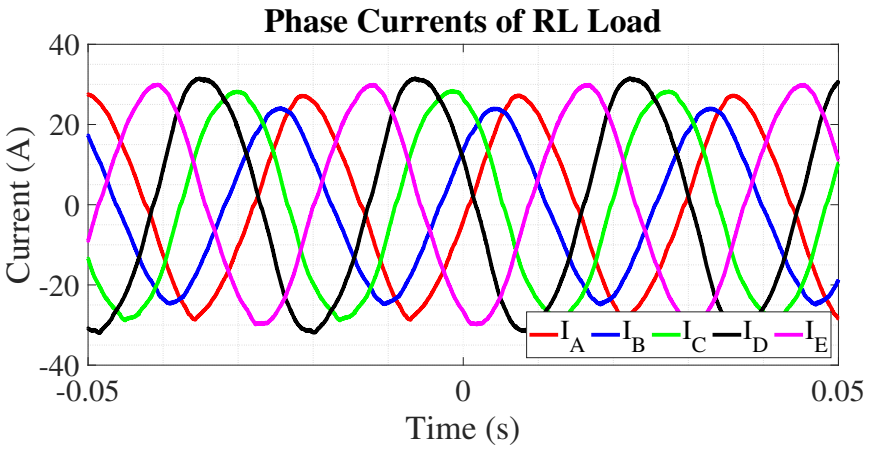

Figure 3.32: Experimental Result of the Operation of the Inverter with an RL Load, at Full Load

For the operation at full load, conduction losses in GaN HEMTs increase dramatically. Heat dissipation performance weakens and the temperature of the devices increases fastly. The photographs of the inverter, taken with a thermal camera at different time instants are shown in Figure 3.33. For a 20-minute-operation, the maximum temperature reaches 80°. Even if this might be considered as a safe operation point, the fast increase of the temperature may cause deterioration of the switches.

(a) Temperature Distribution on the Five-Phase Inverter, at t = 5 min.

(b) Temperature Distribution on the Five-Phase Inverter, at t= 10 min.

(c) Temperature Distribution on the Five-Phase Inverter t = 15 min.

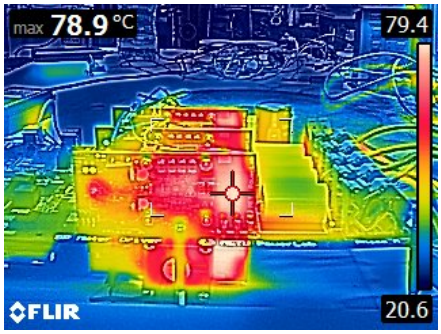

(d) Temperature Distribution on the Five-Phase Inverter at t = 20 min.

Figure 3.33: Thermal Camera Pictures at Different Time Instants

3.6 Conclusion and Discussion

This chapter focused on the proposal of an air-cored five-phase axial flux PMSM that is suitable for high torque, low speed applications. The most prominent characteristic of the machine is its winding. The coils of the winding are thin flat aluminum wires that are cut from an aluminum sheet and then bent to obtain a specific shape. The major advantages of this novel winding type are its high current carrying capability, its easy manufacturing process and short circuit risk elimination thanks to its epoxy resin cover which is an insulating material. In the sense of fault tolerance, consideration of open circuit failures is sufficient for the study of this machine. On the other hand, the drawback of the topology is its low phase inductance, which may cause difficulties for the control of the machine because of its low electrical time constant.

Additionally, the construction and sizing steps of the machine were also presented. As a result of large effective air-gap, the effect of leakage flux is far from being negligible in this topology. Therefore, analytical calculations of magnetic flux density in the air-gap should be made by taking the leakage flux also into consideration. Otherwise, analytical design may be incompatible with the finite element model and the manufactured prototype machine. For the analytically calculated and numerically obtained electromagnetic quantities, there is a discrepancy of $5 - 7\%$, which is an acceptable range.

This chapter also included the experimental results of the prototype five-phase Axial-Flux PMSM (AFPMSM). No-load tests in generating mode showed that the machine operates in the linear region, considering the linear relation between the electrical frequency and induced phase EMF of the machine. Furthermore, full-load test on the prototype presented the superior thermal performance of the topology, as the temperature of the windings became only $62°$C after an hour of loaded operation.

Finally the test results of the GaN-based inverter that is a custom design for this machine were also presented. A dramatic increase in the temperature of the transistors were observed when the inverter supplied rated current to the RL load. It is concluded that the critical element in the drive was the inverter that determines the safe operation boundaries and time of the motor drive system.

CHAPTER 4

FIVE-PHASE MOTOR DRIVE: ANALYSIS, DRIVE SIMULATION AND EXPERIMENTAL VERIFICATION

Analytical modeling of the machine and other drive components is essential for both verification of the drive operation with numerical analysis and for the implementation of control algorithms. For that purpose, in this chapter, mathematical background of a five-phase machine will be examined. Matrices and vectors corresponding to the electromagnetic quantities of the machine will be defined, coordinate transformations of stationary and rotating reference frames will be explained. Equations of the electromechanical system dynamics will be given. Following that, the simulation model of the five-phase electric drive will be described. Sub-units and functioning of the model will be explained in detail. On top of that, the experimental realization of the five-phase motor drive will also be presented in this chapter. Experimental test-bed will be introduced and the operating points of the motor drive will be explained. Finally, simulation results of the analytical model and the experimental results will be presented, compared and discussed.

4.1 Mathematical Background

In generalized theory of electrical machines, phase variables of field and armature components are represented as a linear system. Especially for this study, the use of unconventional five-phase topology requires explicit modeling and explicit explanations of the notations adopted throughout this study. Besides, the definition of the system equations and relations enables building a simulation model of the drive system. Therefore, in this section, the mathematical model of a five-phase motor drive

system will be explained thoroughly.

4.1.1 Definition of Stator Vector and Matrices

Phase-variable model of a five-phase PMSM can be reduced to an electrical equivalent circuit. In Figure 4.1, this equivalent circuit is shown, explicitly. Each phase of the machine can be represented as a combination of the phase induced EMF due to permanent magnets (PMs), stator phase inductance and phase resistance due to the windings. In Figure 4.1, phase induced back EMF is represented as the product of the flux linkage due to PMs (λ_{PM}) and the electrical speed of the rotor (ω_e). Inductance components for each phase are represented as the leakage inductance (L_l), self inductance (L_{XX}), mutual inductance between two adjacent coils (L_{XY}), and mutual inductance between two non-adjacent coils (L_{XZ}). Doubling these mutual inductance values is in order to represent all four mutually coupled coils to a single coil, two of which are placed adjacently, and the other two are placed non-adjacently to each coil. These inductance definitions and calculations will be further explained in the next subsection.

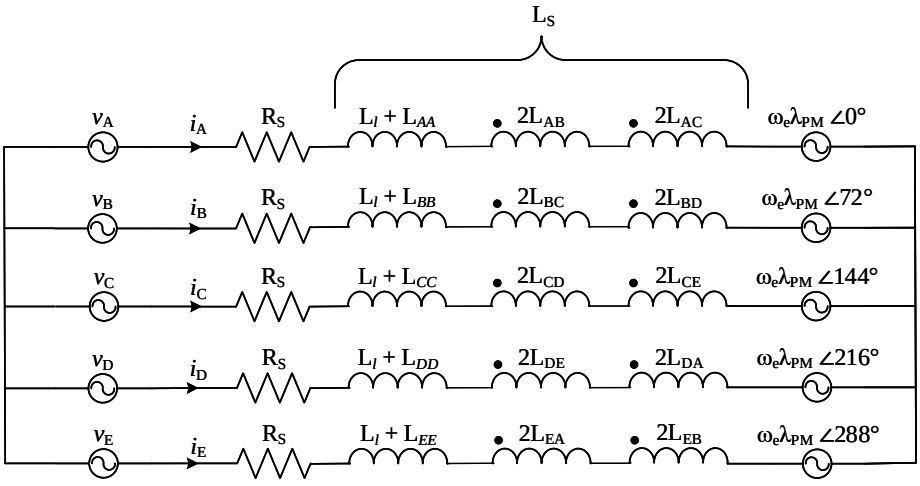

Figure 4.1: Simplified Circuit Schematic For a Five-Phase SM-PMSM

In a generalized sense, stator phase voltage of a permanent magnet synchronous ma-

chine is defined as follows:

$$\boldsymbol{V_s} = R_s \boldsymbol{I_s} + \frac{d}{dt}\boldsymbol{\Lambda_s} \tag{4.1}$$

For a five-phase machine, $\boldsymbol{V_s}$, $\boldsymbol{I_s}$ and $\boldsymbol{\Lambda_s}$ are 5x1 vectors and R_s is a 5x5 matrix. These can be defined as in Eq. 4.2-4.5.

$$\boldsymbol{V_s} = \begin{bmatrix} v_A & v_B & v_C & v_D & v_E \end{bmatrix}^t \tag{4.2}$$

$$\boldsymbol{I_s} = \begin{bmatrix} i_A & i_B & i_C & i_D & i_E \end{bmatrix}^t \tag{4.3}$$

$$\boldsymbol{\Lambda_s} = \begin{bmatrix} \lambda_A & \lambda_B & \lambda_C & \lambda_D & \lambda_E \end{bmatrix}^t \tag{4.4}$$

$$R_s = \begin{bmatrix} R_s & 0 & 0 & 0 & 0 \\ 0 & R_s & 0 & 0 & 0 \\ 0 & 0 & R_s & 0 & 0 \\ 0 & 0 & 0 & R_s & 0 \\ 0 & 0 & 0 & 0 & R_s \end{bmatrix} \tag{4.5}$$

It should be noted that flux linkage in each phase winding has two components: The flux created by permanent magnets on the rotor and the flux due to the current flowing in the windings. Consequently, stator flux linkage term can be expressed as in 4.6

$$\boldsymbol{\Lambda_s} = \boldsymbol{\Lambda_{ss}} + \boldsymbol{\Lambda_{PM}} \tag{4.6}$$

where the flux linkage vectors can be defined as:

$$\boldsymbol{\Lambda_{ss}} = L_s \boldsymbol{I_s} \tag{4.7}$$

$$\boldsymbol{\Lambda_{PM}} = \sum_{n=0}^{\infty} \lambda_{2n+1} \begin{bmatrix} \cos\left((2n+1)(\theta_r)\right) \\ \cos\left((2n+1)(\theta_r - \frac{2\pi}{5})\right) \\ \cos\left((2n+1)(\theta_r - \frac{4\pi}{5})\right) \\ \cos\left((2n+1)(\theta_r + \frac{4\pi}{5})\right) \\ \cos\left((2n+1)(\theta_r + \frac{2\pi}{5})\right) \end{bmatrix} \tag{4.8}$$

(4.7), which denotes the flux linkage due to the winding inductances, requires the definition of the inductance matrix, L_S. In Section 3.3.3, this matrix was already defined clearly. Both self and mutual components were calculated analytically and were verified experimentally.

In 4.8, total flux linkage created by permanent magnets is expressed as a sum of all odd harmonics. However, as can be seen in Figure 3.19b, fifth order harmonic component in the flux linkage is only 3% of the fundamental, where the ratio of higher order terms to the fundamental are even lower. Therefore, the harmonics of order larger than 5 is negligible in the system, only first and third harmonic components will be considered in total flux linkage calculation.

4.1.2 Transformation Matrices

To simplify the control of the drive system, the physical phase variable model of the PMSM should be transferred to a rotating reference frame. This mapping is achieved using Clarke and Park transformations. In conventional three-phase motor drives, phase variable model includes only the variables at fundamental electrical frequency, since there is no torque production capability of the 3-phase machines using higher order terms. In this design, flux linkage due to the magnets include significant third and fifth harmonic terms. Considering that for a five-phase system, fifth order harmonic line-to-line currents will not be observed, it is sufficient that the phase variable model includes only the first and third order terms.

In Figures 4.2a and 4.2b, space distribution of phasors representing each phase coil are given for two different rotating reference frames. Phasors corresponding to each coil can be mapped to a two-dimensional stationary coordinate system using Clarke transform. The mapped $\alpha\beta$ current vector, which consists of two vectors at different frequencies can be shown as in 4.9. This mapping basically performs a projection operation on the phasor vectors onto the two orthogonal vectors lying on the real and imaginary axes. This operation can also be expressed as a transformation matrix form, which will be denoted by T_c, in 4.10.

$$\boldsymbol{I_{\alpha\beta}} = \begin{bmatrix} i_{\alpha 1} & i_{\beta 1} & i_{\alpha 3} & i_{\beta 3} & i_0 \end{bmatrix}^t \tag{4.9}$$

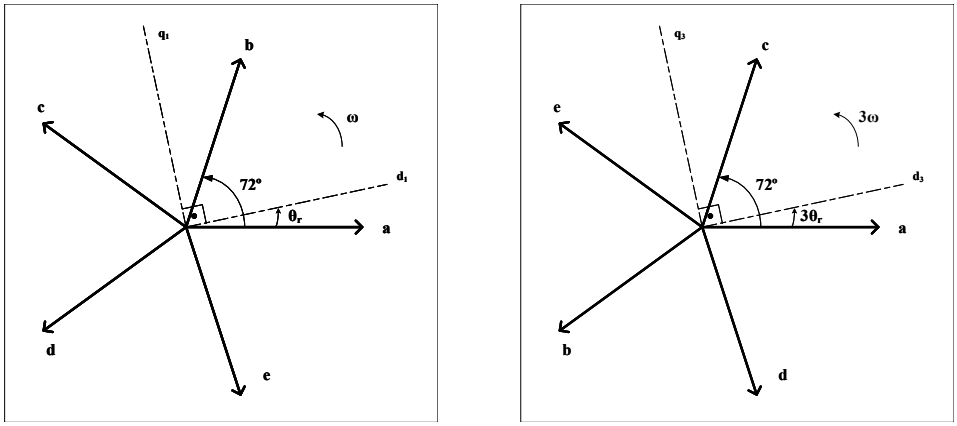

(a) D_1Q_1 Frame (b) D_3Q_3 Frame

Figure 4.2: Illustration of multifrequency rotating reference frames

Clarke transformation has several forms [53]. In this study, amplitude invariant transform method is adopted. Although this form of transformation matrix is not unitary (i.e. its transpose is not equal to its inverse), this method is more intuitive and convenient to determine the control loop parameters.

$$T_c = \frac{2}{5}\begin{bmatrix} \cos(0) & \cos\left(\frac{2\pi}{5}\right) & \cos\left(\frac{4\pi}{5}\right) & \cos\left(\frac{6\pi}{5}\right) & \cos\left(\frac{8\pi}{5}\right) \\ \sin(0) & \sin\left(\frac{2\pi}{5}\right) & \sin\left(\frac{4\pi}{5}\right) & \sin\left(\frac{6\pi}{5}\right) & \sin\left(\frac{8\pi}{5}\right) \\ \cos(0) & \cos\left(\frac{6\pi}{5}\right) & \cos\left(\frac{2\pi}{5}\right) & \cos\left(\frac{8\pi}{5}\right) & \cos\left(\frac{4\pi}{5}\right) \\ \sin(0) & \sin\left(\frac{6\pi}{5}\right) & \sin\left(\frac{2\pi}{5}\right) & \sin\left(\frac{8\pi}{5}\right) & \sin\left(\frac{4\pi}{5}\right) \\ \frac{1}{\sqrt{2}} & \frac{1}{\sqrt{2}} & \frac{1}{\sqrt{2}} & \frac{1}{\sqrt{2}} & \frac{1}{\sqrt{2}} \end{bmatrix} \tag{4.10}$$

$$\boldsymbol{I_{\alpha\beta}} = T_c\, \boldsymbol{I_s}$$

These frames are rotating with speeds of ω and 3ω respectively (where ω is the electrical rotation speed of the rotor), and their instantaneous positions with respect to their initial positions are θ_r and $3\theta_r$ (where θ_r is the electrical position of the rotor). In order to map the stationary frame to a multifrequency rotating frame, the Park transformation matrix, which will be denoted by T_p, in 4.12 can be used. Resultant current vector of this operation is defined as in 4.11.

$$\boldsymbol{I_{dq}} = \begin{bmatrix} i_{d1} & i_{q1} & i_{d3} & i_{q3} & i_0 \end{bmatrix}^t \tag{4.11}$$

$$T_p = \begin{bmatrix} \cos(\theta) & \sin(\theta) & 0 & 0 & 0 \\ -\sin(\theta) & \cos(\theta) & 0 & 0 & 0 \\ 0 & 0 & \cos(3\theta) & \sin(3\theta) & 0 \\ 0 & 0 & -\sin(3\theta) & \cos(3\theta) & 0 \\ 0 & 0 & 0 & 0 & 1 \end{bmatrix} \tag{4.12}$$

$$\boldsymbol{I_{dq}} = T_p \, \boldsymbol{I_{\alpha\beta}}$$

Combining the two matrices in 4.10 and 4.12, a single transformation matrix that maps phase variables two a multifrequency rotating reference frame can be obtained, as in 4.13, which will be denoted by T.

$$T = T_p T_c$$

$$= \frac{2}{5} \begin{bmatrix} \cos(\theta) & \cos\left(\theta - \frac{2\pi}{5}\right) & \cos\left(\theta - \frac{4\pi}{5}\right) & \cos\left(\theta - \frac{6\pi}{5}\right) & \cos\left(\theta - \frac{8\pi}{5}\right) \\ -\sin(\theta) & -\sin\left(\theta - \frac{2\pi}{5}\right) & -\sin\left(\theta - \frac{4\pi}{5}\right) & -\sin\left(\theta - \frac{6\pi}{5}\right) & -\sin\left(\theta - \frac{8\pi}{5}\right) \\ \cos(3\theta) & \cos\left(3\theta - \frac{6\pi}{5}\right) & \cos\left(3\theta - \frac{2\pi}{5}\right) & \cos\left(3\theta - \frac{8\pi}{5}\right) & \cos\left(3\theta - \frac{4\pi}{5}\right) \\ -\sin(3\theta) & -\sin\left(3\theta - \frac{6\pi}{5}\right) & -\sin\left(3\theta - \frac{2\pi}{5}\right) & -\sin\left(3\theta - \frac{8\pi}{5}\right) & -\sin\left(3\theta - \frac{4\pi}{5}\right) \\ \frac{1}{\sqrt{2}} & \frac{1}{\sqrt{2}} & \frac{1}{\sqrt{2}} & \frac{1}{\sqrt{2}} & \frac{1}{\sqrt{2}} \end{bmatrix} \tag{4.13}$$

$$\boldsymbol{I_{dq}} = T \boldsymbol{I_s}$$

Noting that 4.13 is orthogonal and Eq. 4.14 should be satisfied, its inverse transform matrix can be obtained as in 4.15.

$$\frac{5}{2} T^t T = T^{-1} T = I_{(5\times5)} \tag{4.14}$$

$$T^{-1} = \begin{bmatrix} \cos(\theta) & -\sin(\theta) & \cos(3\theta) & -\sin(3\theta) & \frac{1}{\sqrt{2}} \\ \cos\left(\theta - \frac{2\pi}{5}\right) & -\sin\left(\theta - \frac{2\pi}{5}\right) & \cos\left(3\theta - \frac{6\pi}{5}\right) & -\sin\left(3\theta - \frac{6\pi}{5}\right) & \frac{1}{\sqrt{2}} \\ \cos\left(\theta - \frac{4\pi}{5}\right) & -\sin\left(\theta - \frac{4\pi}{5}\right) & \cos\left(3\theta - \frac{2\pi}{5}\right) & -\sin\left(3\theta - \frac{2\pi}{5}\right) & \frac{1}{\sqrt{2}} \\ \cos\left(\theta - \frac{6\pi}{5}\right) & -\sin\left(\theta - \frac{6\pi}{5}\right) & \cos\left(3\theta - \frac{8\pi}{5}\right) & -\sin\left(3\theta - \frac{8\pi}{5}\right) & \frac{1}{\sqrt{2}} \\ \cos\left(\theta - \frac{8\pi}{5}\right) & -\sin\left(\theta - \frac{8\pi}{5}\right) & \cos\left(3\theta - \frac{4\pi}{5}\right) & -\sin\left(3\theta - \frac{4\pi}{5}\right) & \frac{1}{\sqrt{2}} \end{bmatrix} \tag{4.15}$$

4.1.3 Derivation of the Electromagnetic Torque

Output torque of the machine can be obtained by taking the derivative of magnetic co-energy, with respect to the electrical rotor angle. For magnetically insalient topologies (such as air-cored SMPM synchronous machines), machine inductances do not depend on the rotor angle (i.e. $L_d = L_q$). Therefore, for such configurations, the output torque consists only of the Lorentz torque, but not the reluctance torque, as in 4.16.

$$\begin{aligned} T_e = \frac{\partial W'}{\partial \theta} &= P\left(\frac{1}{2}{\mathbf{I_s}}^t \frac{\partial L_s}{\partial \theta}\mathbf{I_s} + {\mathbf{I_s}}^t \frac{\partial \mathbf{\Lambda_{PM}}}{\partial \theta}\right) \\ &= P\left({\mathbf{I_s}}^t \frac{\partial \mathbf{\Lambda_{PM}}}{\partial \theta}\right) \end{aligned} \tag{4.16}$$

The torque equation can also be written by means of the flux linkage and currents in DQ domain. Using 4.14 and 4.16, this version of the equation is obtained as in 4.17.

$$\begin{aligned} T_e &= P\left({\mathbf{I_s}}^t \frac{5}{2} T^t \, T \frac{\partial \mathbf{\Lambda_s}}{\partial \theta}\right) \\ &= \frac{5P}{2}{\mathbf{I_{dq}}}^t \begin{bmatrix} 0 & -1 & 0 & 0 & 0 \\ 1 & 0 & 0 & 0 & 0 \\ 0 & 0 & 0 & -3 & 0 \\ 0 & 0 & 3 & 0 & 0 \\ 0 & 0 & 0 & 0 & 0 \end{bmatrix} \mathbf{\Lambda_{dq}} \\ &= \frac{5P}{2}\left(\lambda_{d1} i_{q1} - \lambda_{q1} i_{d1} + 3\lambda_{d3} i_{q3} - 3\lambda_{q3} i_{d3}\right) \end{aligned} \tag{4.17}$$

4.2 Simulation Results

To observe the actual system behavior, it is essential to perform simulations. Having simulated the machine using FEM, the resulting parameters are used to built a motor drive model in Simulink, so that the whole system dynamics and behavior can be observed. This section summarizes both simulation models' results and compares them with the analytically calculated ones.

4.2.1 Drive Simulation in Simulink

To observe the behavior of the overall drive system and to test the machine under the closed-loop control structure, the drive system is modelled in Simulink. The main structure of this simulation model is presented in Figure 4.3.

The system consists of two main control loops. The outer loop controls the speed, with a PID controller and the inner loop controls the phase currents (referred to the rotating reference frame), with PI controllers. Similar to the real-life implementation of the system, current and rotor position measurements are essential for the closed-loop operation.

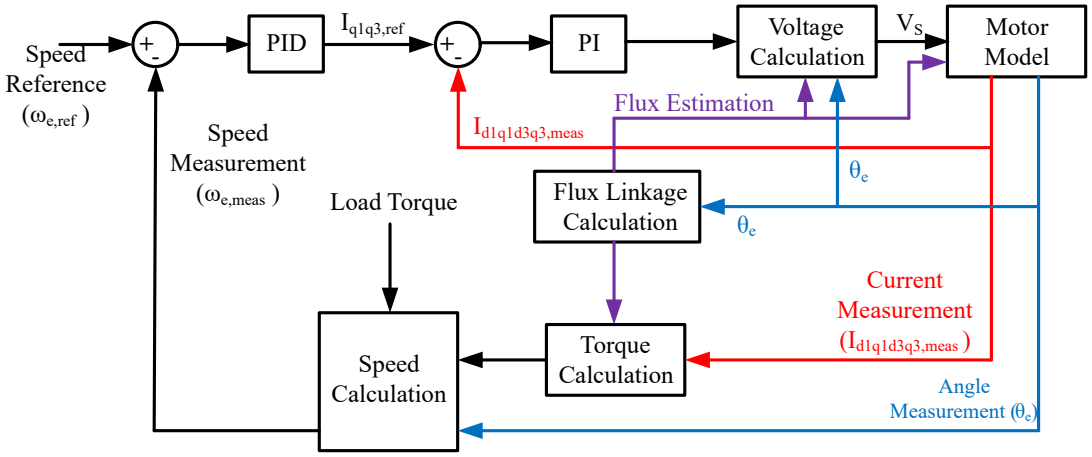

Figure 4.3: Structure of the Simulink Model of the Motor Drive

Functions of each block in the block diagram given in Figure 4.3 can be summarized as follows:

- **Speed reference:** A numerical value that provides the reference rotor speed in rad/sec.
- **Load torque:** A numerical value that represents the fictitious external torque.
- **Speed calculation:** Torque balance equation that calculates the speed as the time integral of angular acceleration.
- **Torque calculation:** The equation given in 4.17.

- **Flux linkage calculation:** Sum of the flux linkage due to the PMs and due to the stator inductance (4.6). These values are the ones obtained via FEA.
- **Motor model:** The primitive electrical model of the machine and the inverter. It composes of five-phase coupled inductors, phase resistances and a voltage source that represents the phase back EMF and is obtained using 4.6, as well as an inverter that is composed of five half-bridge legs.
- **Current and speed controllers:** PI and PID controllers, respectively.
- **Votlage calculation:** A feed-forward block to improve the transient performance of the motor in the simulation. This block calculates the input voltage to the machine with respect to the reference current values, using 5.1.

The main differences of the structure of this model from its real-life form are the voltage feed-forward and consequently its transient response. Due to the computational cost of the voltage feed-forward, that part are not be implemented. As a result, tuning of the controllers are re-performed accordingly. PI and PID parameters have been tuned using Ziegler-Nichols method initially, and then enhanced by trial-and-error.

With this model, the operation of the electric drive at rated speed and rated output torque have been simulated. Furthermore, a speed reversal scenario is also simulated to observe the transient response of the drive under a speed change from half of the rated speed in forward direction, to the same speed in the reverse direction. The results are compatible with the ones obtained analytically.

4.2.1.1 Operation at the Rated Speed

In this simulation, speed reference is increased stepwise. With the current limit of 30 A_{peak}, the system can be said to settle in 1 sec. Figure 4.4 shows the phase current waveforms at this operation, with both the overall trend and the zoom-in waveforms. In Figure 4.4a, the speed-up trend of the motor can be observed in large current regions. In addition to that, the effect of low inductance (and high oscillation due to switching) is seen in Figure 4.4d, which is especially more dominant in no-load operating points.

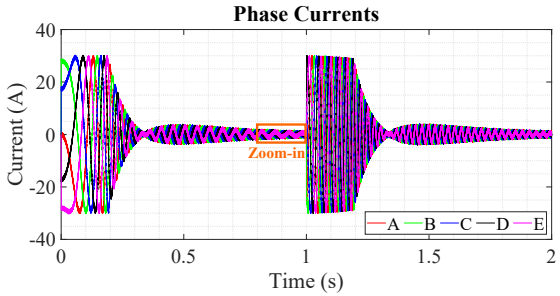

(a) Full-scale

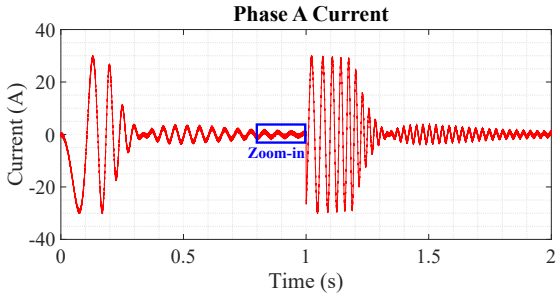

(b) Full-scale, Only Phase A

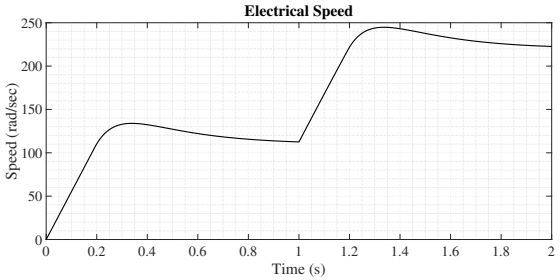

(c) Electrical Speed

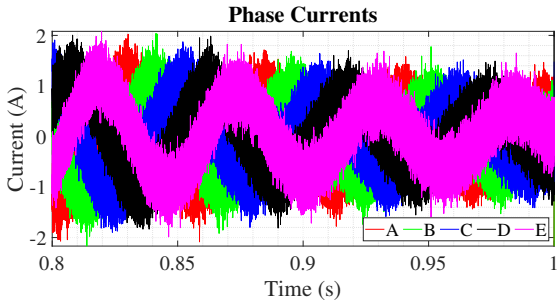

(d) Zoom-in

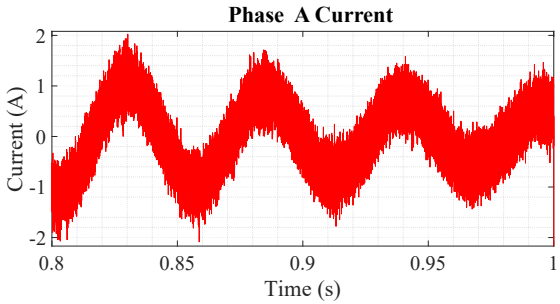

(e) Zoom-in, Only Phase A

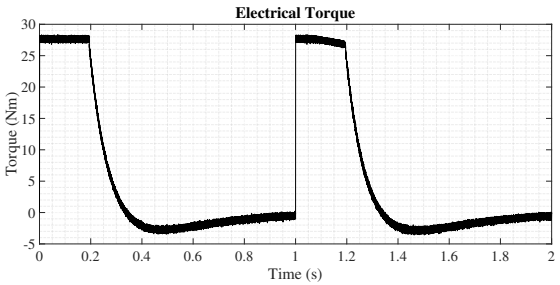

(f) Torque

Figure 4.4: Phase Currents, Output Torque and Speed For Full-Speed Operation, Obtained with Simulink

Figure 4.4 also shows the output torque and speed of the machine under these circumstances.Their values are in a very good agreement with the analytically calculated ones. Also, for this simulation, the transient period is not more that 1 sec.

To convert the phase currents to the rotating reference frame, DQ-values of them can be easily calculated and shown as in Figure 4.5. Not surprisingly, Q1 current has a similar trend to the output torque, as they are directly in relation with each other. Other components remain around 0 A, as no third-harmonic injection or field-weakening are necessary at this point.

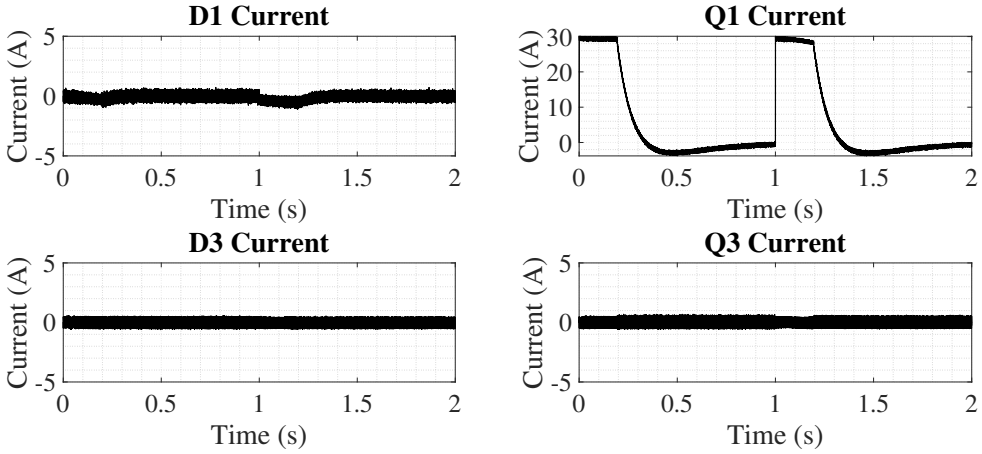

Figure 4.5: DQ Currents For Full-Speed Operation, Obtained with Simulink

4.2.1.2 Operation at Rated Torque

Rated torque operation has been verified by increasing the load torque stepwise, similar to the rated speed operation. For these simulations, motor inertia is taken as 0.2 $kg.m^2$, which is in fact an approximate value of the rotor inertia, where the mechanical coupling elements and the load generator in the real system are out of consideration. It should be noted that this value is expected to be higher considering the effects of the friction, inertia of the loading machine's shaft and the effects of mechanical coupling elements. The real inertia value can be calculated by observing the step response of the shaft speed of the machine. For now, as the simulation is done as a proof of concept, such a discrepancy would be acceptable.

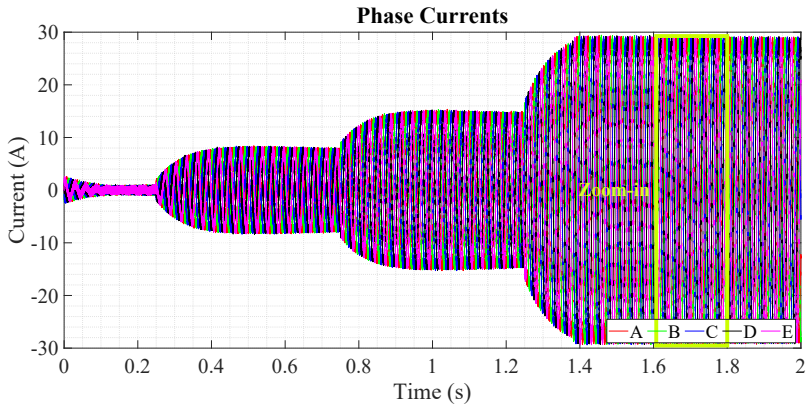

(a) Full-scale

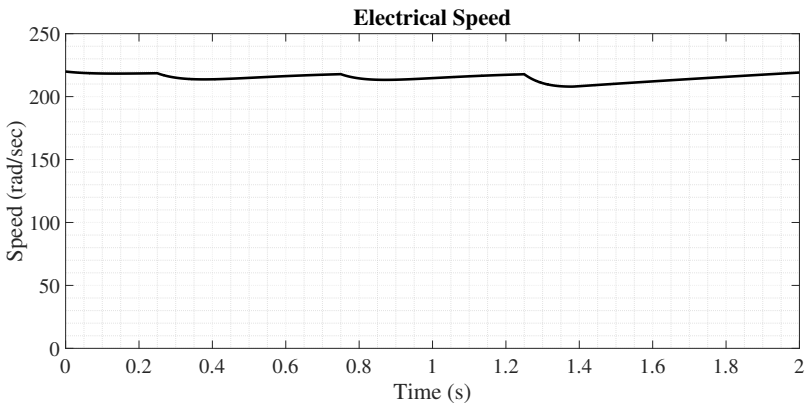

(b) Electrical Speed

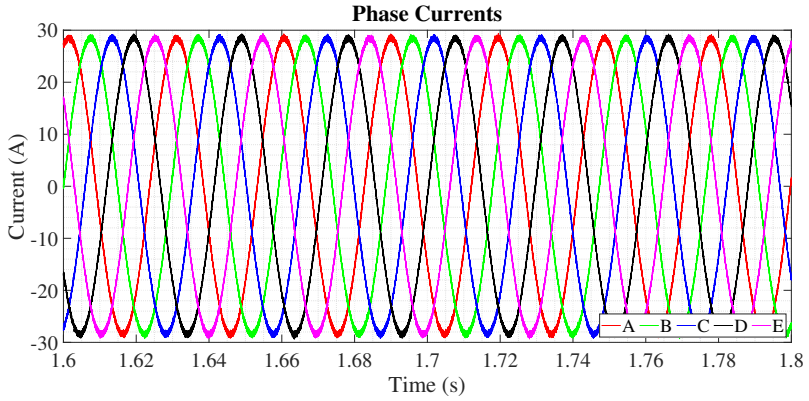

(c) Zoom-in

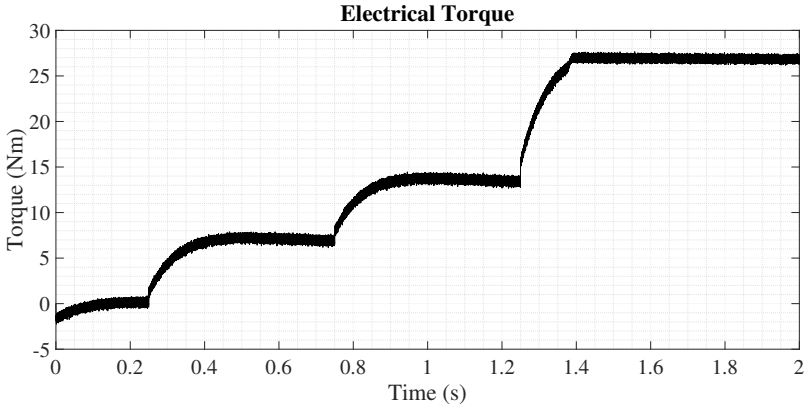

(d) Torque

Figure 4.6: Phase Currents, Output Torque and Speed For Full-Load Operation, Obtained with Simulink

The phase currents, DQ currents, output torque and speed graphs for this operation are shown in Figure 4.6. Having obtained similar results to the previous part, it can be said that the effect of low inductance on the phase currents are less dominant in Figure 4.4d compared to Figure 4.4d.

It is also worth to mention that in the closed loop system, the fluctuation of D1 current in the transient period for this case is lower than in previous case. This can be seen by simply comparing Figures 4.5 and 4.7. That is because, the output of the Q1 current controller does not saturate for this operation. In the case of saturation of Q1 current, the system cannot provide the desired torque to the machine and delays the speed to reach its set point. The saturation of the controllers are necessary to protect the equipment. However, they introduce additional non-linearity to the system, may cause stability issues and contravene the operation of the other controllers with the whole system.

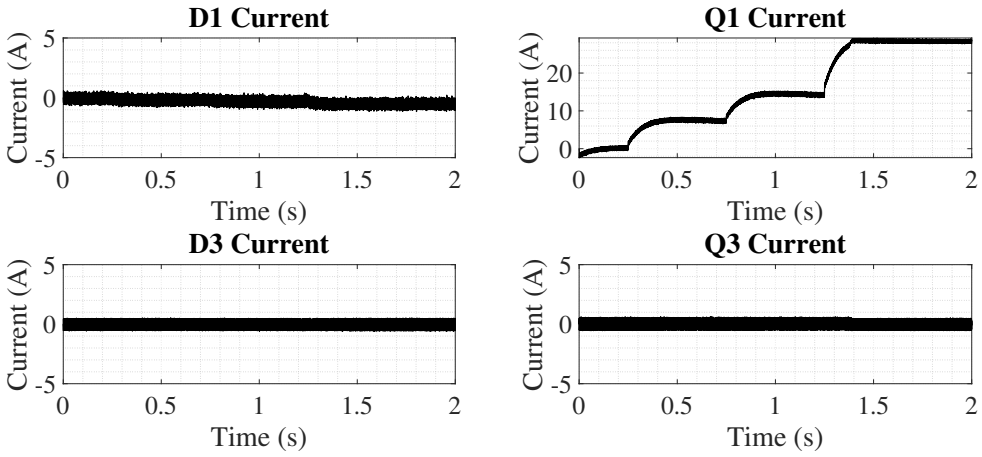

Figure 4.7: DQ Currents For Full-Load Operation, Obtained with Simulink

4.2.1.3 Speed Reversal

Another test case for the transient performance of the motor drive is the speed reversal scenario. Phase current, DQ current and torque-speed waveforms for this test case are present in Figure 4.8 and 4.9. Because of a fast change in the speed set point, the drive operates at the current limit for a significant amount of time. For that reason, the fluctuation of D1 current can also be observed in Figure 4.9.

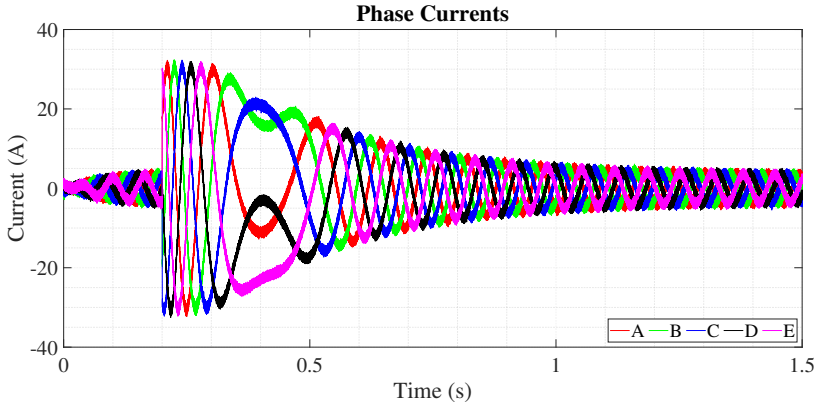

(a) Phase Currents

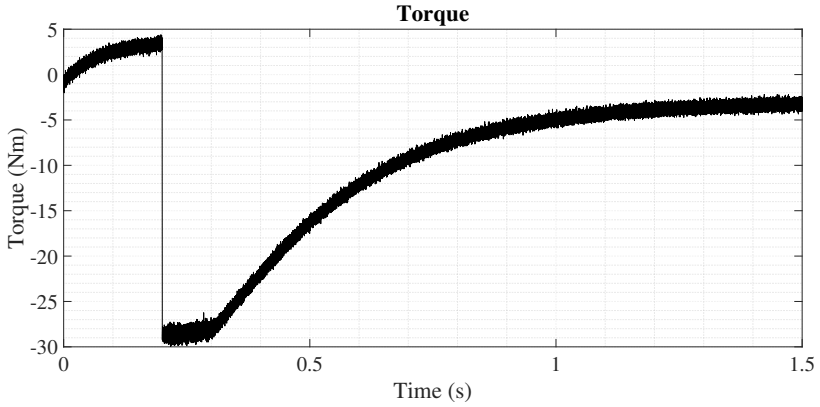

(b) Torque

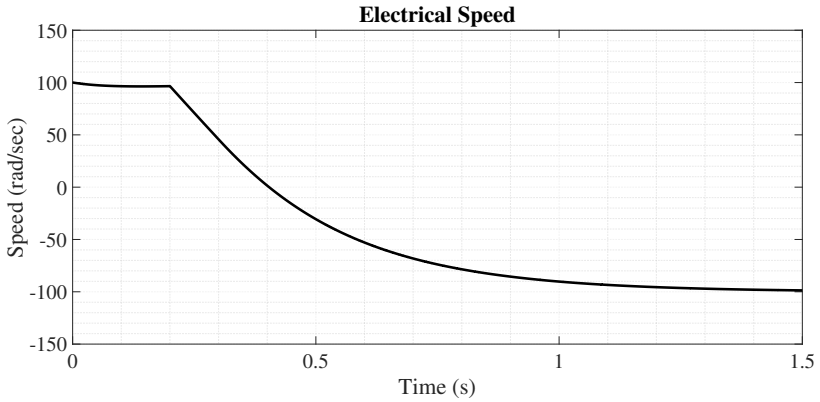

(c) Electrical Speed

Figure 4.8: Machine Torque and Speed For Speed-Reversal Operation Between 100 and -100 rad/s, Obtained with Simulink

Due to the fast change in the speed set point, the speed controller must also include an anti windup property. Otherwise, the accumulation of the error in the integral term of the controller may grow large to undesirable levels. This would definitely cause instability and the output diverges. For this simulation model, back-calculation is used as the anti windup method of choice.

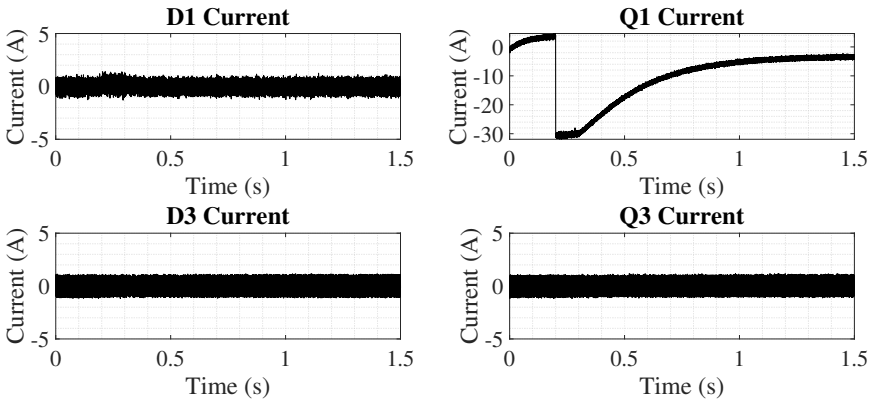

Figure 4.9: DQ Currents For Speed-Reversal Operation Between 100 and -100 rad/s, Obtained with Simulink

4.2.1.4 The Effect of Third Harmonic Current

One of the major benefits of five-phase electric machines is torque producing capability of third order flux linkage and phase currents. In a five-phase machine, a desired torque value can be achieved with a lower peak current value using third harmonic injection technique. Or similarly, the torque can be enhanced with third harmonic injection [54].

This case has also been verified in the drive simulation. Given in Figure 4.10, peak-to-peak value of the phase current decreases with a 14% third harmonic current injection, where the transient and steady state torque values remain the same in the case where the phase current composes only of fundamental order currents.

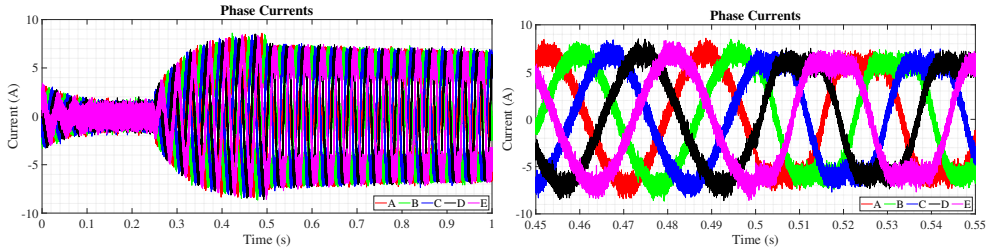

(a) Full-scale (b) Zoom-in

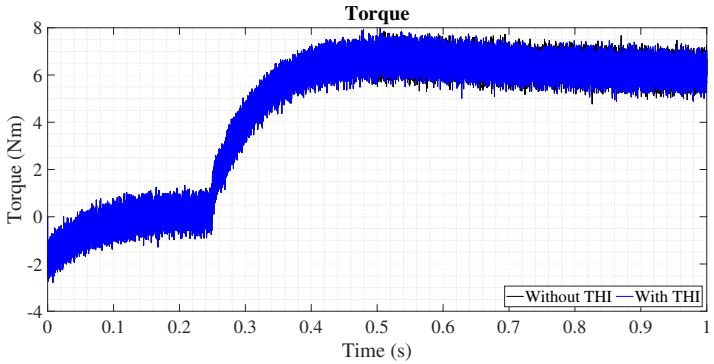

(c) Torque

Figure 4.10: Machine Performance Parameters For 14% Third-Harmonic Injection Operation, Obtained with Simulink

4.2.1.5 Conclusions of the Simulation Cases

Having shown and discussed the results of each simulation case, a short summary of these discussions is worthy. In fact, these simulations show that the model is consistent and sufficient as an analytical implication of the drive system. They are also essential since they provide the observation of closed-loop operation of the drive with continuously changing reference and measurement values. With these simulations, several variables such as phase current and output torque are verified consistently with pre-defined phase variables, such as induced EMF, speed and input voltage. In the next section, as the experimental results will be presented, these results will also be compared by means of accuracy on top of the consistency.

There are also several conclusions that can be drawn from these studies in control theory point of view. In the drive simulations, the transient response of the system has been quite fast. The main reason for that is the voltage feed-forward path that

calculates reference voltages using reference current, machine model and flux estimation. In the experimental implementation, this feed-forward mechanism is not be adopted to reduce the computational burden. Based upon the results in this chapter, it can be easily said that the settling time in the experiments would be definitely higher. On top of that, in the experimental setup, the current references directly determines the duty cycles of the switches, also with a saturation condition between 0 and 1. Due to this fact, PI and PID controllers should be re-tuned. Rather than trial-and-error method adopted in the drive simulation model, these parameters should be determined methodologically, using classical control theory methods such as Ziegler-Nichols. Lastly, for all controllers that include an integral term, the use of anti windup method is crucial in order to preserve the system stability. Otherwise, either speed or phase currents may grow large and diverge, which would definitely cause severe damages especially on the inverter.

4.3 Experimental Verification: Operation of the Drive System Under Normal Operating Conditions

In Chapter 3, operations and the design of the machine and the inverter of the five-phase motor drive were experimentally validated. In this section, after having defined the analytical model for a five-phase drive and having it simulated in Simulink environment, the operation of the drive system will be verified on the test-bed for several operating conditions.

In Figure 4.11, general structure of the test bed is shown, front (Figure 4.11a) and back (Figure 4.11b). The setup mainly consists of data acquisition devices, sensors, driving circuit, loading machine and the five-phase AFPMSM itself. The specifications of the devices can be summarized as follows:

- **DC Power Supply:** Maximum current rating of 60 A and maximum power rating of 20 kW. This supply allows bidirectional power flow. That is, there is no need to use of an external braking resistor for braking operations of the machine.
- **4-Ch DSO:** This DSO provides high resolution data acquisition and online

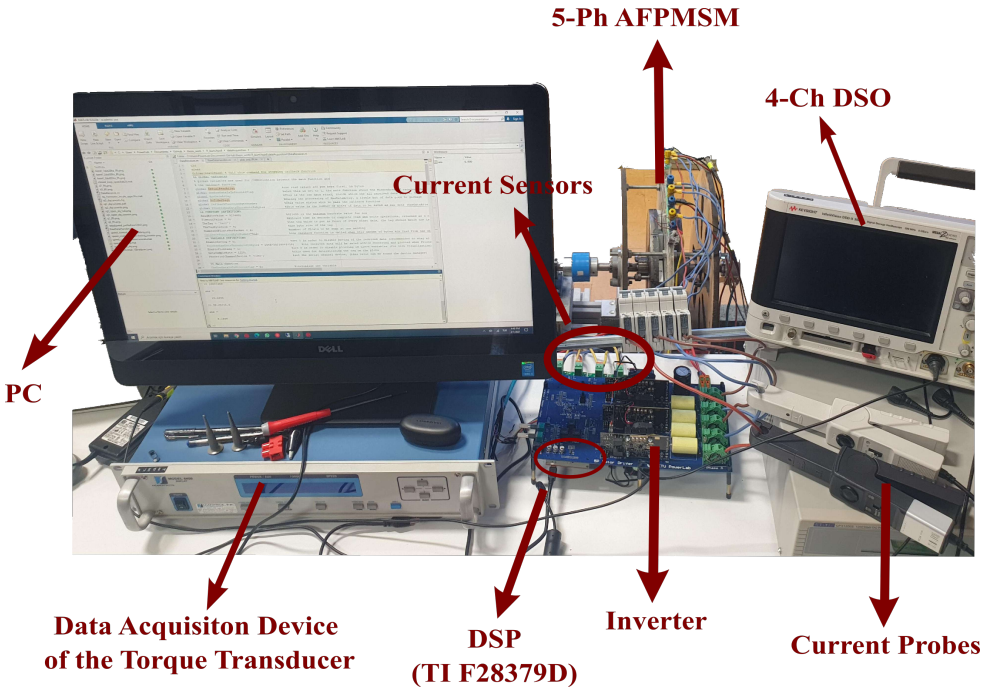

(a) Front View

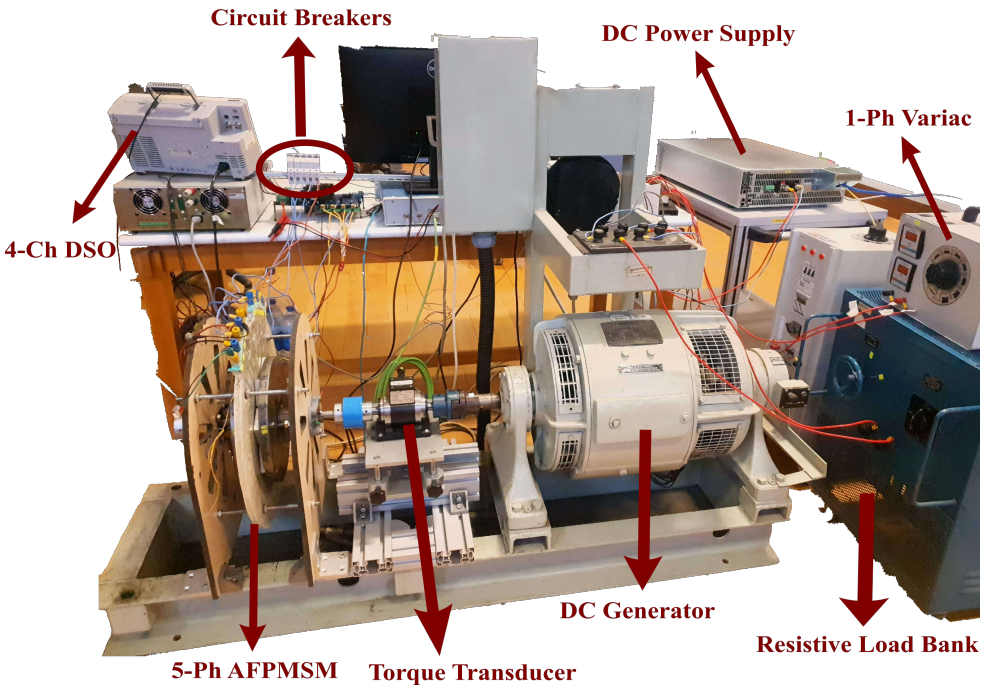

(b) Back View

Figure 4.11: Test Bench for Motoring Mode Tests

FFT property. For several experiments, two DSOs are used for both current and torque measurements.

- **Torque Transducer:** This sensor has an additional data acquisition devices, which has both a built-in user interface and an analog voltage output that provides 50 mV of output voltage per 1 Nm. The voltage output is recorded through an analog low-pass filter with unity gain, in order to eliminate the measurement noise.

- **PC:** The PC and the IDE of the DSP, Code Composer Studio, are used to provide the control commands to the DSP. Also, the current measurements obtained by the current sensors (that are placed on the inverter) are recorded using the serial communication interface of the PC and Matlab.

- **DC Generator:** This machine has a power rating of 11.2 kW, rated speed of 1200 rpm. The field current of the machine is controlled with the rectified output of a single-phase variac. Armature terminals of the machine are connected to a 4.8 kW, 12 Ω resistive load bank.

- **Circuit Breakers:** These are five single-phase fuses with a current rating of 30 A. The circuit breakers are used to generate an open circuit fault in the system.

The operation of the five-phase AFPMSM will be observed for no-load and loaded cases. Also, the transient performance of the machine and the controller will be shown for a case of speed reversal. Besides, the effect of third harmonic current injection will also be discussed throughout this section. For all these operation types, the machine is closed-loop speed controlled with FOC. As the base speed value is not exceeded in any of these experiments, D1 and D3 reference values are set to 0. Q1 reference is dependent on the output of the speed controller. For third harmonic current injection case, Q3 reference is also set depending on the output of the speed controller. For the other cases, Q3 reference is set to 0.

Also, it should be noted that the phase currents and the output torque are recorded using two four channel DSOs; DQ currents and electrical speed are recorded a user interface designed in MATLAB, where the data is obtained via the serial communication port of the DSP. That is why, time axes for phase currents and the output torque

start at a negative value and the ones for DQ currents and the electrical speed start at 0.

4.3.1 No-Load Operation

Initially, the 5-Ph AFPMSM is driven under no-load, at 180 rad/sec. The rated speed of the machine is 220 rad/sec. However, especially under loaded conditions, speeding up the machine beyond 180 rad/sec becomes impossible due to limited DC bus voltage. (Bus voltage is limited at 50 V. Exceeding this value caused the inverter's evaluation board to get in the error mode several times. To experiment in a safe region for the board and GaN HEMTs, this DC bus voltage value is not surpassed.) Therefore, all of the experiments are performed at 180 rad/sec electrical speed.

The output torque, electrical speed, phase currents and DQ currents at no-load operation are presented in Figure 4.12. For this operation, the machine produces a small torque just for friction. Accordingly, the phase current amplitudes and the Q1 current have also small amplitudes in proportional with the output torque. D1, D3 and Q3 current values remain at 0, following their set points.

We can also observe that at no-load, the damping effect of the mechanical system is also negligible. Therefore, the phase current waveforms are quite oscillatory.

In Figure 4.13, the simulation results for the same operating point as in Figure 4.12 are given. Comparing both results, it can be said that they are in good agreement with each other. For both cases, the machine draws around 2 A (peak) phase current at no-load, 180 rad/s speed. It should also be noted that phase currents obtained via simulation look noisier than the experimental results, since there are additional digital filters in the experimental data acquisition system to eliminate the measurement noises.

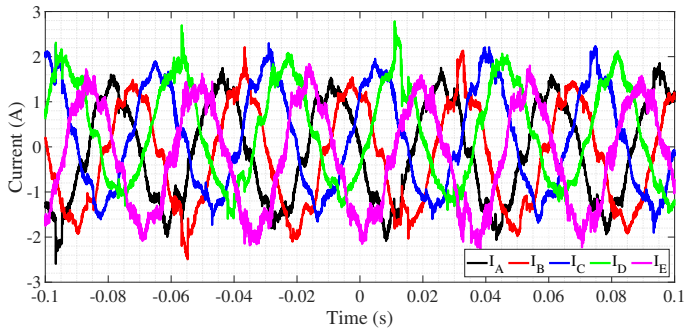

(a) Phase Currents

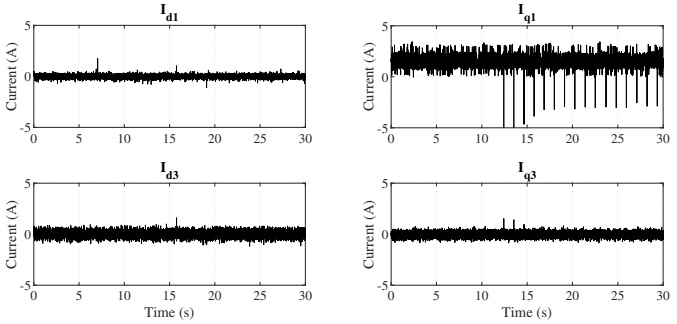

(b) DQ Currents

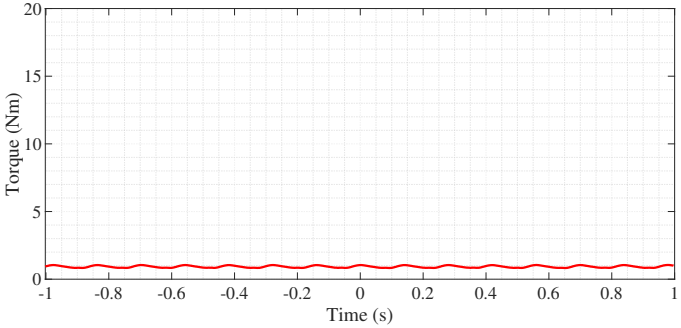

(c) Torque

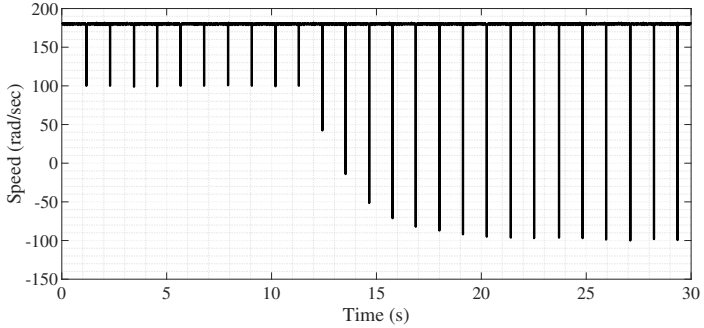

(d) Electrical Speed

Figure 4.12: Experimental Results: Motor Performance Parameters at No-Load Operation

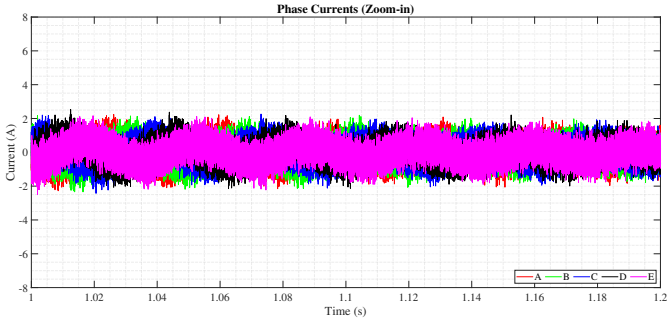

(a) Phase Currents

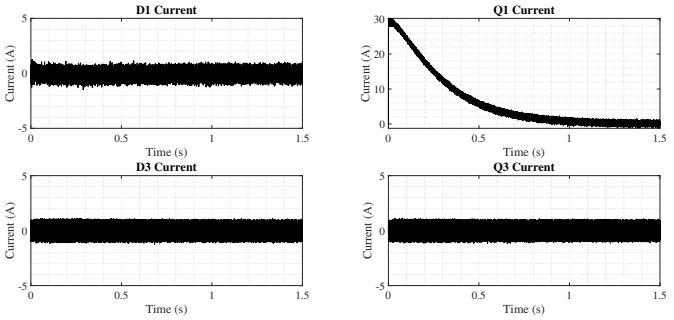

(b) DQ Currents

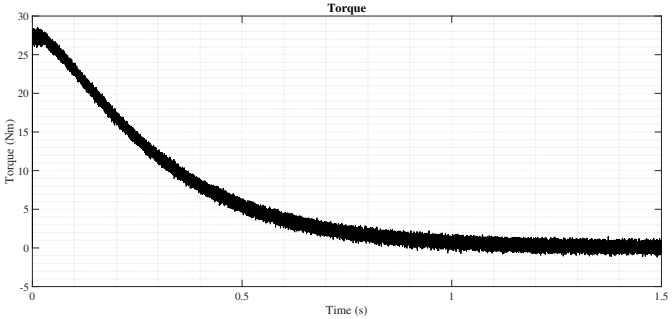

(c) Torque

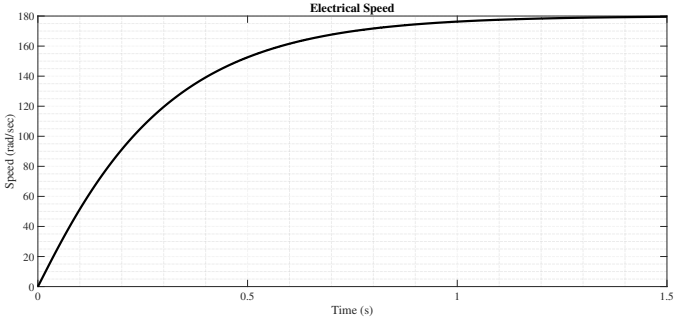

(d) Electrical Speed

Figure 4.13: Simulation Results: Motor Performance Parameters at No-Load Operation at the Same Operating Point with the Experiment (180 rad/s)

4.3.2 Loaded Operation

After no-load operation, the 5-Ph AFPMSM is loaded by increasing the field current of the DC generator. As explained in the previous subsection, due to the limitation caused by DC bus voltage, the maximum available loading level is 20 Nm at 180 rad/sec.

Phase current, output torque and DQ current waveforms for the load levels of 6 Nm, 13.5 Nm and 20 Nm are presented in Figures 4.14, 4.16 and 4.18, respectively. In the figures, it can be clearly seen that the DQ currents easily keep up with the current references thanks to well-tuned controllers. Similar to the previous section, the reference values for D1, D3 and Q3 are 0, where the reference of Q1 is determined by the output of the speed controller.

In Figures 4.15, 4.17 and 4.19 the simulation results for the same operating point as in Figures 4.14, 4.16 and 4.18 are given, respectively. Comparing both results, it can be said that they are in good agreement with each other. In general, it is observed that peak phase currents in simulations are higher for the experiment at the same operating point. The main reason for that is the effect of the switching increases the peak of the phase current as there is third order components in the system and this results in a noisy peak in the phase current. This noise is eliminated mostly in the experimental results, thanks to the digital filters in the experimental data acquisition tools.

With increasing load level, the damping effect of the mechanical system increases and the oscillatory/noisy behavior of the phase current waveform decreases. Also, with increasing load level, the temperature of the inverter and the windings increase. The temperature change and the load profile are shown in Figure 4.20, with respect to the time. When the load torque is kept constant, the increase rate of the winding temperature decreases and it is expected not to exceed 50-55°C after more than 60-min-operation. This temperature value is also quite safe for the structure of the stator and the PMs.

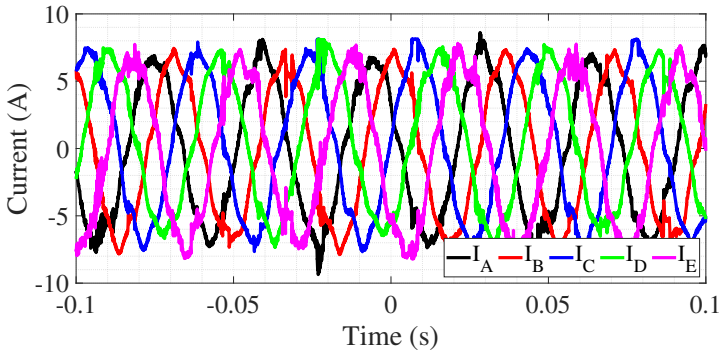

(a) Phase Currents

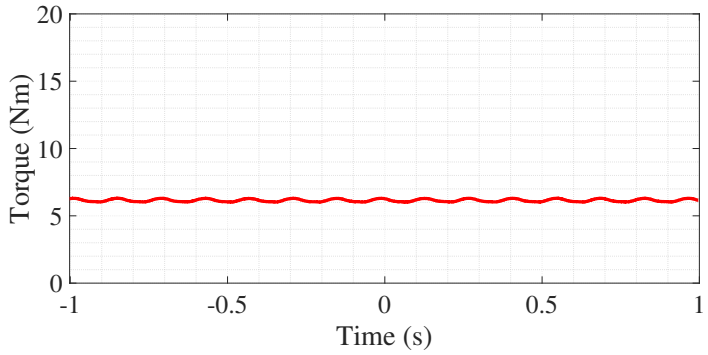

(b) Torque

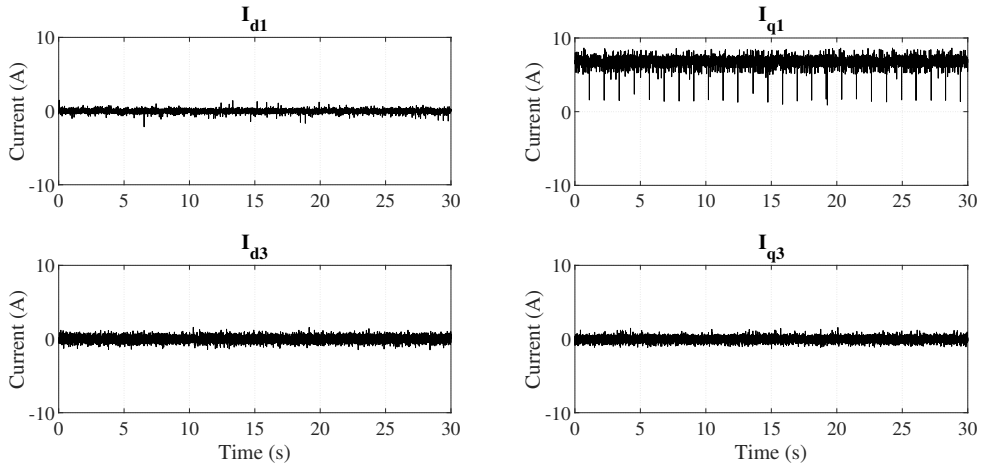

(c) DQ Currents

Figure 4.14: Experimental Results: Motor Performance Parameters at 6 Nm Loaded Operation

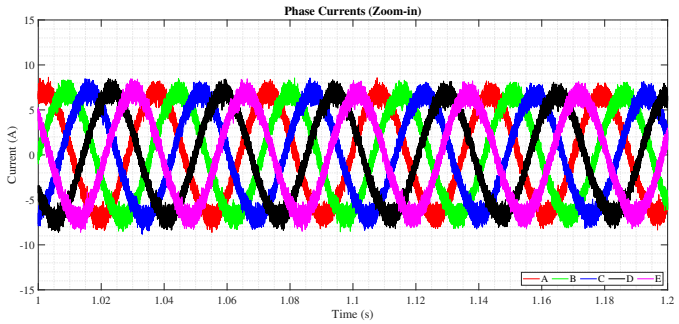

(a) Phase Currents

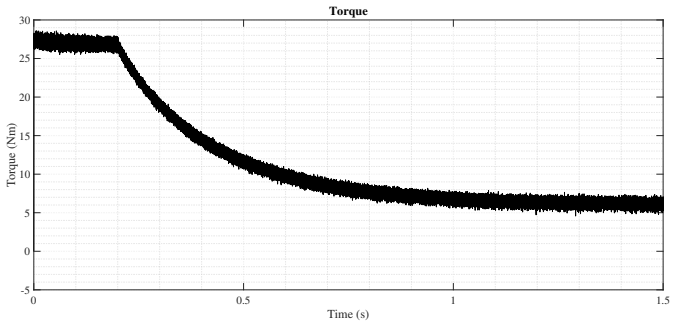

(b) Torque

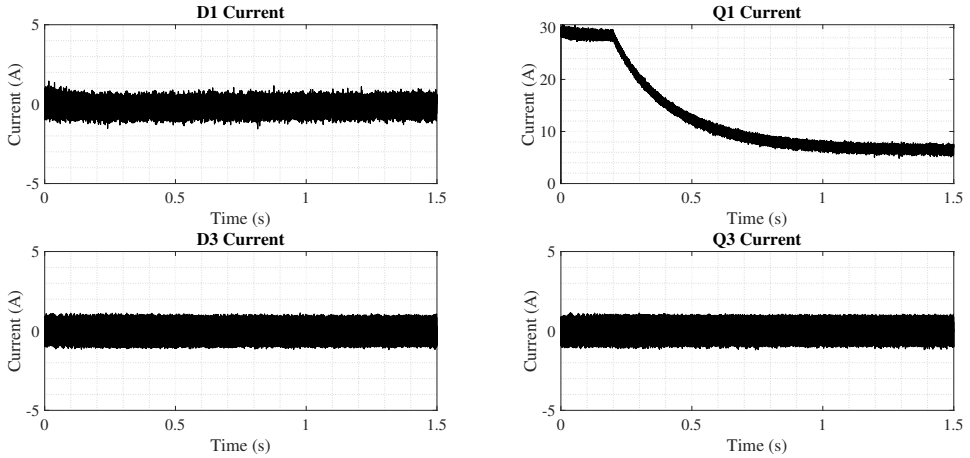

(c) DQ Currents

Figure 4.15: Simulation Results: Motor Performance Parameters at 6 Nm Loaded Operation at the Same Operating Point with the Experiment (180 rad/s)

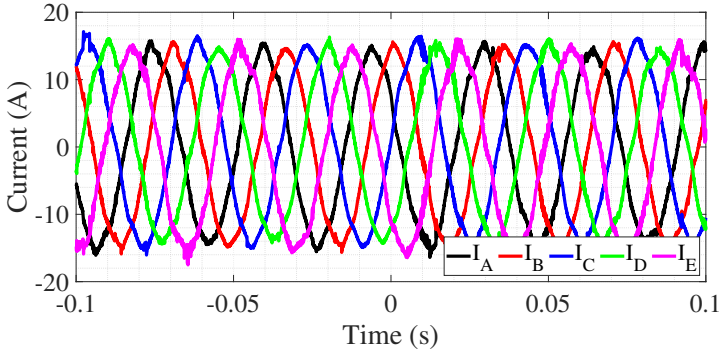

(a) Phase Currents

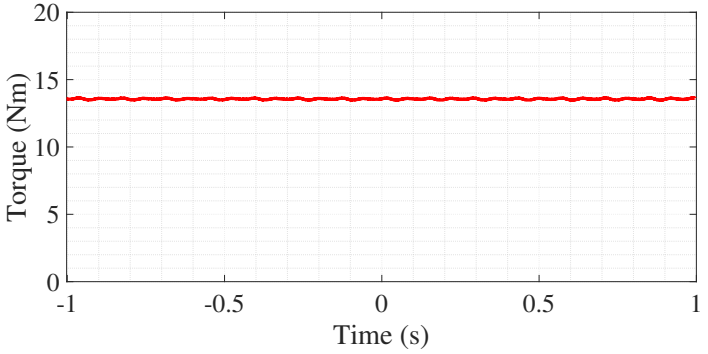

(b) Torque

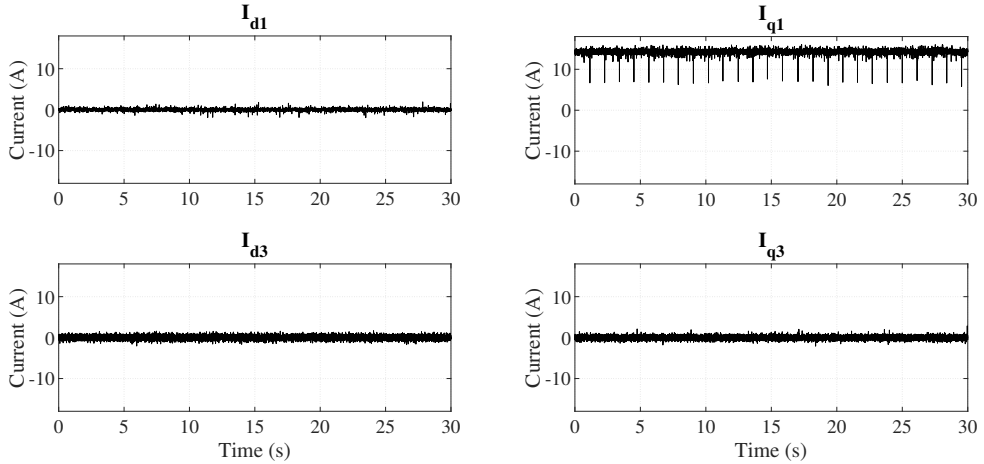

(c) DQ Currents

Figure 4.16: Experimental Results: Motor Performance Parameters at 13 Nm (Half) Loaded Operation

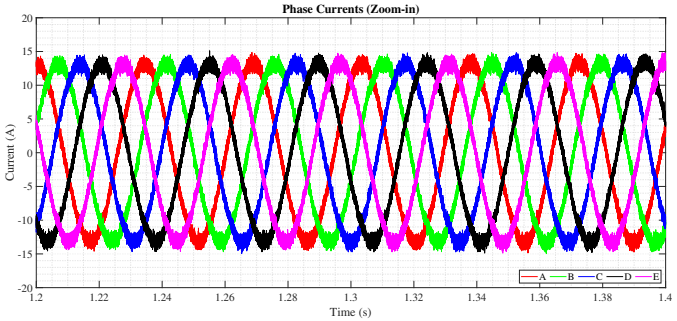

(a) Phase Currents

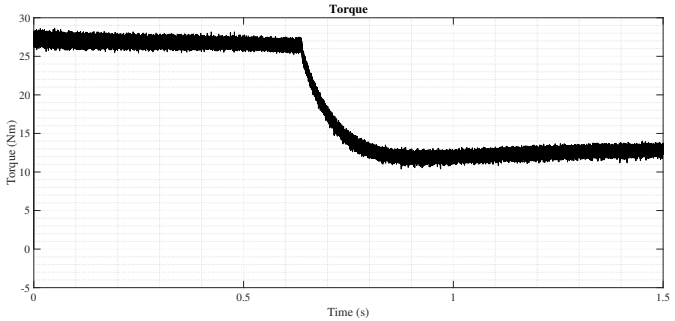

(b) Torque

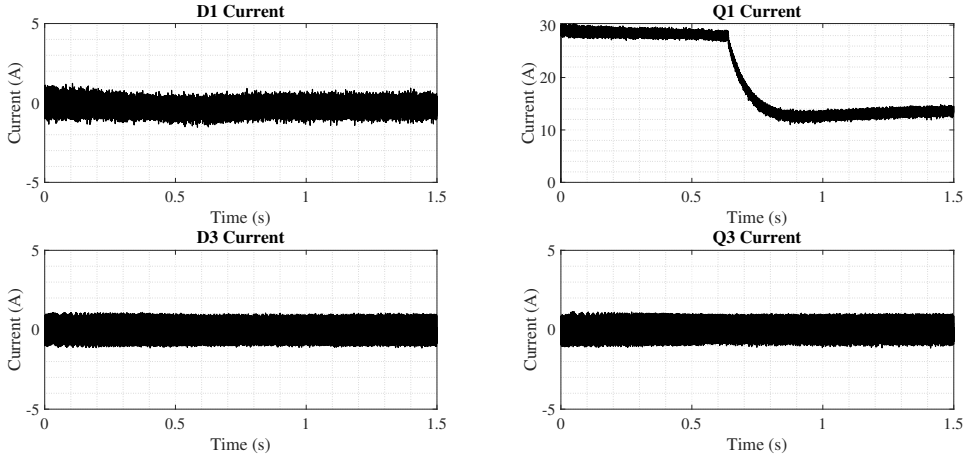

(c) DQ Currents

Figure 4.17: Simulation Results: Motor Performance Parameters at 13 Nm (Half of the Rated)Loaded Operation at the Same Operating Point with the Experiment (180 rad/s)

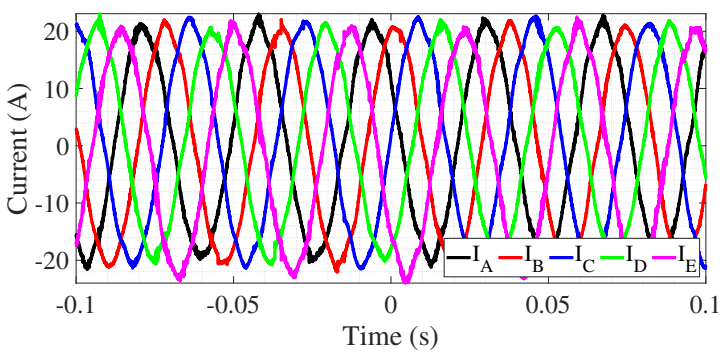

(a) Phase Currents

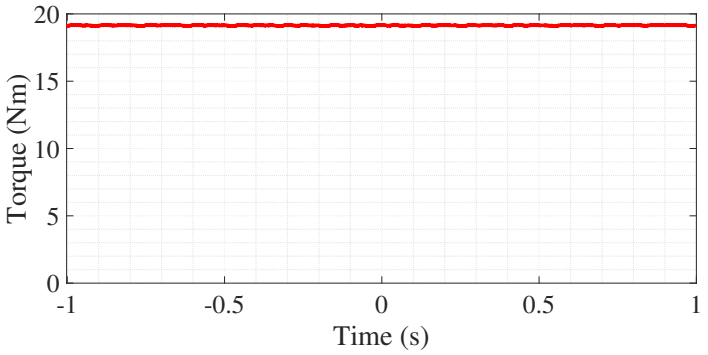

(b) Torque

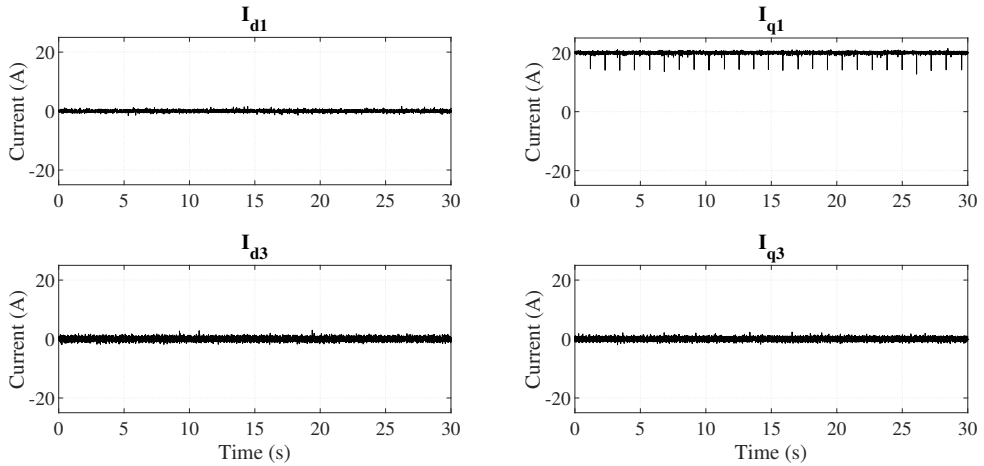

(c) DQ Currents

Figure 4.18: Experimental Results: Motor Performance Parameters at 20 Nm Loaded Operation

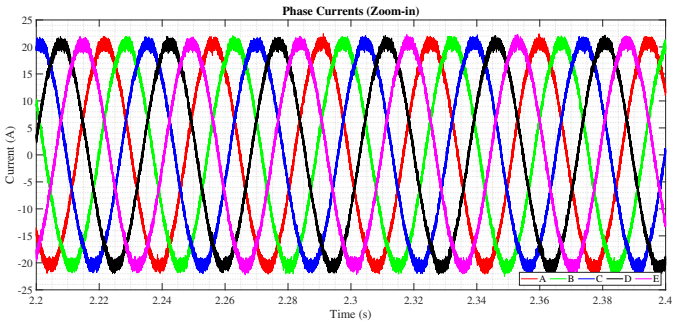

(a) Phase Currents

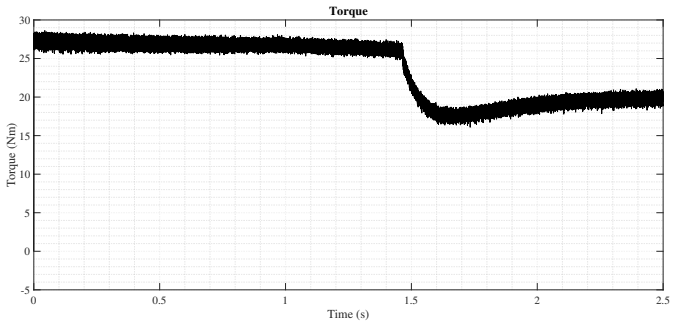

(b) Torque

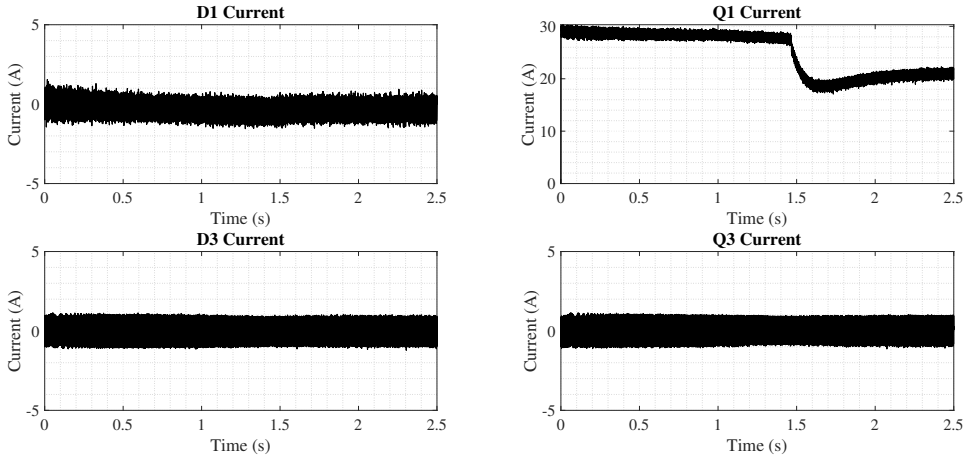

(c) DQ Currents

Figure 4.19: Simulation Results: Motor Performance Parameters at 20 Nm Loaded Operation at the Same Operating Point with the Experiment (180 rad/s)

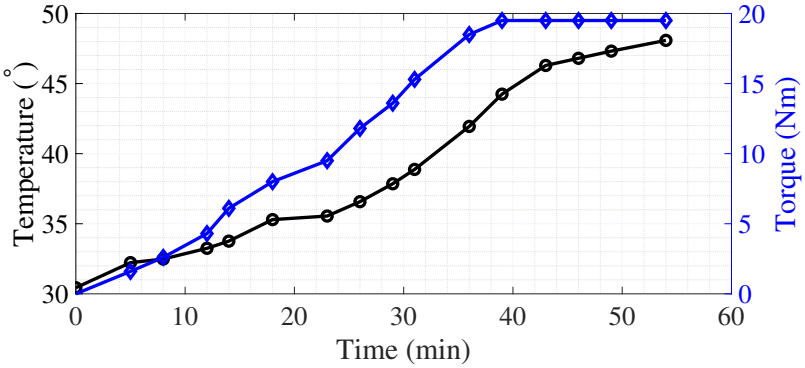

Figure 4.20: Temperature of the Motor Windings at Loaded Operation

For different load torque values, the total efficiency of the motor drive is also calculated. This calculation is made by measuring the DC bus voltage and the output torque, as in Figure 4.21; and then calculated using the following equation given in (4.18).

$$\eta = \frac{P_{out}}{P_{in}} = \frac{\frac{\left(\sum_{i=1}^{n} T_{mech}(i)\frac{t}{n}\right)}{t}\omega_{mech}}{\frac{\left(\sum_{i=1}^{n} I_{bus}(i)\frac{t}{n}\right)}{t}V_{bus}} \tag{4.18}$$

The efficiency and the load torque relation is illustrated in Figure 4.22. On the figure, it is seen that the efficiency decreases for the load values larger than the half load. The main reason for that is the inverter losses dramatically increase for large load current values. Qualitatively speaking, the inverter heats up more than the motor windings for the same load torque, at the same time interval.

4.3.3 Transient Performance

To observe the transient performance of the machine and the response time of the current controllers, a speed-reversal test is applied to the motor. That is, the speed reference is suddenly changed from 100 rad/sec to -100 rad/sec to make sure that the machine operates in three different quadrants for a short amount of time.

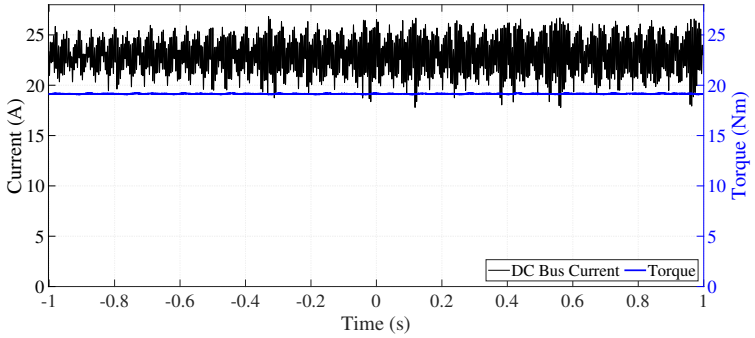

Figure 4.21: Bus Current and Torque of the Machine For Efficiency Calculation

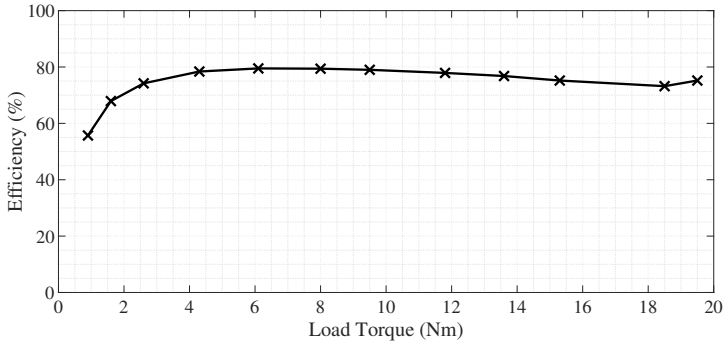

Figure 4.22: Changing Drive Efficiency w.r.t. the Load Torque

In Figure 4.23, the DQ currents, reference Q1 current, output torque and speed waveforms are shown for this test. Both in Figure 4.23a and 4.23b, the effect of sudden speed reference change on Q1 current is clearly shown. In Figure 4.23b it is also possible to observe that the response time of the current controllers are short and they are well-tuned, as the measured and the reference currents almost overlap.

For this speed-reversal test, the settling time of the motor speed is 6 seconds, as presented in Figure 4.23d. This value is almost five times the settling time in the simulation presented in Section 4.2.1. Though, this is not unexpected since the behavior of current and speed controllers and the actual value of the rotor inertia is different than they are in the drive simulation.

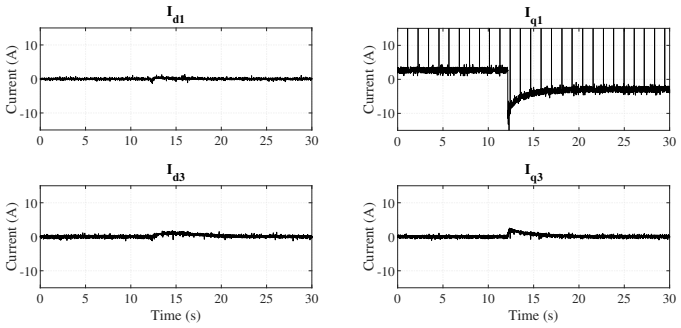

(a) DQ Currents

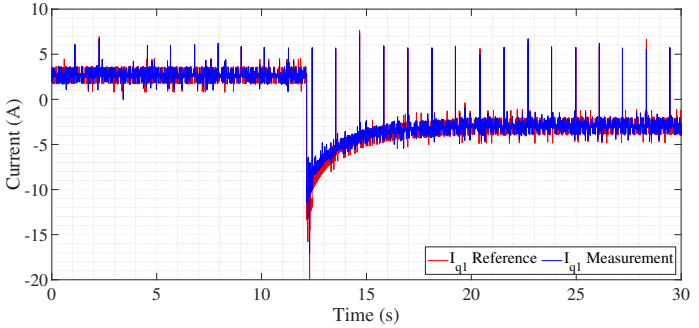

(b) Q1 Current: Reference and Measured

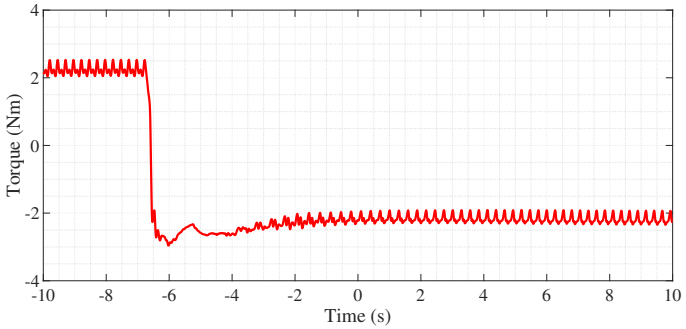

(c) Torque

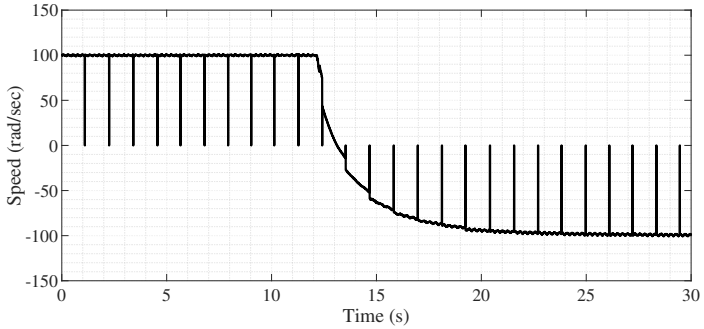

(d) Electrical Speed

Figure 4.23: Experimental Results: Motor Performance Parameters at Speed Reversal Operation

4.3.4 Third-Harmonic Current Injection

Thanks to the five-phase topology, the third harmonic current has torque production capability for this machine, unlike the three-phase conventional machines. For speed-controlled closed-loop operation, third harmonic current injection provides the production of the same torque (because of the constant load torque) to maintain the same speed with lower current amplitudes. Speed control structure of the control loop determines the required torque value to keep the speed at the level of the set point. Obviously, torque reference, which is the output of the speed controller determines the Q1 and Q3 reference current values. For a certain torque reference, Q3 current reference is set to a value proportional to Q1. Resultantly, the total torque production equals to load torque but the output torque is produced both by fundamental and third order currents. With a similar approach, it can be concluded that third-harmonic current injection enhances the produced torque for torque-controlled closed loop operation.

Similar to the simulated cases in Section 4.2.1, the operation of the drive in the experiments are in speed-controlled mode. Figure 4.24 shows the torque, electrical speed and DQ currents for the THI instant. Similar to the simulated cases, the speed of the machine does not change (see Figure 4.24c, where only a small deviation is present in the output torque due to the input disturbance. This deviation can be seen in Figure 4.24b, in both large time-scale and in panned-in scale, which is explanatory for the ratio of the torque deviation.

Besides, Figure 4.25 presents the phase currents before and after THI. Comparing both cases, we can clearly see that the amplitude of the phase currents decreases 16%, where the torque remains the same. Hence, we can conclude that the experimental results are also in good agreement with the drive simulation results for this case too.

4.3.5 Conclusion and Discussion

This section presented the experimental results for the operation of the five-phase drive under several operating conditions. No-load and loaded cases, transient, and THI operations were the main observation cases. Due to the limitations caused by

the fragility of the inverter, we were not able to cover the whole constant torque operation region. Nevertheless, the simulations have been repeated at the operating points where the experiments have been performed in order to observe the similarities and discrepancies between the prototype and the drive simulation model. In general, it can be concluded that the experimented cases were in agreement with the analytical calculations and simulation results.

For no-load case, it is observed that the peak of the phase currents is 2 A for both experiment and simulation, where the current ripple because of switching is higher in simulation results. For loaded cases, for the same load torque, the peak value of the phase current is approximately 7-8$\%$ higher in simulation than in experiment, which is also mainly caused by the current ripple caused by switching. Also, it is shown that the drive provides its maximum efficiency, which is 80$\%$ at 6-8 Nm load torque.

For the transient characteristics of the drive, the main discrepancy between the simulation and experimental results was the transient response time of the drive. The main reasons for this are the lack of feed-forward path in the experimental control loop, and the poor estimation of the motor inertia. Nevertheless, by referring to Figure 4.23b, it can be deduced that the tuning of the current controllers is sufficient, since the measurement and the reference Q1 currents are nearly equal. All in all, it can be concluded that the operation of the motor drive is compatible with the simulated model.

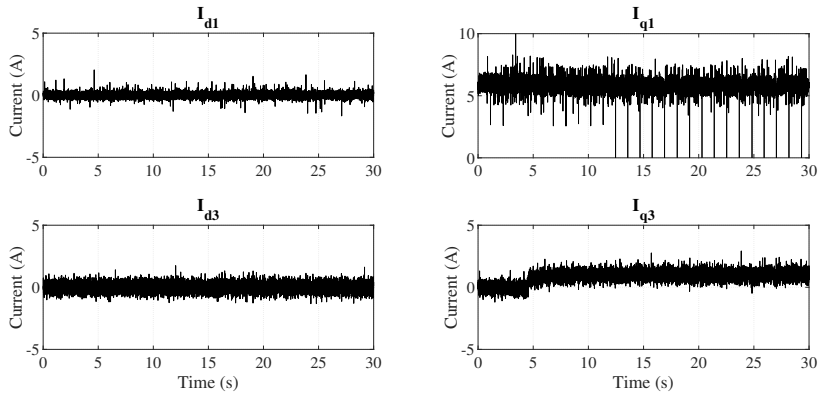

(a) DQ Currents

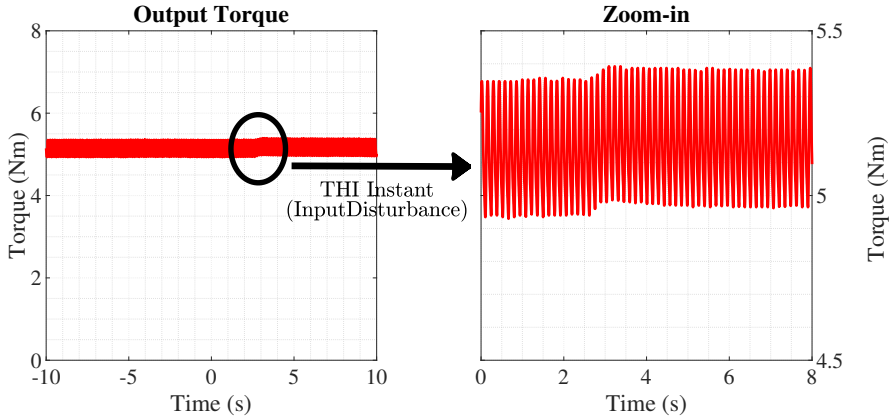

(b) Torque

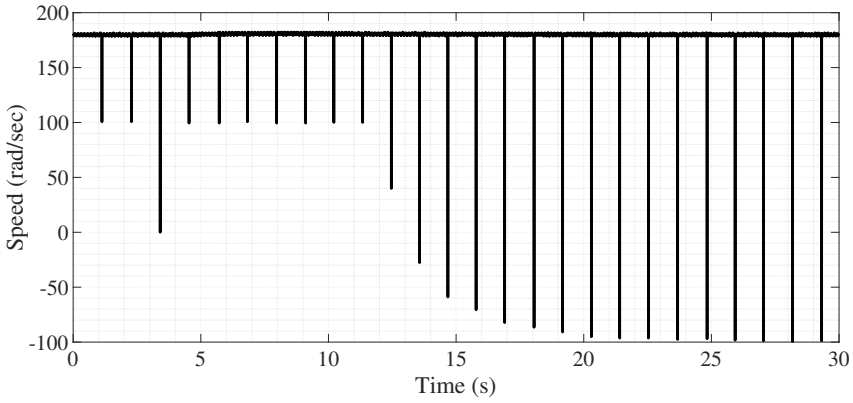

(c) Electrical Speed

Figure 4.24: Experimental Results: Motor Performance Parameters with Third Harmonic Current Injection

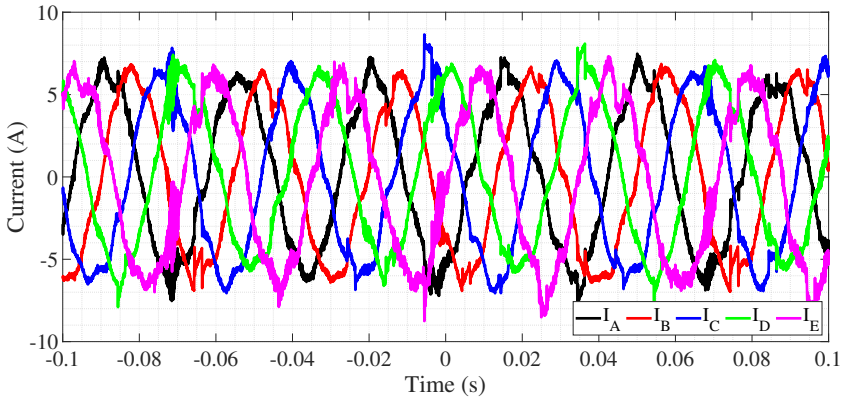

(a) Without THI

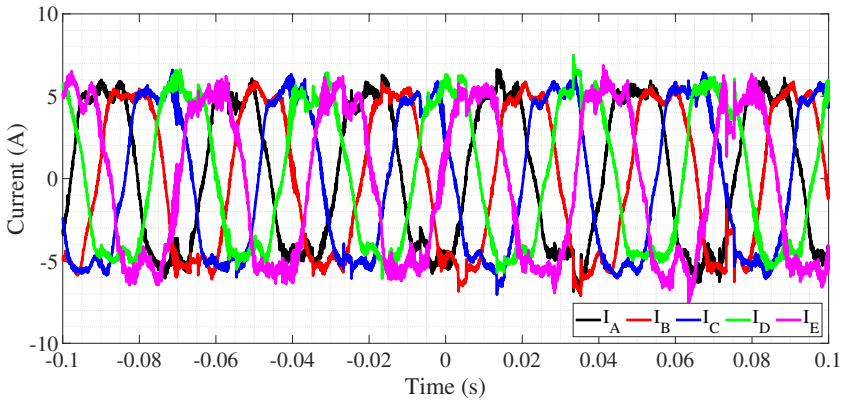

(b) With THI

Figure 4.25: Experimental Results: Phase Currents Before and After Third Harmonic Current Injection

CHAPTER 5

FAULT TOLERANT CONTROL OF FIVE PHASE MACHINE

This study mainly focuses on the occurrence and remedial strategies of a single-phase open circuit fault. First, main concept of fault tolerance, fault tolerant aspects of the proposed machine and drive topologies will be discussed. Following that, analytical calculation of open circuit fault currents will be examined under several operating conditions. This calculation is crucial for the study since it shows the safe operating limits of the drive system. Afterward, the calculation of new current references for post-fault operation will be shown. In this calculation, the currents of the remaining healthy phases are determined in order to form the pre-fault rotating MMF, for both first and third harmonic spaces. Finally, the modifications in the control loop for post-fault recovery operation will be described. As most preferred for PMSMs with non-sinusoidal back EMF waveforms, reduced order Clarke transformations for the first and the third harmonic currents and current references that eliminate torque pulsations have been adopted in the control strategy.

5.1 Concept of Fault Tolerance

Several aspects of the topology enable some significant assets by means of fault tolerance. The novel winding design with flat wires, which eliminates the short circuit fault risk, and multiphase design, which includes redundancy to the system, are two major assets of the proposed design.

Another aspect that implicates fault tolerance of a motor drive other than design decisions is the fault tolerant control procedure. This chapter mainly covers and examines the open circuit fault itself and the recovery methods for a machine with a

single-phase open circuit fault. The main idea behind the control procedure in a fault recovery operation is achieving the same output torque as in pre-fault operation, as closely as possible. This is performed by manipulating the current reference vectors that provide the pre-fault rotating MMF and eliminate even order pulsations in the output torque. Moreover, keeping the exceeded rated current limits at a minimum is one of the major concerns in post-fault operation.

5.2 Analytical Background of Open Circuit Fault

For system-level design and safety considerations, it is important to determine the amplitudes of phase currents under the occurrence of a single-phase open circuit fault. Current waveforms in an open circuit fault case can be obtained using both analytical calculations and numerical analysis (i.e., drive simulation with Simulink). In this section, the analytical approach will be examined.

Calculating the fault currents in our study is complicated because of several reasons. The PMSM drive operates closed-loop and has two control loops, consisting of two PI controllers. The outer loop controls the motor speed and determines the current references. In fault occurrence, as a result of oscillating output torque and deviating rotor speed, current references continuously change to keep the speed constant. Hence, estimating the continuously changing current waveforms requires heavy computation. Further simplifications on the drive topology and making several assumptions make the analytical modeling of fault currents possible:

- Open-loop operation is assumed.
- Input phase voltages remain the same for both healthy and faulty operating conditions.
- Continuing effect of torque and speed deviations are ignored. (Unbalanced phase currents would cause torque ripple. Torque ripple would cause continuous fluctuations of the speed, which would be the reason for changing induced EMF magnitudes and frequency.) Induced EMF voltages are also assumed to remain the same.

- Third harmonic injection to the phase current is not investigated. The input voltage to each phase is assumed to be supplied in a way that the third order back EMF voltage is canceled.

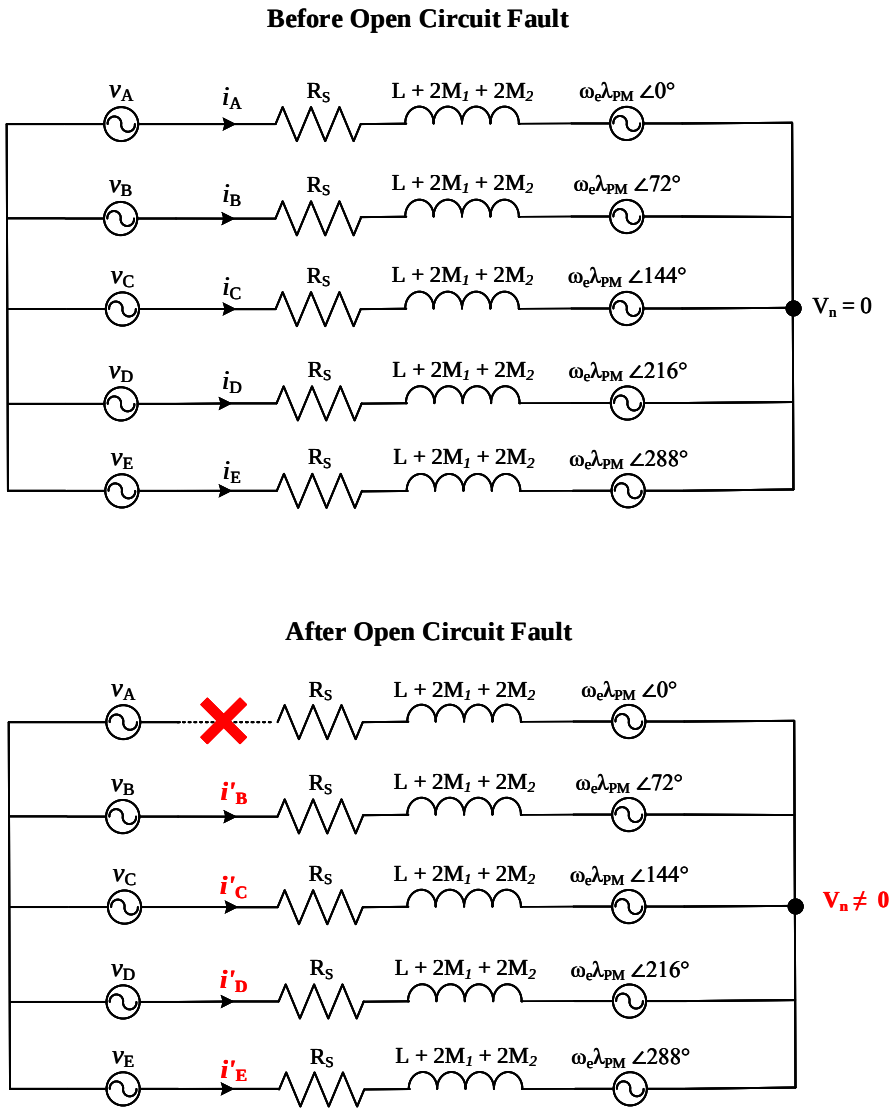

Figure 5.1: Equivalent Circuit of the Five-Phase Machine Before and After Open Circuit Fault Occurrence

Figure 5.1 shows the equivalent circuit of the five-phase machine before and after the machine is under open-circuit fault. The analytical computation of the fault currents is based on solving these two circuits. Considering the input phase voltages are equal

in both cases, a simple node analysis and equating the voltage drops on each phase of the machine before and after fault occurrence would give the fault currents.

The phase voltage equation of a surface mount PMSM is given in (5.1). Bold terms are 5×1 vectors and the others are 5×5 matrices.

$$\boldsymbol{V_s} = R_s \boldsymbol{I_s} + \frac{d}{dt}(\boldsymbol{\Lambda}_{ss} + \boldsymbol{\Lambda}_{PM}) = R_s \boldsymbol{I_s} + L_s \frac{d}{dt}\boldsymbol{I_s} + \frac{d}{dt}\boldsymbol{\Lambda}_{PM} \tag{5.1}$$

As a result of the aforementioned assumptions, during the healthy and faulty modes, it can be said that input voltage and back EMF remain unchanged. Therefore, fault currents can be calculated by equalizing the resistive and inductive voltage drop on the phase windings. As a reference, assuming that the neutral node voltage is 0 V in a healthy and balanced condition, there will be a non-zero voltage in the neutral node of a star-connected machine under fault. This relation is described in (5.2).

$$R_s \boldsymbol{I_{s1}} + L_s \frac{d}{dt}\boldsymbol{I_{s1}} + = R_s \boldsymbol{I_{s2}} + L_s \frac{d}{dt}\boldsymbol{I_{s2}} + \boldsymbol{V_n} \tag{5.2}$$

where

$$\begin{aligned} \boldsymbol{I_{s1}} &= \begin{bmatrix} i_A & i_B & i_C & i_D & i_E \end{bmatrix}^t \\ &= \begin{bmatrix} I_{peak}\, e^{j0} & I_{peak}\, e^{j\frac{2\pi}{5}} & I_{peak}\, e^{j\frac{4\pi}{5}} & I_{peak}\, e^{j\frac{6\pi}{5}} & I_{peak}\, e^{j\frac{8\pi}{5}} \end{bmatrix}^t \end{aligned} \tag{5.3}$$

$$\boldsymbol{I_{s2}} = \begin{bmatrix} i'_B & i'_C & i'_D & i'_E \end{bmatrix}^t \tag{5.4}$$

The equation can be written in the phasor domain by replacing the derivative operators with $j\omega$. Also, the sum of resistive and inductive elements can be represented as a single impedance matrix, as in (5.5b).

In this analysis, open-circuited phase is assumed to be Phase A. Therefore, the fifth row of the matrices is eliminated for the upcoming operations. For the benefit of solution of these operations, two sub-matrices, as $\mathbb{Z}_1$ and $\mathbb{Z}_1$, can be obtained from

$\mathbb{Z}$, which are given in (5.5c) and (5.5d), respectively.

$$\mathbb{Z} = \left[\begin{array}{c|cccc} R_s + j\omega L & j\omega M_1 & j\omega M_2 & j\omega M_2 & j\omega M_1 \\ \hline j\omega M_1 & R_s + j\omega L & j\omega M_1 & j\omega M_2 & j\omega M_2 \\ j\omega M_2 & j\omega M_1 & R_s + j\omega L & j\omega M_1 & j\omega M_2 \\ j\omega M_2 & j\omega M_2 & j\omega M_1 & R_s + j\omega L & j\omega M_1 \\ j\omega M_1 & j\omega M_2 & j\omega M_2 & j\omega M_1 & R_s + j\omega L \end{array}\right] \tag{5.5a}$$

$$= \left[\begin{array}{c|c} R_s + j\omega L & \mathbb{Z}_2^t \\ \hline \mathbb{Z}_2 & \mathbb{Z}_1 \end{array}\right] \tag{5.5b}$$

$$\mathbb{Z}_1 = \left[\begin{array}{cccc} R_s + j\omega L & j\omega M_1 & j\omega M_2 & j\omega M_2 \\ j\omega M_1 & R_s + j\omega L & j\omega M_1 & j\omega M_2 \\ j\omega M_2 & j\omega M_1 & R_s + j\omega L & j\omega M_1 \\ j\omega M_2 & j\omega M_2 & j\omega M_1 & R_s + j\omega L \end{array}\right] \tag{5.5c}$$

$$\mathbb{Z}_2 = \left[\begin{array}{c} j\omega M_1 \\ j\omega M_2 \\ j\omega M_2 \\ j\omega M_1 \end{array}\right] \tag{5.5d}$$

With all these manipulations, the equation (5.2) can be reduced to (5.6).

$$\mathbb{Z}_1 \underbrace{\left[\begin{array}{c} e^{j\frac{2\pi}{5}} \\ e^{j\frac{4\pi}{5}} \\ e^{j\frac{6\pi}{5}} \\ e^{j\frac{8\pi}{5}} \end{array}\right]}_{\mathbf{E}} + \mathbb{Z}_2 e^{j0} = \mathbb{Z}_1 \underbrace{\left[\begin{array}{c} i'_B \\ i'_C \\ i'_D \\ i'_E \end{array}\right]}_{\mathbf{I}_f} + \underbrace{\left[\begin{array}{c} v_n \\ v_n \\ v_n \\ v_n \end{array}\right]}_{\mathbf{V}_n} \tag{5.6}$$

There are 5 unknowns in (5.6) which are v_n and $\mathbf{I}_f$. Considering Kirchhoff's current

law, a fifth equation ((5.7)) can be obtained and this system of linear equations can be solved. The equation can be modified as in (5.8).

$$i'_B + i'_C + i'_D + i'_E = 0 \tag{5.7}$$

$$\mathbf{I}_f = I_{peak}\,\mathbf{E} + \mathbb{Z}_1^{-1}(I_{peak}\,\mathbb{Z}_2\,e^{j0} - \mathbf{V}_n)) \tag{5.8}$$

Solving for (5.7) and (5.8), fault currents in phasor domain can be obtained. Keeping in mind the assumptions made for this calculation, this solution is valid when the third harmonic injection is not present and there is no disturbance in torque and speed.

Assuming a test case where the motor is loaded with half of the rated output torque (13 Nm) and rated speed (525 rpm, 35 Hz electrical), corresponding peak induced EMF value becomes 20 V. Under the assumption of rotor flux oriented control, i_q can be taken as 13 A. Using these operating point parameters, phase currents under single-phase open circuit fault condition can be obtained as in Figure 5.2b, where they were as in Figure 5.2a in normal operation. In Figure 5.2b, it is observed that two adjacent phases (in both forward and reverse direction) to the phase that fault occurs carry larger current than the others.

The study conducted by Guzman in [55] on induction machines clearly explains the effect of an open circuit fault on the phase variable model. In this fault condition, the spatial asymmetry occurs for the remaining phases and causes the machine parameters to be time-dependent. As a result of this incident, the electrical parameters, such as phase current, forms an ellipsoid in $\alpha\beta$ plane. This phenomenon is verified by showing the obtained phase currents (in Figure 5.2) in $\alpha\beta$ plane, as presented in Figure 5.3.

The change in phase currents also directly affects the rotating MMF in the airgap. The MMF due to each phase current can be defined as in (5.9). The sum of these five MMFs equals a rotating MMF given in (5.10).

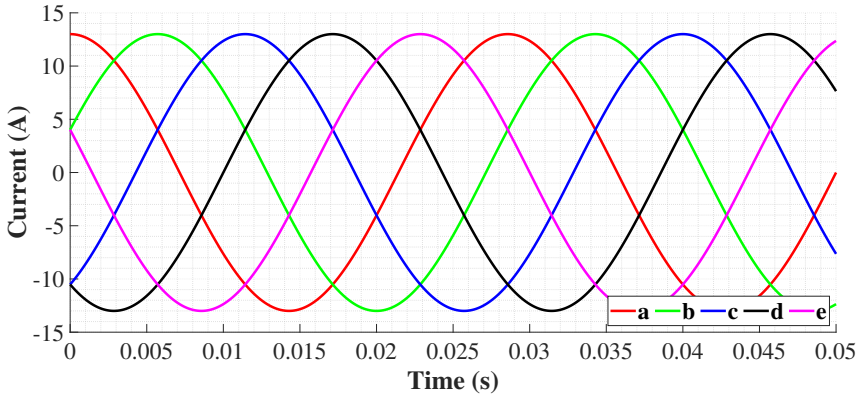

(a) Normal Operation

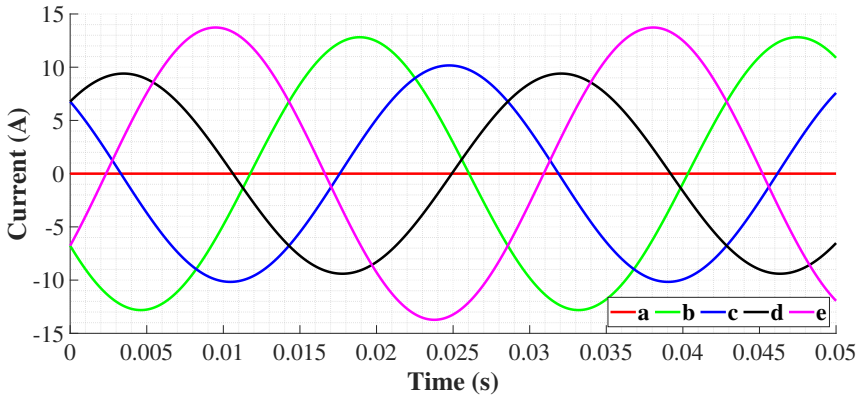

(b) Open Circuit Fault Operation

Figure 5.2: Analytical Phase Currents: Normal Operation and the Operation Under an Open Circuit Fault, at Half Load and Rated Speed

$$
\begin{aligned}
\mathcal{F}_A(\theta,t) &= NI_1\cos(\omega t)\cos(\theta)\\
\mathcal{F}_B(\theta,t) &= NI_1\cos\left(\omega t-\frac{2\pi}{5}\right)\cos\left(\theta-\frac{2\pi}{5}\right)\\
\mathcal{F}_C(\theta,t) &= NI_1\cos\left(\omega t-\frac{4\pi}{5}\right)\cos\left(\theta-\frac{4\pi}{5}\right)\\
\mathcal{F}_D(\theta,t) &= NI_1\cos\left(\omega t-\frac{6\pi}{5}\right)\cos\left(\theta-\frac{6\pi}{5}\right)\\
\mathcal{F}_E(\theta,t) &= NI_1\cos\left(\omega t-\frac{8\pi}{5}\right)\cos\left(\theta-\frac{8\pi}{5}\right)
\end{aligned}
\tag{5.9}
$$

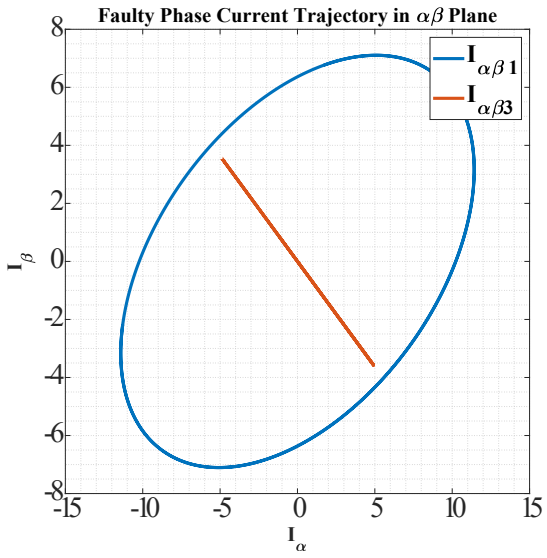

Figure 5.3: Phase Currents in $\alpha\beta$ Plane, Under Single-Phase Open Circuit Fault, at Half Load and Rated Speed

$$\mathcal{F}(\theta, t) = \frac{5}{2} N I_1 \cos(\theta - \omega t) \tag{5.10}$$

In Figure 5.4, airgap MMF waveforms are shown in a 3D space as a function of both space and time. Figure 5.4a shows the MMF distribution in normal operation, which is seen to be perfect sinusoidal in the time domain and which has a constant magnitude with respect to the spatial angle. However, in Figure 5.4b, which presents the MMF distribution for a single-phase open circuit fault (1-Ph OCF) operation, the invariability of the magnitude with respect to spatial angle disappears.

This fact is also further illustrated in Figure 5.5, which shows the MMF trajectories as a function of spatial angle. Unlike the circular form in Figure 5.5a, the trajectory becomes distorted in the faulted case, given in Figure 5.5b. Here, the term non-circular MMF means that the peak value of the MMF changes as a function of rotor angle. Such an unwanted effect is especially crucial for torque production as the torque of the machine is the derivative of magnetic co-energy with respect to the rotor angle, where magnetic co-energy is directly related to the MMF. The derivative of angle-dependent MMF function will result in angle-dependent magnitude terms which will cause even order harmonics and pulsations in the output torque, and must

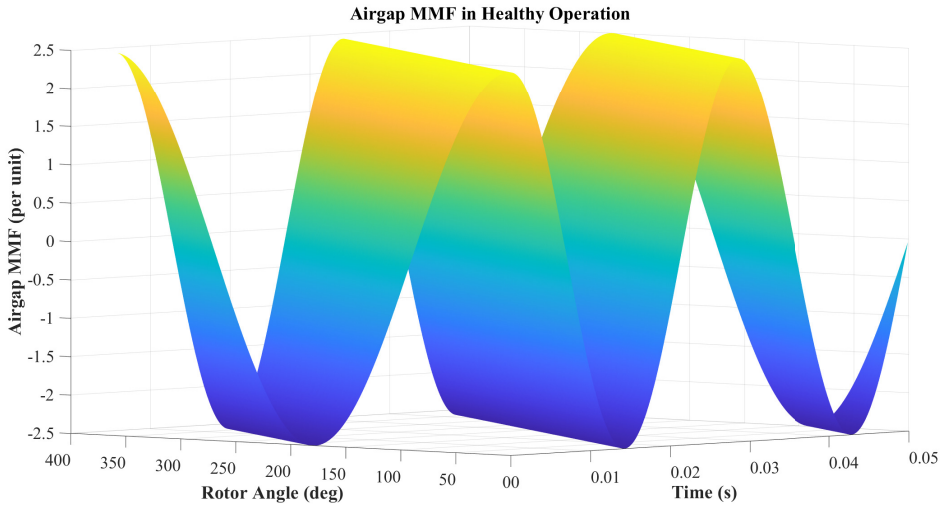

(a) Normal Operation

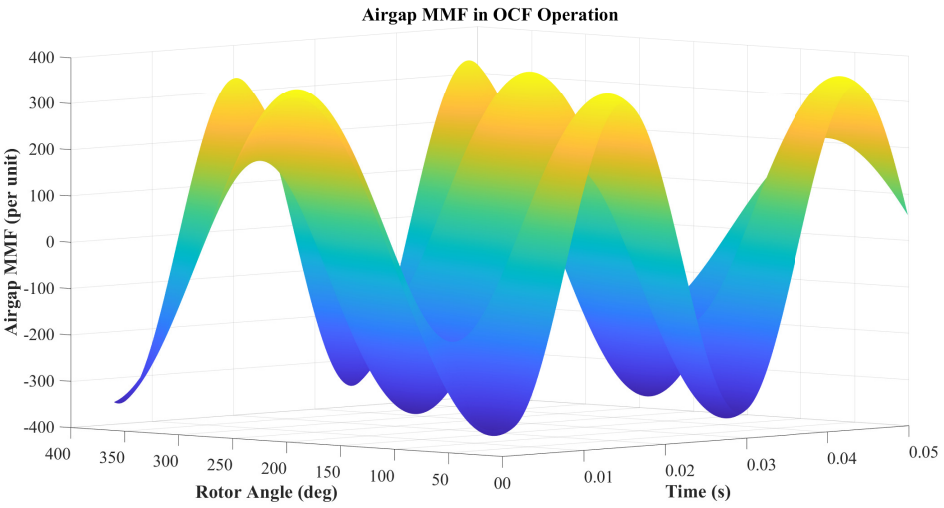

(b) 1-Ph OCF Operation

Figure 5.4: Airgap MMF in 3D Space, as a Function of Time and Spatial Angle, For Normal and 1-Ph OCF Operations

be eliminated.

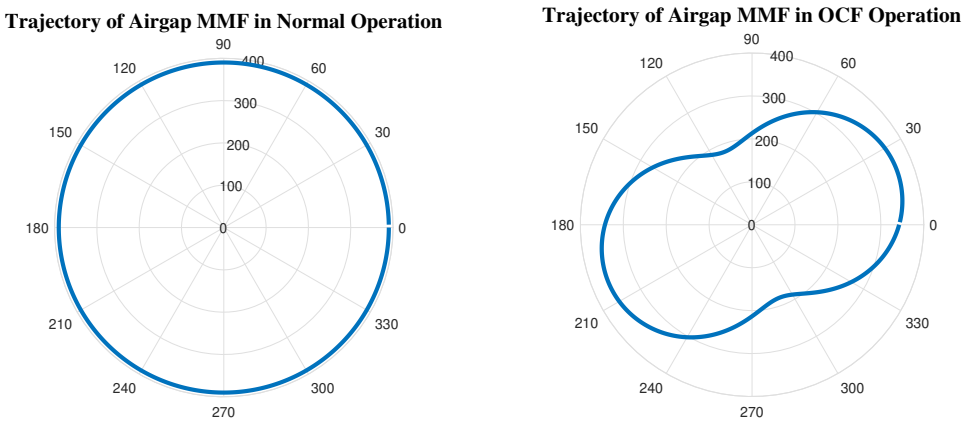

(a) Normal Operation

(b) 1-Ph OCF Operation

Figure 5.5: Airgap MMF Trajectories as a Function of Spatial Angle, For Normal and 1-Ph OCF Operations

5.3 Open Circuit Fault Recovery Strategies

Having identified and discussed the machine operation under a 1-Ph OCF condition, the recovery strategies with their assets and drawbacks on the operation should be examined. As mentioned several times previously, a motor drive that is claimed to be fault tolerant should maintain the operation in a fault occurrence with the lowest possible deviation from the desired operation point, with minimum derating or overrating. To achieve this, the most common approach is rearranging the phase currents in order to obtain a circular MMF trajectory, as given in Figure 5.5a [56]. Moreover, additional constraints are also introduced on top of MMF recovery. Minimum derating of phase variables, minimization of torque pulsations, and minimization of Joule losses are some of the major concerns of building the recovery strategies [57].

In this study the main aspect of the fault tolerant control is to maintain the machine performance. That is, the major concern is to minimize the torque ripple and exceed the rated current value, at a minimum level, to obtain the same output torque. To achieve this the primary step is to determine remedial current references in order to obtain a rotating MMF with circular trajectory, which should eliminate the torque ripple when the system is considered to be consist of the parameters at a single-frequency. For the consideration of higher-order terms, several ripple eliminating

methods will be introduced such as third harmonic injection and redefinition of the remedial phase current references.

5.3.1 Determination of the Remedial Phase Currents

In normal operation, without third harmonic current injection, the MMFs due to each phase of the machine is defined as in (5.9). These sum up to a rotating MMF given in (5.11). Omitting the $e^{j\omega t}$ term, it can also be obtained in the phasor domain.

$$\begin{aligned} \mathcal{F}_i(\theta, t) &= \frac{5}{2} N I_1 \cos(\theta - \omega t) \\ &= \frac{5NI_1}{2} e^{j\omega t} e^{j\theta} \end{aligned} \tag{5.11}$$

In an open circuit fault, assuming phase A, to preserve the rotating MMF, the remedial current phasors, which are shown with the primed variables, should be defined according to the following constraints:

$$\begin{aligned} \frac{5I_1}{2} e^{j\theta} &= i'_B\, e^{j\frac{2\pi}{5}} + i'_C\, e^{j\frac{4\pi}{5}} + i'_D\, e^{j\frac{6\pi}{5}} + i'_E\, e^{j\frac{8\pi}{5}} \\ \frac{5NI_1}{2} \cos(\theta) &= N(i'_B + i'_E) \cos\left(\frac{2\pi}{5}\right) - N(i'_C + i'_D) \cos\left(\frac{\pi}{5}\right) \\ \frac{5NI_1}{2} \sin(\theta) &= N(i'_B - i'_E) \sin\left(\frac{2\pi}{5}\right) + N(i'_C - i'_D) \sin\left(\frac{\pi}{5}\right) \end{aligned} \tag{5.12}$$

The aims were to preserve the pre-fault average output torque and to adopt the equal Joule losses criterion. Besides, the remaining phases have a symmetrical spatial distribution within the stator. Consequently, the phase current phasors in the recovery operation must meet the condition given in (5.13). [58, 59]

$$\begin{aligned} i'_B &= -i'_D \\ i'_C &= -i'_E \end{aligned} \tag{5.13}$$

Solving for (5.12) and (5.13), phase currents for 1-Ph OCF recovery operation can be obtained, as given in (5.14) and (5.15).

$$\begin{aligned} i'_B &= -i'_D = \frac{5I_1}{4}\left(\frac{\cos\left(\theta - \frac{\pi}{5}\right)}{\sin\left(\frac{2\pi}{5}\right)^2}\right) \\ i'_C &= -i'_E = \frac{5I_1}{4}\left(\frac{\cos\left(\theta - \frac{4\pi}{5}\right)}{\sin\left(\frac{2\pi}{5}\right)^2}\right) \end{aligned} \tag{5.14}$$

$$\begin{aligned} i'_B &= 1.382\, I_1 \cos\left(\omega t - \frac{\pi}{5}\right) \\ i'_C &= 1.382\, I_1 \cos\left(\omega t - \frac{4\pi}{5}\right) \\ i'_D &= 1.382\, I_1 \cos\left(\omega t - \frac{6\pi}{5}\right) \\ i'_E &= 1.382\, I_1 \cos\left(\omega t - \frac{9\pi}{5}\right) \end{aligned} \tag{5.15}$$

Unfortunately, determining the phase currents by considering only the recovery of non-circular MMF trajectory is not enough for this study. This solution should be valid only if the machine under consideration had sinusoidal back EMF. As this machine has a trapezoidal back EMF waveform, consisting of higher order harmonics but mainly first and third order voltages, the asymmetry in the third space of flux linkage interacts with the fundamental space, which causes large pulsations in the output torque, at even ordered frequencies [60, 61].

In Figure 5.6, the output torque for an open loop simulation of the machine, operating at half load is present. Even if the remedial current references have been applied to the remaining healthy phases after 1-Ph OCF occurs, it can be observed that torque ripple is almost 22%, which is quite significant.

Therefore, with a similar approach to the previously described one, third harmonic current must be injected into the phase windings. The criteria can be obtained by simply multiplying the angles of the previous ones by 3.

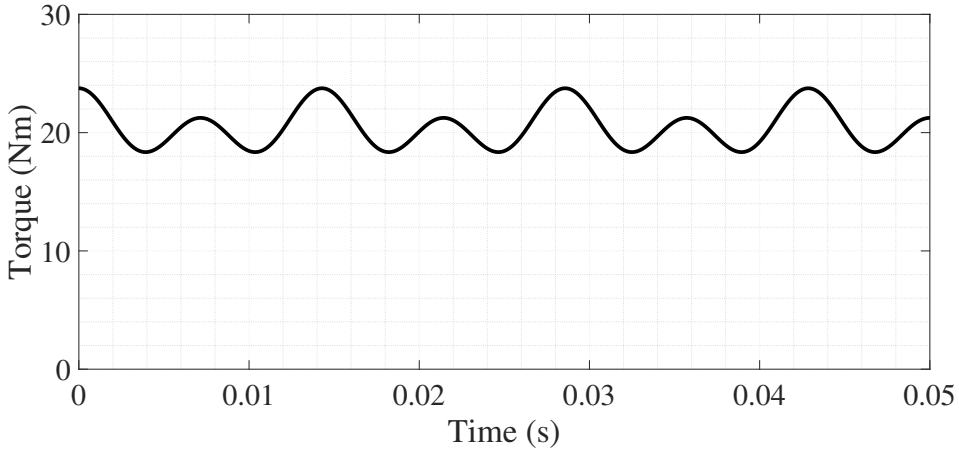

Figure 5.6: Output Torque for 1-Ph OCF Recovery Operation, Without Third Harmonic Current Injection

$$\frac{5I_3}{2}e^{j\theta} = i'_{B3}\,e^{j\frac{6\pi}{5}} + i'_{C3}\,e^{j\frac{2\pi}{5}} + i'_{D3}\,e^{j\frac{8\pi}{5}} + i'_{E3}\,e^{j\frac{4\pi}{5}} \tag{5.16}$$

$$\begin{aligned} i'_{B3} &= -i'_{D3} = \frac{5I_3}{4}\left(\frac{\cos\left(3\theta - \frac{3\pi}{5}\right)}{\sin\left(\frac{\pi}{5}\right)\sin\left(\frac{4\pi}{5}\right)}\right) \\ i'_{C3} &= -i'_{E3} = \frac{5I_3}{4}\left(\frac{\cos\left(3\theta - \frac{2\pi}{5}\right)}{\sin\left(\frac{\pi}{5}\right)\sin\left(\frac{4\pi}{5}\right)}\right) \end{aligned} \tag{5.17}$$

$$\begin{aligned} i'_B &= 1.382\,I_1\cos\left(\omega t - \frac{\pi}{5}\right) + 3.618\,I_3\cos\left(3\omega t - \frac{3\pi}{5}\right) \\ i'_C &= 1.382\,I_1\cos\left(\omega t - \frac{4\pi}{5}\right) + 3.618\,I_3\cos\left(3\omega t - \frac{2\pi}{5}\right) \\ i'_D &= 1.382\,I_1\cos\left(\omega t - \frac{6\pi}{5}\right) + 3.618\,I_3\cos\left(3\omega t - \frac{8\pi}{5}\right) \\ i'_E &= 1.382\,I_1\cos\left(\omega t - \frac{9\pi}{5}\right) + 3.618\,I_3\cos\left(3\omega t - \frac{7\pi}{5}\right) \end{aligned} \tag{5.18}$$

5.3.2 Modification of the Control Loop

In post-fault operation, the basic control loop structure does not change; however, some modifications are inevitable. Recent studies in this field suggest that under a

1-Ph OCF, reference current values and controller must be revised. With the main claim of difficulty of tracking varying i_d and i_q current references, some of the researchers adapted some more sophisticated controller types, such as proportional integral resonant controller [62], model predictive control (MPC) [55], robust control and hysteresis control [63]. It is also worth mentioning that it is still possible to use the conventional PI controller even for the machines with large phase inductance and with deviating current references [58]. In our study, the use of PI control technique will remain for the sake of simplicity and to keep the modification of the structure at the least level.

Yet, as the previous section suggests, the current references and their application method should be modified for post-fault operation. There are two main techniques to achieve this:

- New current references can be calculated in compliance with the Clarke transformations used in the normal operation [64].
- New reduced-order Clarke transformation matrices should be defined [58, 60].

As the first option complicates eliminating the co-dependence of the fundamental and third harmonic spaces [65], reduced order transformation matrices will be employed.

As defined explicitly in Chapter 3, inverse Clarke transform equation can be shown as in (5.19).

$$\begin{bmatrix} i_A \\ i_B \\ i_C \\ i_D \\ i_E \end{bmatrix} = \begin{bmatrix} \cos(0) & \sin(0) & \cos(0) & \sin(0) & \frac{1}{\sqrt{2}} \\ \cos\left(\frac{2\pi}{5}\right) & \sin\left(\frac{2\pi}{5}\right) & \cos\left(\frac{6\pi}{5}\right) & \sin\left(\frac{6\pi}{5}\right) & \frac{1}{\sqrt{2}} \\ \cos\left(\frac{4\pi}{5}\right) & \sin\left(\frac{4\pi}{5}\right) & \cos\left(\frac{2\pi}{5}\right) & \sin\left(\frac{2\pi}{5}\right) & \frac{1}{\sqrt{2}} \\ \cos\left(\frac{6\pi}{5}\right) & \sin\left(\frac{6\pi}{5}\right) & \cos\left(\frac{8\pi}{5}\right) & \sin\left(\frac{8\pi}{5}\right) & \frac{1}{\sqrt{2}} \\ \cos\left(\frac{8\pi}{5}\right) & \sin\left(\frac{8\pi}{5}\right) & \cos\left(\frac{4\pi}{5}\right) & \sin\left(\frac{4\pi}{5}\right) & \frac{1}{\sqrt{2}} \end{bmatrix} \begin{bmatrix} i_{\alpha 1} \\ i_{\beta 1} \\ i_{\alpha 3} \\ i_{\beta 3} \\ i_0 \end{bmatrix} \tag{5.19}$$

Assuming that 1-Ph OCF occurs in phase A and the phase windings are connected in star connection (i.e. $i_0 = 0$), resultant i_A will become 0. Therefore, we can obtain the following equality.

$$i_{\alpha 1} = -i_{\alpha 3} \tag{5.20}$$

(5.20) implies that the first and third spaces are not independent anymore. Therefore, to modify the T_c, a new vector orthogonal to both $i_{\alpha 1}$ and $i_{\beta 1}$ row transform vectors should be defined. This vector can also be called third space current [60, 66], and it eliminates the effect of third harmonic current from the first plane. This vector is defined as in (5.21), to make sure that it is linearly independent with other row vectors and ensures the condition in (5.18). In [58], this vector is multiplied with a factor of $\sin\left(\frac{2\pi}{5}\right)$ without a justification, but (5.21) is more suitable for the sake of clarity.

$$i_{z1} = i_{z3} = \begin{bmatrix} 1 & -1 & 1 & -1 \end{bmatrix}^t \tag{5.21}$$

Similar approach can also be followed for the third space Clarke transformation. Resultant current vectors after stationary transformations for both first and third spaces become:

$$\begin{aligned} i_{\alpha\beta 1} &= \begin{bmatrix} i_{\alpha 1} & i_{\beta 1} & i_{z1} & i_{01} \end{bmatrix}^t \\ i_{\alpha\beta 3} &= \begin{bmatrix} i_{\alpha 3} & i_{\beta 3} & i_{z3} & i_{03} \end{bmatrix}^t \end{aligned} \tag{5.22}$$

Adopting the new current references calculated in (5.18), new inverse Clarke transformations for fault tolerant control are obtained as in (5.23) and (5.24).

$$T^{-1}_{C1_{FTC}} = 1.382 \begin{bmatrix} \cos\left(\frac{\pi}{5}\right) & \sin\left(\frac{\pi}{5}\right) & 0.181 & 0.181 \\ \cos\left(\frac{4\pi}{5}\right) & \sin\left(\frac{4\pi}{5}\right) & -0.181 & 0.181 \\ \cos\left(\frac{6\pi}{5}\right) & \sin\left(\frac{6\pi}{5}\right) & 0.181 & 0.181 \\ \cos\left(\frac{9\pi}{5}\right) & \sin\left(\frac{9\pi}{5}\right) & -0.181 & 0.181 \end{bmatrix} \tag{5.23}$$

$$T^{-1}_{C3_{FTC}} = 3.618 \begin{bmatrix} \cos\left(\frac{3\pi}{5}\right) & \sin\left(\frac{3\pi}{5}\right) & 0.069 & 0.069 \\ \cos\left(\frac{2\pi}{5}\right) & \sin\left(\frac{2\pi}{5}\right) & -0.069 & 0.069 \\ \cos\left(\frac{8\pi}{5}\right) & \sin\left(\frac{8\pi}{5}\right) & 0.069 & 0.069 \\ \cos\left(\frac{7\pi}{5}\right) & \sin\left(\frac{7\pi}{5}\right) & -0.069 & 0.069 \end{bmatrix} \tag{5.24}$$

Due to spatial asymmetry, these vectors form ellipsoids in $\alpha\beta$ plane (i.e., the norms of the vectors are not equal). Because of this reason, each row vector must have a

coefficient normalizing the vector for the Clarke transformation matrices. These coefficients can be obtained by solving the linear system consisting of α and β currents.

$$1.382 \underbrace{\begin{bmatrix} \cos\left(\frac{\pi}{5}\right) & \sin\left(\frac{\pi}{5}\right) \\ \cos\left(\frac{4\pi}{5}\right) & \sin\left(\frac{4\pi}{5}\right) \\ \cos\left(\frac{6\pi}{5}\right) & \sin\left(\frac{6\pi}{5}\right) \\ \cos\left(\frac{9\pi}{5}\right) & \sin\left(\frac{9\pi}{5}\right) \end{bmatrix}}_{A} \underbrace{\begin{bmatrix} i_{\alpha 1} \\ i_{\beta 1} \end{bmatrix}}_{x} = \underbrace{\begin{bmatrix} i'_B \\ i'_C \\ i'_D \\ i'_E \end{bmatrix}}_{b}$$

$$x = \underbrace{\left(A^t\, A\right)^{-1}}_{\begin{bmatrix} \frac{1}{5} & 0 \\ 0 & \frac{1}{2.64} \end{bmatrix}} A^t\, b \tag{5.25}$$

As a result of (5.23) and (5.25), the new Clarke transformation can be calculated as in (5.26). With a similar approach, Clarke transformation for third harmonic space can also be found, as in (5.27). Park transformation for post-fault operation remains in its original form, and used as two separate matrices for two different rotation frequencies.

$$T_{C1_{FTC}} = \begin{bmatrix} \frac{\cos\left(\frac{\pi}{5}\right)}{3.618} & \frac{\cos\left(\frac{4\pi}{5}\right)}{3.618} & \frac{\cos\left(\frac{6\pi}{5}\right)}{3.618} & \frac{\cos\left(\frac{9\pi}{5}\right)}{3.618} \\ \frac{\sin\left(\frac{\pi}{5}\right)}{1.91} & \frac{\sin\left(\frac{4\pi}{5}\right)}{1.91} & \frac{\sin\left(\frac{6\pi}{5}\right)}{1.91} & \frac{\sin\left(\frac{9\pi}{5}\right)}{1.91} \\ \frac{\sin\left(\frac{2\pi}{5}\right)}{5} & \frac{-\sin\left(\frac{2\pi}{5}\right)}{5} & \frac{\sin\left(\frac{2\pi}{5}\right)}{5} & \frac{-\sin\left(\frac{2\pi}{5}\right)}{5} \\ 1 & 1 & 1 & 1 \end{bmatrix} \tag{5.26}$$

$$T_{C3_{FTC}} = \begin{bmatrix} \frac{\cos\left(\frac{3\pi}{5}\right)}{1.382} & \frac{\cos\left(\frac{2\pi}{5}\right)}{1.382} & \frac{\cos\left(\frac{8\pi}{5}\right)}{1.382} & \frac{\cos\left(\frac{7\pi}{5}\right)}{1.382} \\ \frac{\sin\left(\frac{3\pi}{5}\right)}{13.09} & \frac{\sin\left(\frac{2\pi}{5}\right)}{13.09} & \frac{\sin\left(\frac{8\pi}{5}\right)}{13.09} & \frac{\sin\left(\frac{7\pi}{5}\right)}{13.09} \\ \frac{\sin\left(\frac{2\pi}{5}\right)}{13.09} & \frac{-\sin\left(\frac{2\pi}{5}\right)}{13.09} & \frac{\sin\left(\frac{2\pi}{5}\right)}{13.09} & \frac{-\sin\left(\frac{2\pi}{5}\right)}{13.09} \\ 1 & 1 & 1 & 1 \end{bmatrix} \tag{5.27}$$

Redefinition of transformation matrices provides handling of the current reference values and the generation of SPWM reference sinusoidal waveforms. Yet, another

crucial point for smooth output torque in post-fault operation is the determination of the current references in the DQ frame. As the spatial asymmetry of the remaining phases causes an interaction between first and third order flux linkages and currents will cause fluctuation of the output torque, as previously discussed. Thus, reference currents must be selected in order to cancel those fluctuations.

The torque of an electric machine can be calculated by taking the derivative of magnetic co-energy of the system with respect to θ, electrical angle of the rotor given in (5.28), as also defined in Chapter 3.

$$\begin{aligned} T_e &= T_{e1} + T_{e3} \\ &= \frac{\partial W'}{\partial \theta} = P\left(\cancelto{0}{\frac{1}{2}\mathbf{I_s}^t \frac{\partial \mathbf{L_s}}{\partial \theta}\mathbf{I_s}} + \mathbf{I_s}^t \frac{\partial \mathbf{\Lambda_s}}{\partial \theta}\right) \end{aligned} \tag{5.28}$$

The torque consists of the products of both first and third order components. Besides, having adopted the air-cored stator topology, magnetic insaliency brings out the invariant inductance matrix with respect to rotor position. As a result, the torque produced in this machine is only synchronous torque. Reluctance torque is not produced (and the related term in (5.28) is canceled out) due to the magnetic insaliency.

Writing (5.28) more explicitly, (5.29) is obtained. As mentioned above, it may be observed that angle dependent terms in the torque equation. It is possible to eliminate some of these terms, as i_{d1}, i_{d3}, i_{z1} and i_{z3} references are set to 0.

$$\begin{aligned} T_e = \frac{5}{2}P\Bigg\{ & i_{d1}\left[i_{q1}(L_d - L_q) + \lambda_{m3}\cancelto{0}{\frac{3(\sin 2\theta + \sin 4\theta)}{2}}\right] \\ & + i_{q1}\left[\lambda_{m1} + \lambda_{m3}\frac{3(\cos 4\theta - \cos 2\theta)}{2}\right] \\ & + i_{d3}\lambda_{m1}\cancelto{0}{\frac{(\sin 4\theta - \sin 2\theta)}{2}} + i_{q3}\left[\lambda_{m3} + \lambda_{m1}\frac{(\cos 4\theta - \cos 2\theta)}{2}\right] \\ & + \cancelto{0}{3i_{z1}\lambda_{m3}\cos 3\theta} + \cancelto{0}{i_{z3}\lambda_{m1}\cos\theta}\Bigg\} \\ = i_{q1}\lambda_{m1} + i_{q3}\lambda_{m3} & + (3i_{q1}\lambda_{m3} + i_{q3}\lambda_{m1})\left(\frac{(\cos 4\theta - \cos 2\theta)}{2}\right) \end{aligned} \tag{5.29}$$

In order to obtain a smooth output torque, the remaining angle dependent term of the torque can be excluded by choosing the i_{q1} and i_{q3} references satisfying the following condition:

$$i_{q3} = \frac{-3\lambda_{m3}}{\lambda_{m1}} i_{q1} \tag{5.30}$$

With all these modifications, the same control approach enables post-fault recovery operation with minimum deration and smooth output torque.

5.4 An Alternative Approach

For an asymmetric system like in this study, third harmonic current injection may increase the computational burden of the main control loop, since the number of Clarke transform operation triples and complicates the structure of the control loop. Besides, the DQ current set points become varying signals instead of constant ones when fundamental and third order current references are combined. Conventional and moderate PI controllers may not be sufficient to track varying current references.

In order to overcome this issue, an alternative method is proposed in this study. This new method determines the current references by analytically computing the optimum phase angles of the remedial phase currents, in a way that the average torque is maximized, torque ripple is minimized, and the magnitudes of phase currents are equal with minimum overrating.

In contrast with the previously explained methodologies, this method does not guarantee a purely circular MMF trajectory and does not fully eliminate the torque ripple; but finds an optimum point between these two conditions. By exciting the machine with only the phase currents at fundamental frequency and with a minimized modification of the control loop (with low computation cost), fault tolerant control is expected to achieve.

5.4.1 Formulation of the Methodology

Formulation of the problem is quite simple. It is based on obtaining a torque equation with phase induced EMFs and phase currents, as a function of reference current phase

angle. For this method and to get a reference point, some basic preliminary conditions on remedial phase currents are defined. Figure 5.7 shows the remedial phase current phasor diagram in case where a 1-Ph OCF occurs in phase A.

- $I'_B = I'_D$
- $I'_C = I'_E$
- I'_B and I'_E (neighboring phases to the open-circuited phase) are symmetrical w.r.t. the α axis (assuming that 1-Ph OCF occurs on this axis).
- $\|I'_B\| = \|I'_C\| = \|I'_D\| = \|I'_E\|$

The reason for defining these preliminary conditions is to eliminate the necessity of a correction factor as in [66] while defining a Clarke transform matrix and to make sure that the phase current magnitudes are equal.

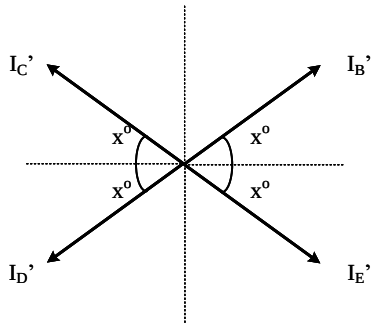

Figure 5.7: Current Phase Angle (x) Convention for Phase Currents

Having defined the reference current phase angle x, the torque equation is obtained as a function of x as in (5.33), using the induced EMF and phase current definitions in (5.31) and (5.32).

$$
\begin{aligned}
e_B &= E_1 \cos\left(\omega t - \frac{2\pi}{5}\right) + E_3 \cos\left(3\omega t - \frac{6\pi}{5}\right) \\
e_C &= E_1 \cos\left(\omega t - \frac{4\pi}{5}\right) + E_3 \cos\left(3\omega t - \frac{2\pi}{5}\right) \\
e_D &= E_1 \cos\left(\omega t - \frac{6\pi}{5}\right) + E_3 \cos\left(3\omega t - \frac{8\pi}{5}\right) \\
e_E &= E_1 \cos\left(\omega t - \frac{8\pi}{5}\right) + E_3 \cos\left(3\omega t - \frac{4\pi}{5}\right)
\end{aligned} \tag{5.31}
$$

$$
\begin{aligned}
i'_B(x) &= I'_1 \cos\left(\omega t - x\right) \\
i'_C(x) &= I'_1 \cos\left(\omega t - \pi + x\right) \\
i'_D(x) &= I'_1 \cos\left(\omega t + \pi - x\right) \\
i'_E(x) &= I'_1 \cos\left(\omega t + x\right)
\end{aligned} \tag{5.32}
$$

$$
T(x) = \frac{e_B\, i'_B(x) + e_C\, i'_C(x) + e_D\, i'_D(x) + e_E\, i'_E(x)}{\omega} \tag{5.33}
$$

The mean values and the peak-to-peak values of the torque function $T(x)$ is then obtained for x values between 0° and 90°, for both sinusoidal ($E_3 = 0$) and trapezoidal ($E_3 \neq 0$) induced EMF cases. For the trapezoidal case, $E_3 = 0.16E_1$ as in the studied machine topology. Figure 5.8 shows output torque of the machine, obtained analytically assuming open loop operation with a phase current of 20 A and an electrical frequency of 35 Hz.

Figures 5.9 and 5.10 show the mean torque and torque ripple (both as numeric and normalized forms) values for different values of reference phase angle, x. For a machine with sinusoidal induced EMF, $x = 36^\circ$ provides the least torque ripple (which is 0), not surprisingly as it was also obtained in the previous section. This value is also the value where the MMF trajectory becomes circular, and the rated torque value can be achieved with an overrating factor of 1.382 of the current magnitudes. For a machine with trapezoidal induced EMF, $x = 39^\circ$ provides the least torque ripple, which is non-zero. For both cases, $x = 54^\circ$ gives the maximum mean torque. However, torque ripple also increases to a higher level at this phase angle.

Up to this point in this section, the discussion is made and the results are shown considering an open-loop system and adopting analytical approaches. However, the

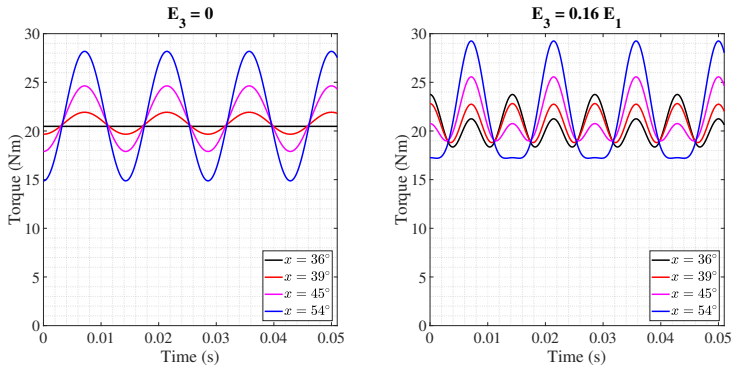

Figure 5.8: Output Torque of the Machine Obtained Analytically, in FTC Operation, for Different x Values

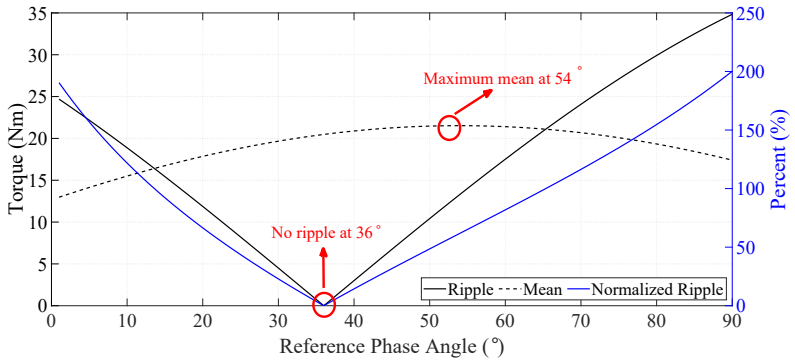

Figure 5.9: Optimum Current Phase Angle For a Machine With Sinusoidal Phase Induced EMF

behavior of the closed-loop speed controlled system would be different as the reference current values would continuously change in order to track the set point of the speed under a constant load torque.

Figure 5.11 shows the torque ripple and mean value of the torque as a function of x. On both graphs, discrete points are obtained with the drive simulation model in Simulink, where the continuous lines are analytically obtained functions for open-loop system. In Figure 5.11a, it is observed that the difference between the results that are analytically obtained and obtained with simulation increases. This is because the output torque at the same reference phase angle x is larger when the operation is

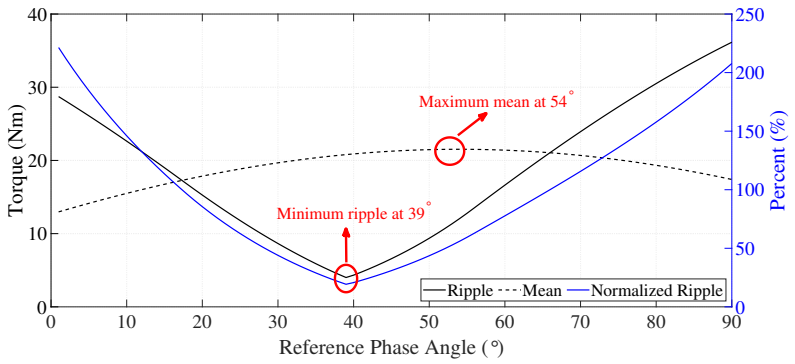

Figure 5.10: Optimum Current Phase Angle For a Machine With Trapezoidal Phase Induced EMF

closed-loop, in order to maintain the speed at the same load torque. The effect of this fact can also be observed in Figure 5.11b. The mean value of the output torque is nearly same for all values of x, as the operation for all cases is under the same load torque.

5.4.2 Modification of the Control Loop

For the simulation and experimental verification parts, the remedial phase currents' phase angles will be replaced with these three values and the machine performances will be compared under these circumstances. Therefore, new Clarke transform matrices should be defined for the new phase current references. No further modifications in the control loop structure are necessary for this method.

The derivation of the new Clarke matrices was explained in detail in Section 5.3.2, for the case where $x = 36°$. This approach can be generalized for a reference phase angle x. By replacing x with $39°$ and $54°$, the required transforms can be obtained. The generalized forward and inverse Clarke transformations as a function of x can be written as in (5.35) and (5.34), where the coefficients C_1 and C_2 in (5.35) can be obtained as in (5.36).

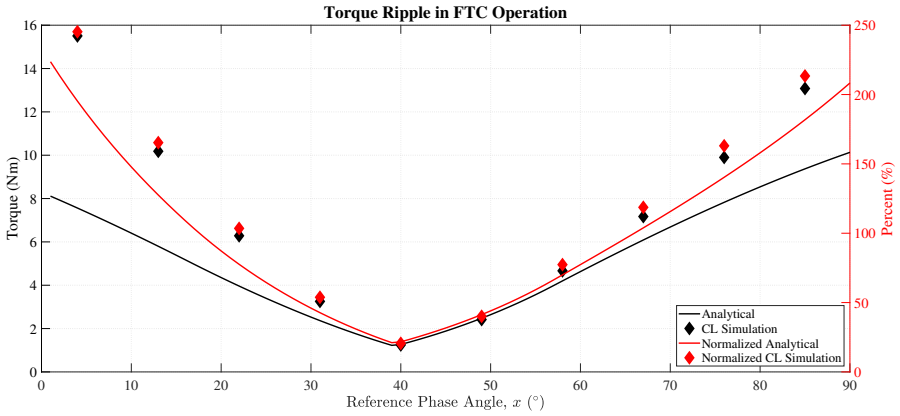

(a) Torque Ripple

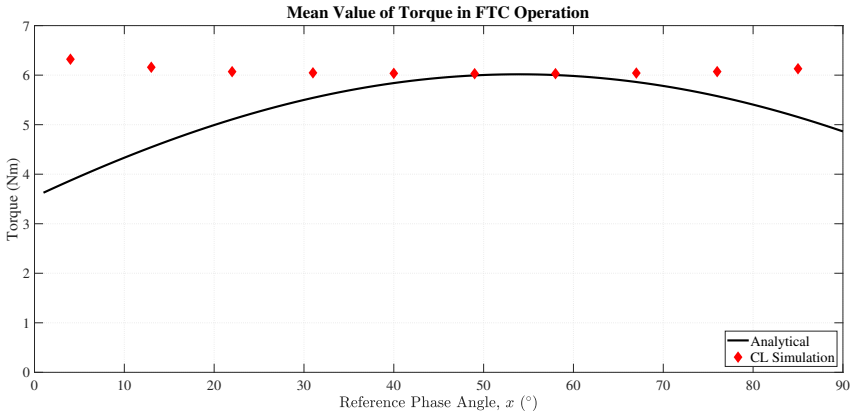

(b) Mean Value of Torque

Figure 5.11: Simulation Results: Output Torque as a Function of x, when the System is Closed-Loop and Speed-Controlled

$$T_{C,gen}^{-1} = \begin{bmatrix} \cos(x) & \sin(x) & 1 & 1 \\ \cos(\pi - x) & \sin(\pi - x) & -1 & 1 \\ \cos(\pi - x) & -\sin(\pi - x) & 1 & 1 \\ \cos(x) & -\sin(x) & -1 & 1 \end{bmatrix} \tag{5.34}$$

$\underbrace{\qquad}_{\boldsymbol{\alpha}}$ $\underbrace{\qquad}_{\boldsymbol{\beta}}$

$$T_{C,gen} = \begin{bmatrix} C_1 \cos(x) & C_1 \cos(\pi - x) & C_1 \cos(\pi - x) & C_1 \cos(x) \\ C_2 \sin(x) & C_2 \sin(\pi - x) & -C_2 \sin(\pi - x) & -C_2 \sin(x) \\ 0.25 & -0.25 & 0.25 & -0.25 \\ 0.25 & 0.25 & 0.25 & 0.25 \end{bmatrix} \tag{5.35}$$

$$\begin{aligned} C_1 &= \left(\boldsymbol{\alpha}^t \boldsymbol{\alpha}\right)^{-1} \\ C_2 &= \left(\boldsymbol{\beta}^t \boldsymbol{\beta}\right)^{-1} \end{aligned} \tag{5.36}$$

5.5 Drive Simulation for Open Circuit Fault Recovery Operation

To observe the overall drive system behavior and to verify the proposed FTC method, a series of drive simulations are made in MATLAB/Simulink environment, using the previously presented simulation model. No changes have been made on the model structure compared to its version that is used to simulate the normal operation of the five-phase drive, except for redefinition of Clarke transform blocks.

In the simulations, the motor operates at rated speed (220 rad/s, electrical) and at half-load (13 Nm). The duration of each simulation is 3 s. The motor operates in normal operation condition for the first second. At $t = 1s$, a 1-Ph OCF occurs in phase A and the FTC method is applied to the motor as of $t = 2s$.

As stated in the previous section, the simulation series investigates the effect of reference phase angle of the phase currents on the dynamic behavior of the system. On top of that, there are two major properties of the drive that directly affect the dynamic performance of the machine. One of these properties are the control coefficients of current PI controllers; and the other is the effect of the spatial asymmetry caused by the third order induced phase voltage. Therefore, in this section, mainly the effect of these properties and the reference phase angle values will be explained and discussed.

5.5.1 The Effect of Controller Aggressiveness

Due to the spatial asymmetry in a system with a 1-Ph OCF, or for any asymmetrical system, fundamental DQ currents (reference frame rotating at the fundamental electrical frequency) are composed of sine waves with even order frequencies [67]. As a result, it gets harder for the controller to set an oscillatory signal to a constant value.

Figure 5.12 shows the DQ currents of the machine for different reference phase angles of the current (x) with aggressive and moderate current controllers, for a machine with sinusoidal induced EMF. For the cases where controllers are relatively slow, in Figures 5.12a and 5.13a, it can be observed that the currents oscillate around the set points. By increasing the K_p and K_i coefficients of the current controllers, we can observe that these oscillations decrease and almost vanish. For the output torque, oscillations are also present. However, with increasing current controller aggression, the oscillations in the output torque also decrease for $x = 36°$, where this has no effect on the torque for $x = 54°$. This was an expected outcome considering the analysis results given in Figure 5.9.

As a result of the oscillating DQ currents when the controller parameters are smaller, the phase difference between phase currents cannot reach the desired values and their magnitudes become uneven. The comparison of the phase currents are presented in Figure 5.14.

On top of that, as the motor is speed-controlled, the need to define an extra overrating coefficient (such as in the methods discussed in Section 5.3.2 is not present. The speed controller sets the i_{q1} reference in order to satisfy the sufficient torque requirement to maintain the shaft speed. Hence, phase current magnitudes increase in proportional to the torque requirement, accordingly.

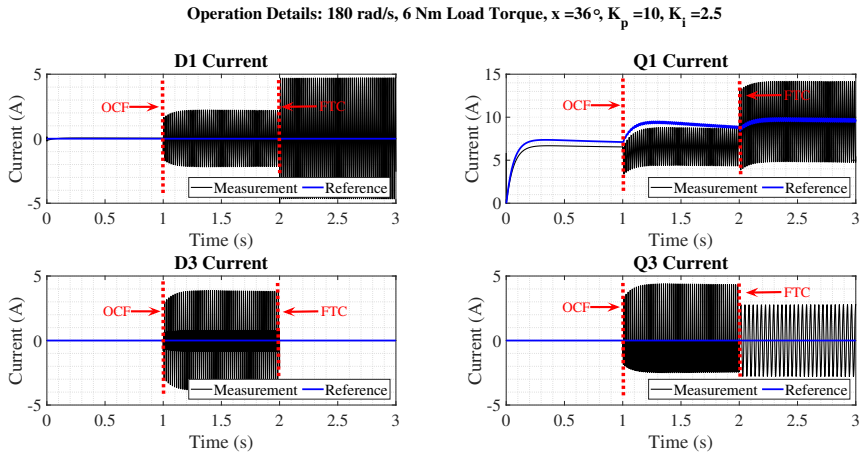

(a) $x = 36°$, $K_p = 10$, $K_i = 2.5$

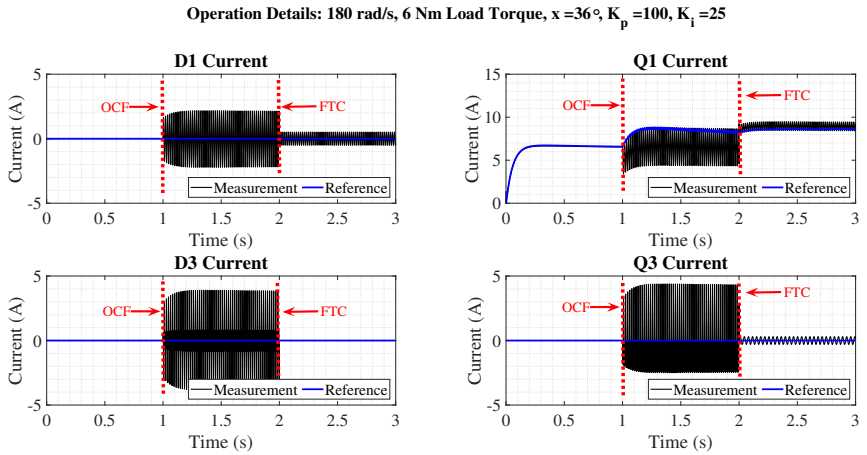

(b) $x = 36°$, $K_p = 100$, $K_i = 25$

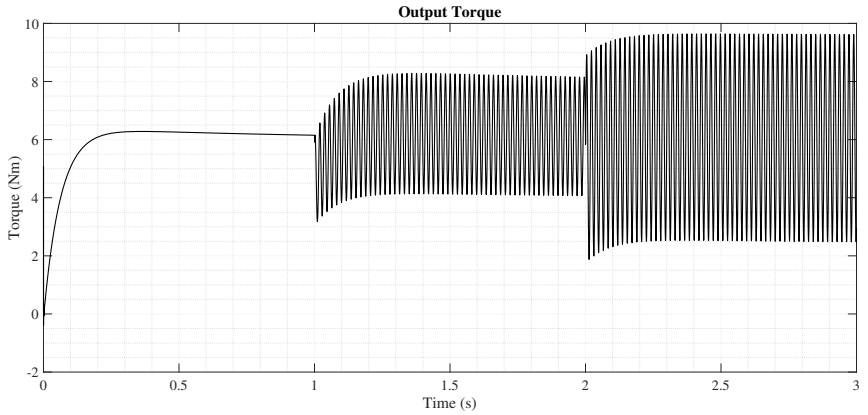

(c) $x = 36°$, $K_p = 10$, $K_i = 2.5$

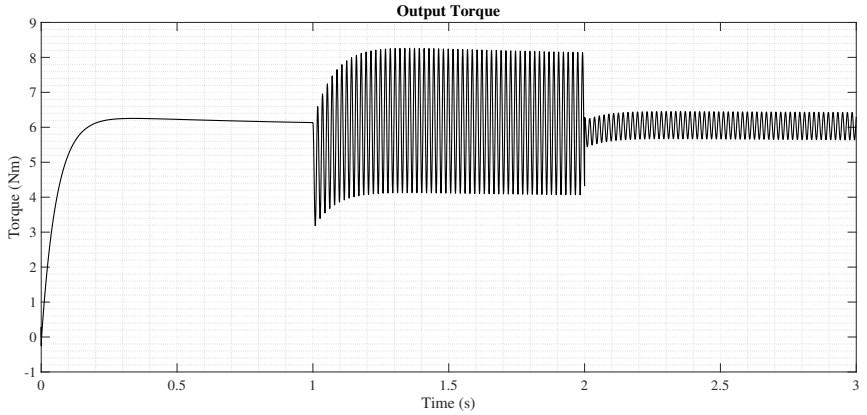

(d) $x = 36°$, $K_p = 100$, $K_i = 25$

Figure 5.12: Simulation Results: DQ Currents and Output Torque of the Machine in Normal, 1-Ph OCF and FTC Operation. Comparison For Different Controller Parameters at $x = 36°$, 180 rad/s Electrical Speed and 6 Nm Load Torque

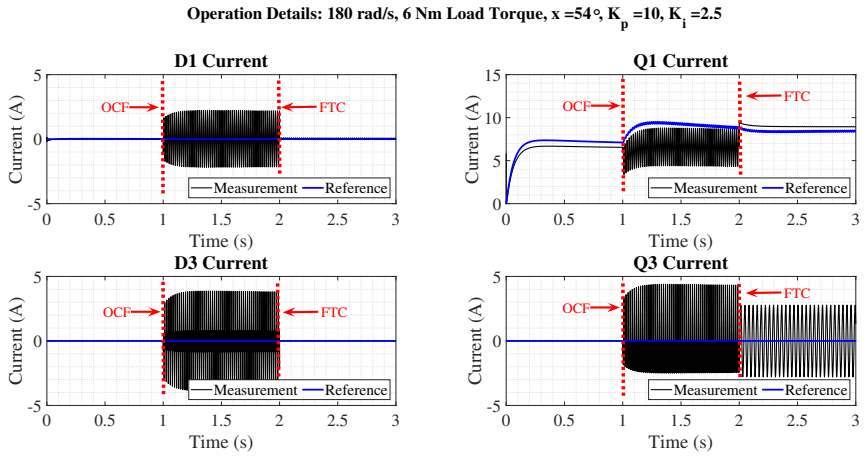

(a) $x = 54°$, $K_p = 10$, $K_i = 2.5$

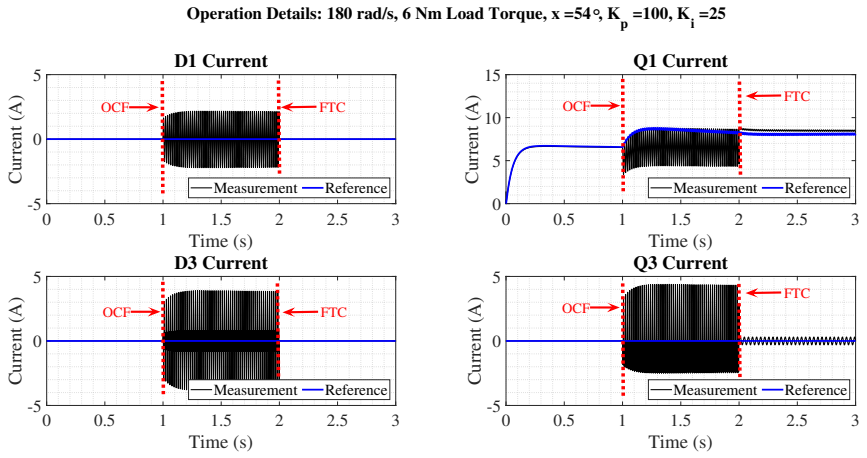

(b) $x = 54°$, $K_p = 100$, $K_i = 25$

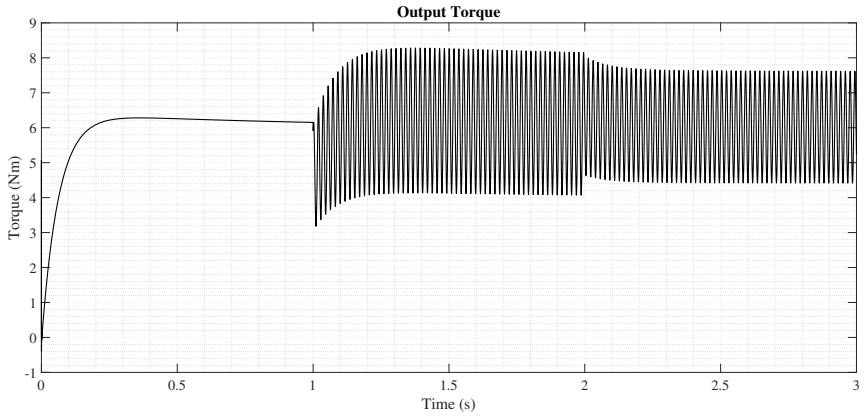

(c) $x = 54°$, $K_p = 10$, $K_i = 2.5$

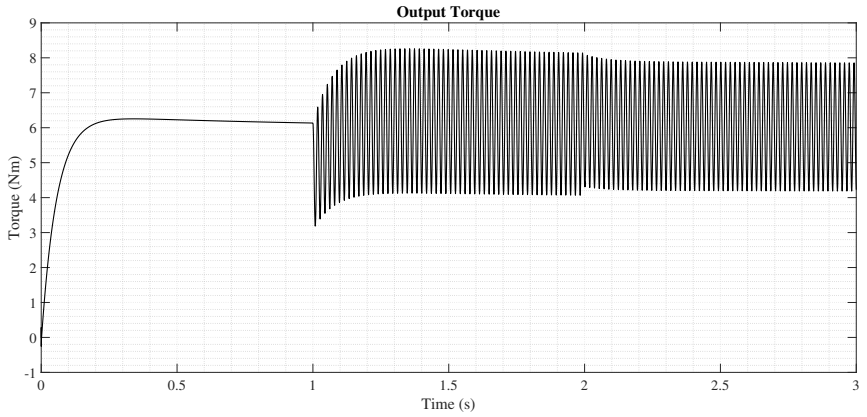

(d) $x = 54°$, $K_p = 100$, $K_i = 25$

Figure 5.13: Simulation Results: DQ Currents and Output Torque of the Machine in Normal, 1-Ph OCF and FTC Operation. Comparison For Different Controller Parameters at $x = 54°$, 180 rad/s Electrical Speed and 6 Nm Load Torque

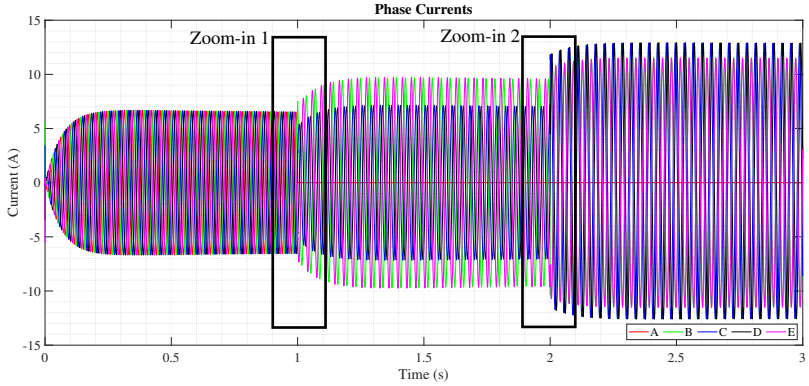

(a) $x = 36°$, $K_p = 10$, $K_i = 2.5$

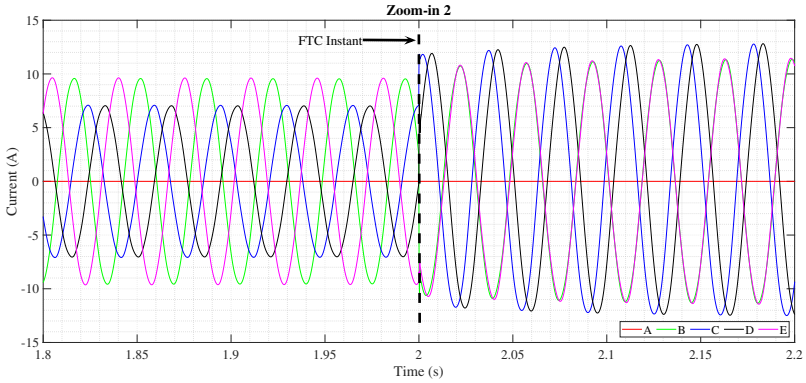

(b) Zoom-in 2, $x = 36°$, $K_p = 10$, $K_i = 2.5$

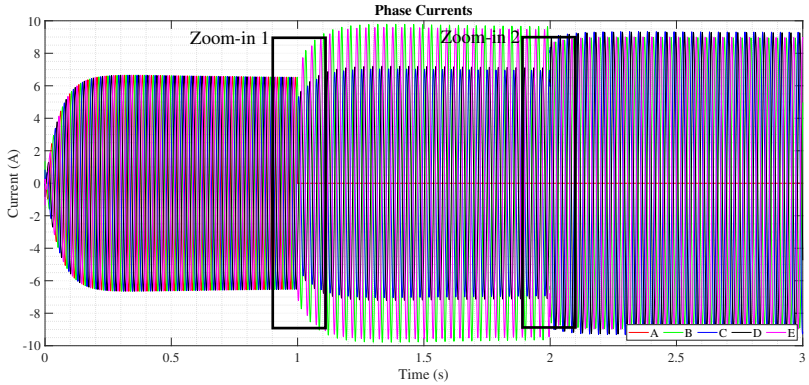

(c) $x = 36°$, $K_p = 100$, $K_i = 25$

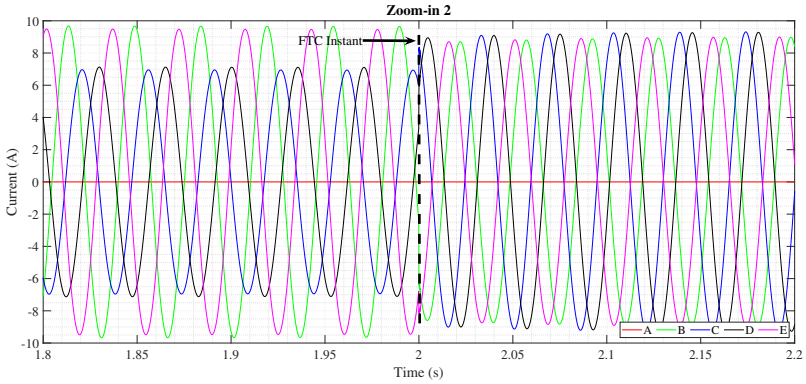

(d) Zoom-in 2, $x = 36°$, $K_p = 100$, $K_i = 25$

Figure 5.14: Simulation Results: Phase Currents of the Machine in FTC Operation. Comparison For Different Controller Parameters. Operation at 180 rad/s and 6 Nm Load Torque.

5.5.2 The Effect of the Third Harmonic Induced EMF

The drive simulations in the previous section are done for a machine with a sinusoidal induced EMF, in order to observe only the effect of the controller speed on the phase currents. The addition of the third order induced EMF and current to the system further makes it difficult to figure out the current controllers' behavior.

Figure 5.15 shows the DQ currents of the machine with a trapezoidal induced EMF, for both fast and slow current controller parameters. The dynamics of the machine with two different reference phase angle cases are compared in this section too. These two angles are $x = 39°$, that gives the least torque ripple and $x = 54°$, that gives the maximum average torque. The dynamic behavior of the motor with the third order induced voltage is similar to the one without the third order voltage: Oscillatory when the current controllers are slow and damped when the controllers are aggressive.

Similar conclusions can be made for the output torque. Torque graphs for the simulated cases are presented in Figure 5.16. Torque ripple can be eliminated by accelerating the current controller for $x = 39°$, but it cannot eliminate the large torque tipple when $x = 54°$.

Figure 5.17 shows the phase currents of the machine when $x = 39°$. With the additive or subtracting effect of the third order voltage on the phase current, the magnitude and phase difference between all phase currents differ a lot more than as it is in the previous case. For both cases, it can be observed that $x = 54°$ could be a wiser choice when only the phase current constraints are in consideration and the controllers are supposed to be slow.

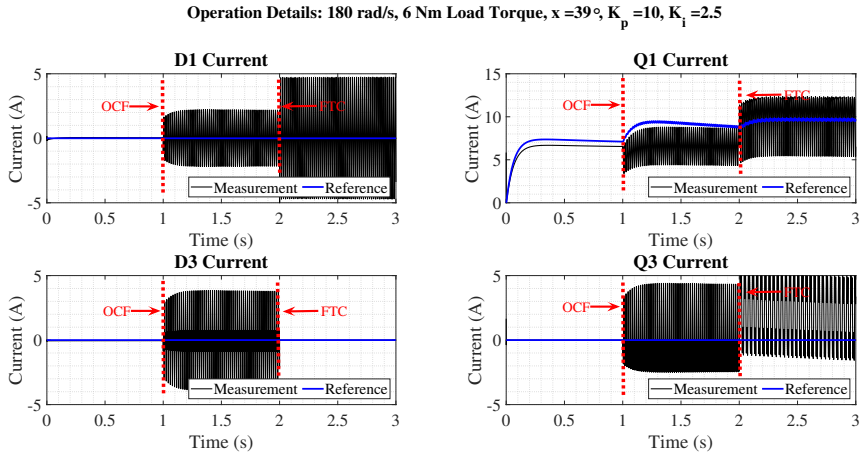

(a) $x = 39°$, $K_p = 10$, $K_i = 2.5$

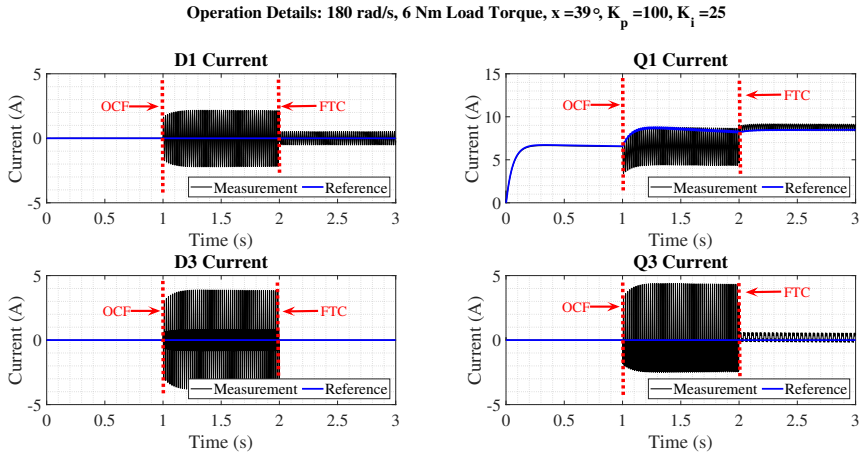

(b) $x = 39°$, $K_p = 100$, $K_i = 25$

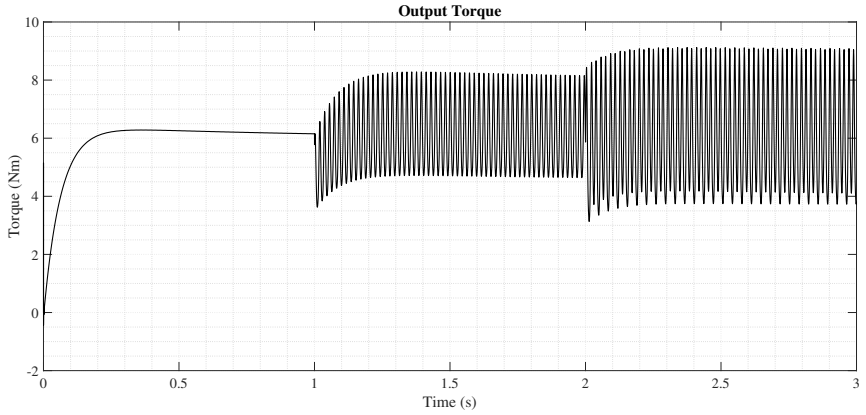

(c) $x = 39°$, $K_p = 10$, $K_i = 2.5$

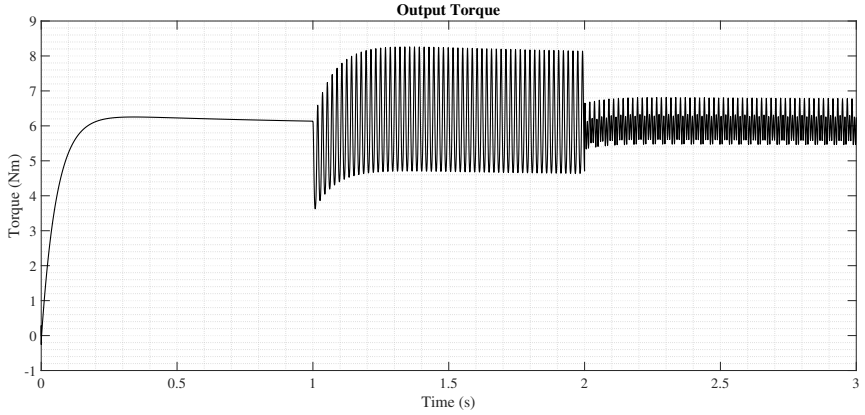

(d) $x = 39°$, $K_p = 100$, $K_i = 25$

Figure 5.15: Simulation Results: DQ Currents and Output Torque of the Machine in Normal, 1-Ph OCF and FTC Operation. Comparison For Different Controller Parameters at $x = 39°$, 180 rad/s Electrical Speed and 6 Nm Load Torque for a Machine With Trapezoidal Induced EMF

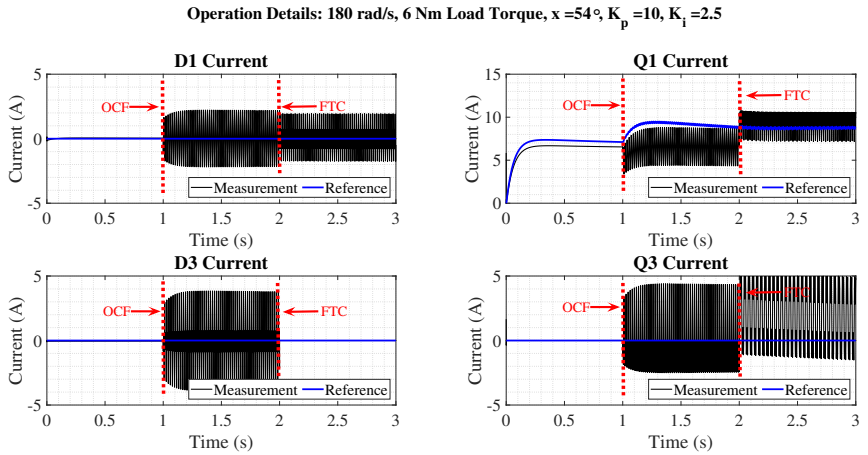

(a) $x = 54°$, $K_p = 10$, $K_i = 2.5$

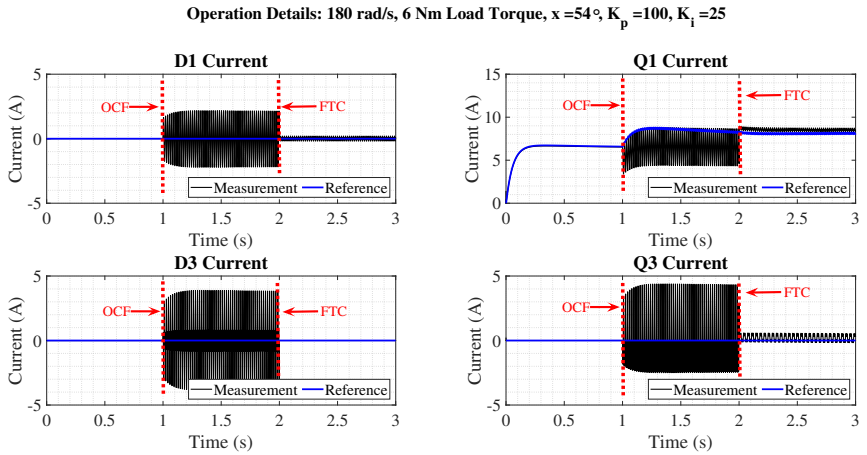

(b) $x = 54°$, $K_p = 100$, $K_i = 25$

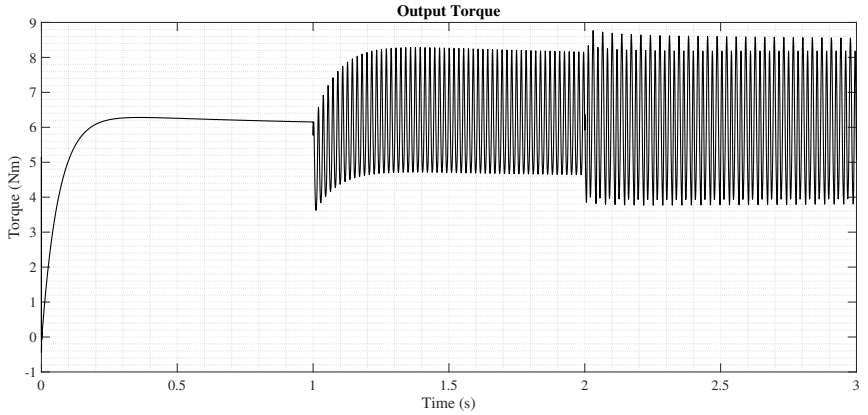

(c) $x = 54°$, $K_p = 10$, $K_i = 2.5$

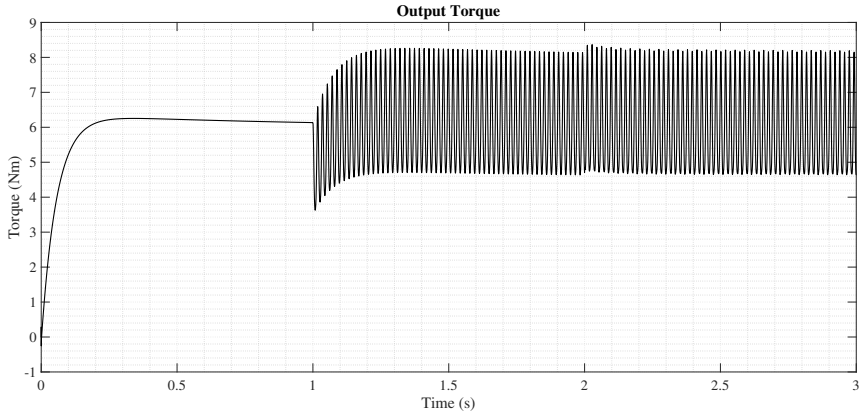

(d) $x = 54°$, $K_p = 100$, $K_i = 25$

Figure 5.16: Simulation Results: DQ Currents and Output Torque of the Machine in Normal, 1-Ph OCF and FTC Operation. Comparison For Different Controller Parameters at $x = 54°$, 180 rad/s Electrical Speed and 6 Nm Load Torque for a Machine With Trapezoidal Induced EMF

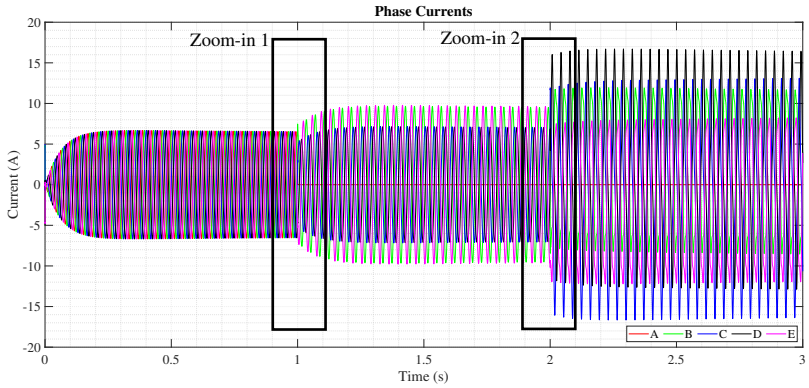

(a) $x = 39°$, $K_p = 10$, $K_i = 2.5$

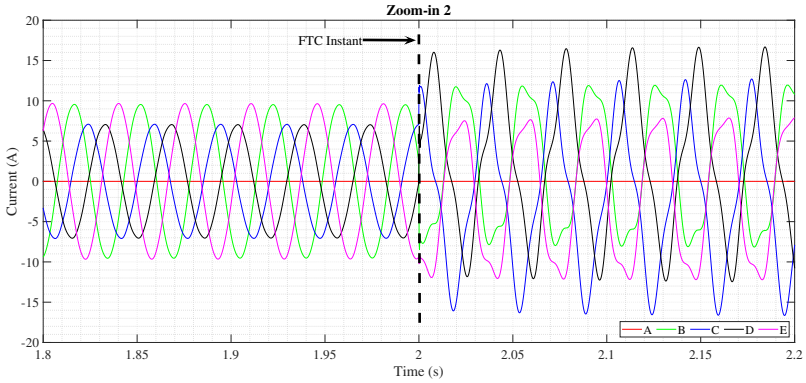

(b) Zoom-in 2, $x = 39°$, $K_p = 10$, $K_i = 2.5$

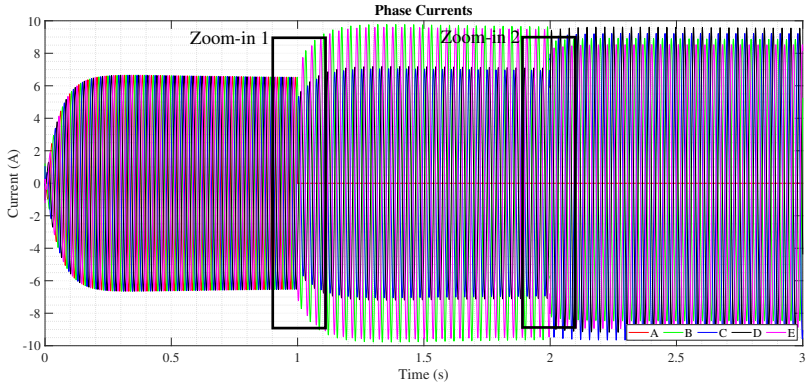

(c) $x = 39°$, $K_p = 100$, $K_i = 25$

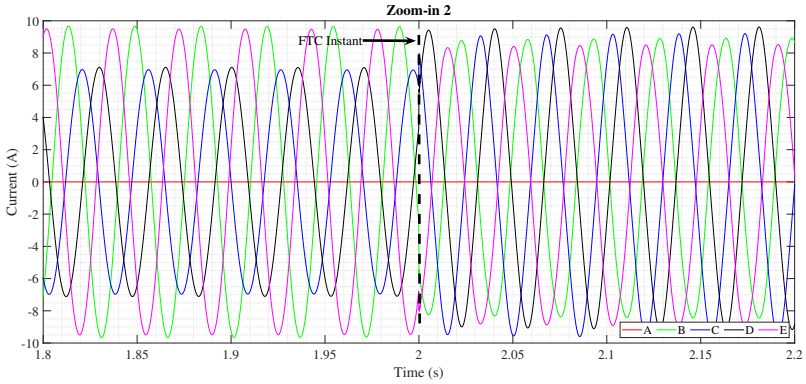

(d) Zoom-in 2, $x = 39°$, $K_p = 100$, $K_i = 25$

Figure 5.17: Simulation Results: Phase Currents of the Machine in FTC Operation. Comparison For Different Controller Parameters for a Machine With Trapezoidal Induced EMF

5.6 Experimental Results for 1-Ph OCF Recovery Operation

Proposed method of fault tolerant control is also realized and experimented on the manufactured prototype and its test bed. This experimental realization is performed in a safe operation region. The electrical speed of the machine is set to 180 rad/sec (430 rpm, mechanical) and the applied load torque by the DC generator is set to 6 Nm for FTC operation. During the experiments, the restraining element is the inverter. For a 10 minute operation at full load, GaN transistors' temperature rises up to 110°C, which may be, in fact a hazardous temperature level for these delicate (and relatively expensive) instruments. Therefore, the experiments for fault recovery operations are conducted at one-fourth of the rated load.

The experimental procedure is initially to generate a 1-Ph OCF using the circuit breaker between the machine and the inverter, and then to change the operation mode from normal control to FTC. These operation mode differences are shown in three "Zoom-in" windows in Figure 5.19. For this experiment, phase A is open-circuited to observe the system dynamics, and the control algorithm is developed accordingly. This algorithm can also be generalized as a FTC algorithm for and 1-Ph OCF occurrence in each possible phase by simply modifying the sequence of the row vectors of Clarke transform matrix. For such a generalization and in order to create a standalone control algorithm, it is also necessary to include fault diagnosis part to the algorithm. Both of these are out of the scope of this study.

The experiments of FTC have been repeated for $x = 36°$, $x = 39°$ and $x = 54°$. The current controllers are set to their maximum possible values (i.e. increasing the K_p and K_i values caused instability of the system). Under these conditions, recorded DQ currents, phase currents and output torque are presented in Figures 5.18, 5.19 and 5.20, respectively.

Also, it should be noted that the phase currents and the output torque are recorded using two four-channel DSOs; DQ currents and electrical speed are recorded a user interface designed in MATLAB, where the data is obtained via the serial communication port of the DSP. That is why, time axes for phase currents and the output torque start at a negative value and the ones for DQ currents and the speed start at 0.

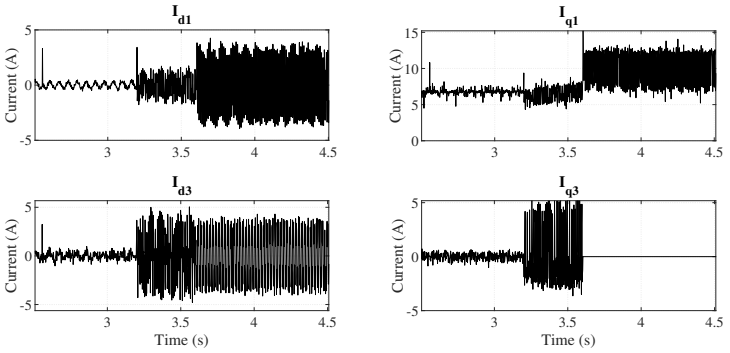

(a) $x = 36°$

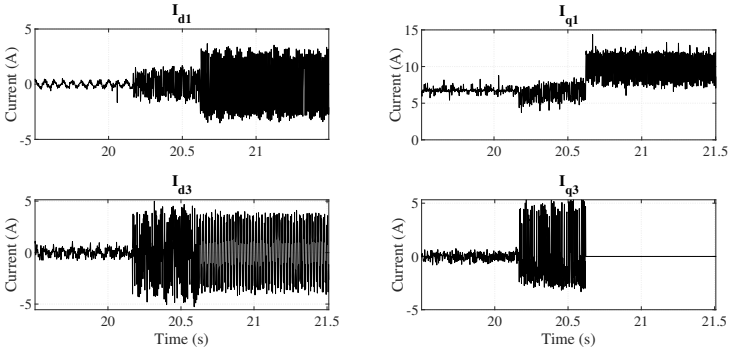

(b) $x = 39°$

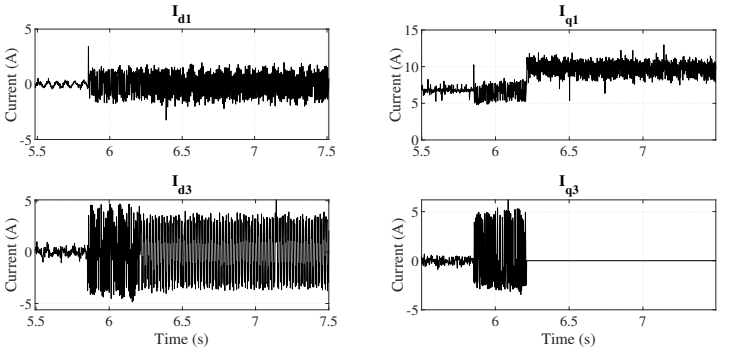

(c) $x = 54°$

Figure 5.18: Experimental Results: DQ Currents of the Machine in FTC Operation at 6 Nm Load Torque and 180 rad/s Electrical Speed. Comparison For Different Reference Phase Angles, x. Test Sequence: Normal Operation, Fault Occurrence, Fault Tolerant Control.

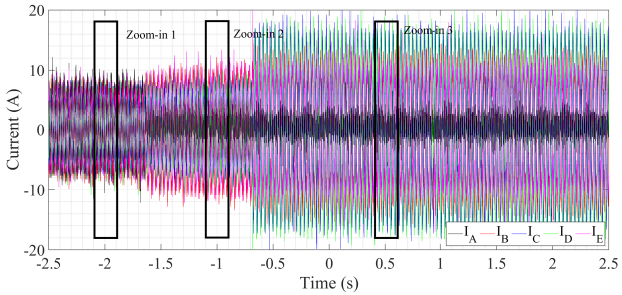

(a) $x = 36°$

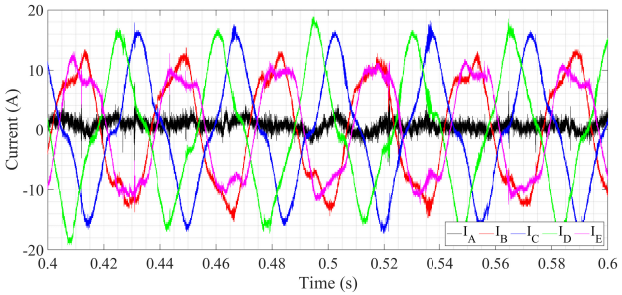

(b) $x = 36°$, Window "Zoom-in 3"

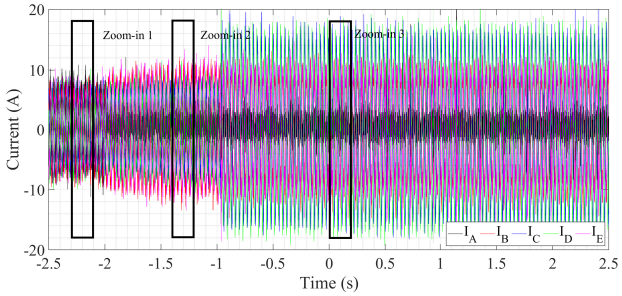

(c) $x = 39°$

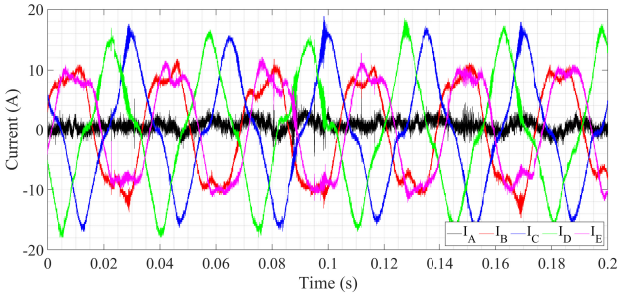

(d) $x = 39°$, Window "Zoom-in 3"

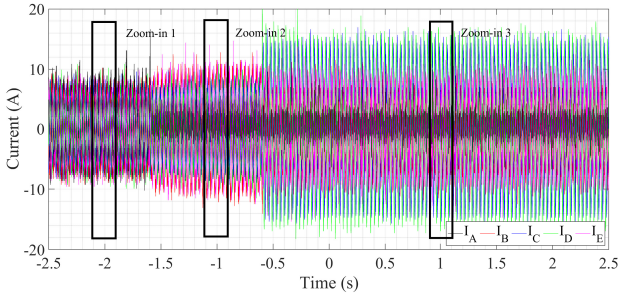

(e) $x = 54°$

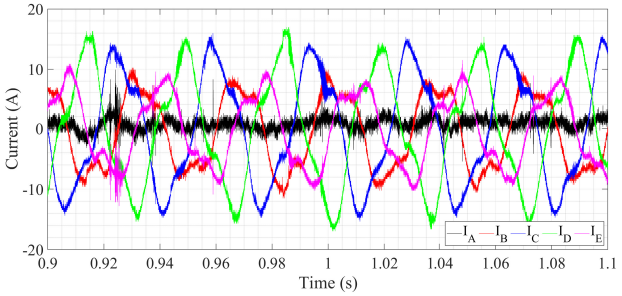

(f) $x = 54°$, Window "Zoom-in 3"

Figure 5.19: Experimental Results: Phase Currents of the Machine in FTC Operation at 6 Nm Load Torque and 180 rad/s Electrical Speed. Comparison For Different Reference Phase Angles, x. Test Sequence: Normal Operation, Fault Occurrence, Fault Tolerant Control.

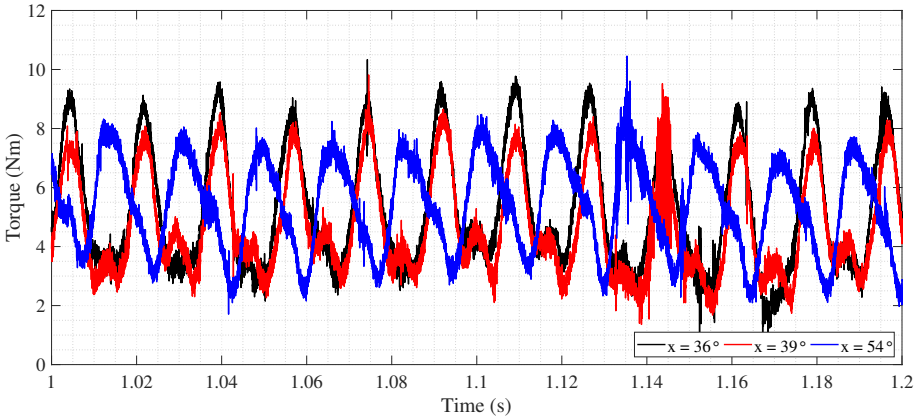

Figure 5.20: Experimental Results: Output Torque of the Machine in FTC Operation at 6 Nm Load Torque. Comparison For Different Reference Phase Angles, x. Test Sequence: Normal Operation, Fault Occurrence Fault Tolerant Control.

Figure 5.18 shows us that the current controllers are quite slower than the required level. Similar to the simulation results obtained in Figure 5.15, oscillations at the double electrical frequency are present in the DQ currents, where the least of these oscillations are observed for the case where $x = 54°$. These oscillations show that the phase currents do not reach the reference values with desired phase differences between each of them and with equal magnitudes, as explained after the results of the drive simulations with a slower current controller. The experimental phase current waveforms showing the mentioned issue are presented in Figure 5.19.

For all these three experiments, the output torque is also recorded for a period that covers the normal operation, 1-Ph OCF occurrence and the FTC operation sequentially, similar to the window of the DQ currents. However, the mechanical structure of the test-bed is not very robust, precisely integrated. There are some loose connected mechanical joints, most probably misalignment problems and additional counter-torque producing sources in the mechanical system. These problems cause the torque measurement to be obtained in a very oscillatory form and eliminates the torque ripple information when it is filtered. Therefore, the output torque is obtained by calculation using the phase currents and (4.17).

Figure 5.20 shows the analytically obtained torque graphs for different reference phase angles at the same load torque of 6 Nm, using phase current measurements. Comparing these torque waveforms with the ones that are obtained analytically, it can be said that the waveform patterns are similar for different reference phase angles.

The machine is not expected to have torque ripple when normally operating but it is definitely expected for the operation with 1-Ph OCF. Also, the mean torque measurements for the three cases are reliable and it can be observed that thanks to the speed controller, the torque level and the output speed are maintained for 1-Ph OCF and FTC operations.

5.7 Conclusion and Discussion

This chapter discussed the fault tolerant control methodology of the five-phase AF-PMSM. Initially, the phase currents of the machine under 1-Ph OCF have been analytically calculated. Calculation results showed that there was an unbalance between phase currents by means of both magnitude and phase. For the operation points of higher load, this unbalance and the exceed of safe current limits, as well as uneven heating and temperature distribution of both machine and motor driver can be dangerous and fatally harmful, especially for the motor drive.

After that, fault tolerant control, or fault recovery control methods were presented. The main purpose of FTC is defining new current waveforms to obtain the same torque as in normal operating condition. The most common approach to achieve this is choosing the current references that form the same rotating MMF before the 1-Ph OCF. Additional constraints can also be defined according to the requirements and the motor type such as torque ripple minimization, equal Joule losses criterion and Joule loss minimization.

This study mainly focused on torque ripple minimization, torque maximization with equal Joule loss criterion. As the machine is a machine with trapezoidal induced EMF, redefining the phase currents that shapes the pre-fault rotating MMF did not satisfy the requirements. Therefore, third harmonic current injection method was investigated.

This method includes generating current references using both fundamental and third harmonics that eliminates the torque ripple. A drawback of this method is the control part: As the DQ reference currents do not become constant values, tracking the set point becomes harder for the current controllers.

On top of that, an alternative solution to the torque ripple problem was also proposed. This method aimed to excite the windings with only fundamental currents, but with an optimum phase angle that provides maximum mean torque and minimum torque ripple. The responses of the drive to the excitation currents with these reference phase angles have been compared for different controller parameters and different induced EMF shapes of the machine. For a machine with trapezoidal induced EMF, a reference phase angle of 39° reduces the torque ripple to 15%, compared to the case with 54°. Also, it is observed that the current controllers should be more aggressive than they were in normal operation in order to eliminate the oscillations of the DQ currents. Otherwise, the phase currents cannot be generated at desired the magnitude and phase difference.

Finally, the fault tolerant control has been performed on the experimental setup, on the manufactured prototype of the five-phase AFPMSM. The current controllers could not be tuned as too aggressive, because of the current limit of the inverter. Under these circumstances, the fault tolerant operation has been experimented and the results were similar to the simulation results that were obtained with slower current controllers.

Looking from a broader perspective, it can be concluded that the air-cored topology is a big trade-off between ease of manufacturing and ease of controllability. In theory, fault tolerant control is quite easy since it only involves changing the phase difference between the remaining healthy phases. However, the spatial asymmetry in the machine under a single-phase open circuit fault causes continuous oscillations in the DQ currents of the machine. The elimination of these oscillations requires aggressive controllers or modern control techniques, where these are not possible unless the measurement noise or current ripple caused by switching is eliminated from the system. Once this criterion is satisfied, fault tolerant control can be achieved in a machine.

CHAPTER 6

CONCLUSIONS AND FUTURE WORK

Axial flux permanent magnet synchronous machines are quite advantageous compared to their radial flux equivalents by means of torque density thanks to their larger diameters; hence, they are preferred for the applications that require high torque over radial flux machines. Considering the reliability requirement of the modern industrial drives that are used in safety-critical industrial applications, this study came up with a fault tolerant, five-phase air-cored AFPMSM design with a novel winding structure. The main motivation for adopting this novel, air-cored winding type was its high current carrying capability and the insulating epoxy resin cover of the coils. Both of these aspects are quite important by means of fault tolerance, as the epoxy cover completely eliminates the inter-turn, phase-to-phase or any kind of short circuit risk in the machine which is the most common starting point of stator-related failures and that can easily spread through the whole winding. Besides, high current carrying capability is also an advantage as it is possible to exceed the rated current value in the remedial operation of a possible open circuit fault.

Throughout the study, initially, the design of the machine is covered. Starting with analytical calculations, basic machine parameters regarding its size and phase variables were determined. These results were also verified based on the simulation results obtained with finite element modeling. The analysis results were also verified experimentally, based on the experiments performed on a machine prototype operating in the generating mode.

After the design and design verification parts, the main focus of the study was five-phase drives in general sense. Having defined the parameters, equations and transforms of a five-phase drive, a simulation model was built in Simulink to observe the

behavior of the electric drive based on the defined analytical model. Lastly, open circuit fault occurrence cases were investigated, current levels that will flow through the windings at the instant of fault occurrence, fault mitigation strategies with different constraints were analyzed. Proposed fault tolerant control schemes were tried successfully on the drive simulation model. Both healthy and faulty operations of the machine were verified experimentally on the machine prototype driven by a custom GaN-based inverter.

The primary conclusions that can be drawn from this study can be summarized as follows:

- The large current carrying capability of the stator winding composed of flat wires has been verified since it provided a superior thermal performance under loaded operation.
- Conventional magnetic equivalent circuit approach in the design procedure of a machine by ignoring the leakage flux is misleading for air-cored machines due to their large equivalent air-gaps, which dramatically increases the leakage. When the leakage flux was also included in the calculations, analytical and FEA results of electromagnetic quantities were compatible with only a difference of $5-7\%$.
- It is concluded that the limiting element of the drive in experimental work was the inverter since its temperature surpassed 110° in only 20 minutes under loaded operation.
- One of the major advantages of adopting a five-phase topology was the ability to enhance the output torque with third harmonic flux linkage and current. This asset was indirectly shown in the closed-loop speed-controlled operation. The motor speed was kept constant under the same load torque when the machine was drawing phase currents of lower magnitude for the case of third harmonic current injection.
- Low inductance was the biggest disadvantage of air-cored AFPMSM because it caused more difficult controllability. Unlike the machines with high inductance, the phase windings did not as much as behave as low pass filter and did not

fully eliminate the noise of the current waveform caused by the controller and the switching. This was in the way of speeding up the controllers for them to make DQ currents track the set points.

- Even if it is mostly stated that the primary approach for a fault tolerant control strategy should be reforming the air-gap MMF as it was before the fault occurrence in the literature, this may not be sufficient to eliminate the torque ripple caused by fault. The control strategy for a machine under open circuit fault depends on the induced EMF type of the machine and additional operation constraints. It was shown that the remedial phase currents that provide zero torque ripple for a machine with sinusoidal induced EMF did not eliminate the torque ripple in the studied topology. Therefore, an optimum current reference set was obtained to obtain the least torque ripple for fault remedial operation.
- When the machine is closed-loop speed controlled, it is not necessary to define a coefficient for the remedial phase currents that reforms the air-gap MMF as it was before the fault. It was shown with both simulations and experimental results that the speed controller provided the optimal set point to i_{q1} that increased the output torque to the required level.

This study can also further be improved with several actions that could be taken. First of all, data acquisition devices (current sensors and the encoder) could be replaced with the ones that have better resolution, that have the capability to obtain less noisy measurements. Another alternative to this is the implementation of digital filters to eliminate the noise in the phase current measurements. Basic low pass filter or probabilistic filters such as Kalman filter are potential candidates for current measurement filtering tools. These methods would improve the performance of the current controllers and the fault tolerant control algorithm.

Another relevant research area that is a candidate subsequent to this study is the investigation of fault diagnosis methods. As explained in Chapter 5, the standalone operation of the system requires the generalization of the fault tolerant control algorithms as well as integration of fault diagnosis methods to the system. Therefore, online and computationally inexpensive condition monitoring techniques are worth exploring.

REFERENCES

[1] P. Arumugam, *Design and modelling of permanent magnet machine's windings for fault-tolerant applications*. PhD thesis, University of Nottingham, Nottingham, UK, December 2013.

[2] A. da Silva, *Induction motor fault diagnostic and monitoring methods*. PhD thesis, 05 2006.

[3] "Why 1% efficiency improvement means so much." `https://news.mgmotor.eu/why-1-percent-efficiency-improvement-means-so-much/`, Apr 2021. Accessed: 2021-08-28.

[4] D. Moreels and P. Leijnen, "This inside-out motor for evs is power dense and (finally) practical." `https://spectrum.ieee.org/this-insideout-motor-for-evs-is-power-dense-and-finally-practical`, Sep 2019. Accessed: 2021-08-28.

[5] G. Çakal, "Axial flux permanent magnet machine with novel flat winding made of conductor sheet," Master's thesis, Middle East Technical University, Ankara, Turkey, 2020.

[6] G. J. Atkinson, J. W. Bennett, B. C. Mecrow, D. J. Atkinson, A. G. Jack, and V. Pickert, "Fault tolerant drives for aerospace applications," *2010 6th International Conference on Integrated Power Electronics Systems, CIPS 2010*, pp. 1–7, 2011.

[7] A. El-Refaie, "Fault-tolerant permanent magnet machines: a review," *IET Electric Power Applications*, vol. 5, pp. 59–74(15), January 2011.

[8] C. M. Verrelli, S. Bifaretti, E. Carfagna, A. Lidozzi, L. Solero, F. Crescimbini, and M. Di Benedetto, "Speed sensor fault tolerant pmsm machines: From position-sensorless to sensorless control," *IEEE Transactions on Industry Applications*, vol. 55, no. 4, pp. 3946–3954, 2019.

[9] A. Gholipour, M. Ghanbari, E. Alibeiki, and M. Jannati, "Speed sensorless fault-tolerant control of induction motor drives against current sensor fault," *Electrical Engineering*, vol. 103, pp. 1493–1513, Jun 2021.

[10] P. Lezana, J. Pou, T. Meynard, J. Rodriguez, S. Ceballos, and F. Richardeau, "Survey on fault operation on multilevel inverters," *IEEE Transactions on Industrial Electronics*, vol. 57, pp. 2207–2218, July 2010.

[11] J. He, C. Somogyi, A. Strandt, and N. A. O. Demerdash, "Diagnosis of stator winding short-circuit faults in an interior permanent magnet synchronous machine," in *2014 IEEE Energy Conversion Congress and Exposition (ECCE)*, pp. 3125–3130, 2014.

[12] J. G. Cintron-Rivera, S. N. Foster, and E. G. Strangas, "Mitigation of turn-to-turn faults in fault tolerant permanent magnet synchronous motors," *IEEE Transactions on Energy Conversion*, vol. 30, no. 2, pp. 465–475, 2015.

[13] M. Riera-Guasp, J. A. Antonino-Daviu, and G.-A. Capolino, "Advances in electrical machine, power electronic, and drive condition monitoring and fault detection: State of the art," *IEEE Transactions on Industrial Electronics*, vol. 62, no. 3, pp. 1746–1759, 2015.

[14] M. Zafarani, E. Bostanci, Y. Qi, T. Goktas, and B. Akin, "Interturn short-circuit faults in permanent magnet synchronous machines: An extended review and comprehensive analysis," *IEEE Journal of Emerging and Selected Topics in Power Electronics*, vol. 6, no. 4, pp. 2173–2191, 2018.

[15] G. Berardi and N. Bianchi, "Design guideline of an ac hairpin winding," in *2018 XIII International Conference on Electrical Machines (ICEM)*, pp. 2444–2450, IEEE, 2018.

[16] G. Berardi, S. Nategh, N. Bianchi, and Y. Thioliere, "A comparison between random and hairpin winding in e-mobility applications," in *IECON 2020 The 46th Annual Conference of the IEEE Industrial Electronics Society*, pp. 815–820, 2020.

[17] T. Ishigami, Y. Tanaka, and H. Homma, "Motor stator with thick rectangular

wire lap winding for hevs," *IEEE Transactions on Industry Applications*, vol. 51, no. 4, pp. 2917–2923, 2015.

[18] P. Mancinelli, S. Stagnitta, and A. Cavallini, "Lifetime analysis of an automotive electrical motor with hairpin wound stator," in *2016 IEEE Conference on Electrical Insulation and Dielectric Phenomena (CEIDP)*, pp. 877–880, 2016.

[19] B. Mecrow, "Fault-tolerant permanent magnet machine drives," *IEE Proceedings - Electric Power Applications*, vol. 143, pp. 437–442(5), November 1996.

[20] X. Deng, H. Wu, B. Gu, G. Atkinson, B. Mecrow, and V. Pickert, "Present and future of fault tolerant drives applied to transport applications," in *CIPS 2020; 11th International Conference on Integrated Power Electronics Systems*, pp. 1–8, 2020.

[21] N. Bianchi, E. Fornasiero, and S. Bolognani, "Thermal analysis of a five-phase motor under faulty operations," in *8th IEEE Symposium on Diagnostics for Electrical Machines, Power Electronics Drives*, pp. 431–436, 2011.

[22] B. Mecrow, A. Jack, D. Atkinson, S. Green, G. Atkinson, A. King, and B. Green, "Design and testing of a four-phase fault-tolerant permanent-magnet machine for an engine fuel pump," *IEEE Transactions on Energy Conversion*, vol. 19, no. 4, pp. 671–678, 2004.

[23] M. J. Duran and F. Barrero, "Recent advances in the design, modeling, and control of multiphase machines—part ii," *IEEE Transactions on Industrial Electronics*, vol. 63, no. 1, pp. 459–468, 2016.

[24] E. Levi, "Multiphase electric machines for variable-speed applications," *IEEE Transactions on Industrial Electronics*, vol. 55, no. 5, pp. 1893–1909, 2008.

[25] A. Tani, M. Mengoni, L. Zarri, G. Serra, and D. Casadei, "Control of multiphase induction motors with an odd number of phases under open-circuit phase faults," *IEEE Transactions on Power Electronics*, vol. 27, no. 2, pp. 565–577, 2012.

[26] F. Wu, P. Zheng, and T. M. Jahns, "Six-phase fault-tolerant permanent magnet motor drives with reduced switch counts: Topology comparisons and hardware demonstration," in *2015 IEEE Transportation Electrification Conference and Expo (ITEC)*, pp. 1–6, 2015.

[27] F. Wu, P. Zheng, Y. Sui, B. Yu, and P. Wang, "Design and experimental verification of a short-circuit proof six-phase permanent magnet machine for safety critical applications," *IEEE Transactions on Magnetics*, vol. 50, no. 11, pp. 1–4, 2014.

[28] J. J. Aciego, I. González Prieto, and M. J. Duran, "Model predictive control of six-phase induction motor drives using two virtual voltage vectors," *IEEE Journal of Emerging and Selected Topics in Power Electronics*, vol. 7, no. 1, pp. 321–330, 2019.

[29] M. T. Abolhassani and H. A. Toliyat, "Fault tolerant permanent magnet motor drives for electric vehicles," *2009 IEEE International Electric Machines and Drives Conference, IEMDC '09*, vol. m, pp. 1146–1152, 2009.

[30] S. Dwari and L. Parsa, "Fault-tolerant control of five-phase permanent-magnet motors with trapezoidal back EMF," *IEEE Transactions on Industrial Electronics*, vol. 58, pp. 476–485, feb 2011.

[31] A. Hosseyni, R. Trabelsi, M. F. Mimouni, and A. Iqbal, "Vector controlled five-phase permanent magnet synchronous motor drive," *IEEE International Symposium on Industrial Electronics*, pp. 2122–2127, 2014.

[32] L. Parsa, H. A. Toliyat, S. S. Member, H. A. Toliyat, and S. S. Member, "Five-phase permanent-magnet motor drives," *IEEE Transactions on Industry Applications*, vol. 41, no. 1, pp. 30–37, 2005.

[33] F. Locment, E. Semail, and F. Piriou, "Design and study of a multiphase axial-flux machine," *IEEE Transactions on Magnetics*, vol. 42, no. 4, pp. 1427–1430, 2006.

[34] S. Wu, C. Tian, W. Zhao, J. Zhou, and X. Zhang, "Design and analysis of an integrated modular motor drive for more electric aircraft," *IEEE Transactions on Transportation Electrification*, vol. 6, no. 4, pp. 1412–1420, 2020.

[35] J. Wang, Y. Li, and Y. Han, "Integrated Modular Motor Drive Design With <roman>GaN</roman> Power <roman>FETs</roman>," *IEEE Transactions on Industry Applications*, vol. 51, no. 4, pp. 3198–3207, 2015.

[36] G. H. Bayazıt, M. Uğur, and O. Keysan, "Fault tolerance capabilities of three, four and six-phase configurations of a 24 slot modular pmsm," in *2019 IEEE 13th International Conference on Power Electronics and Drive Systems (PEDS)*, pp. 1–6, 2019.

[37] C. Chan, "Axial-field electrical machines - design and applications," *IEEE Transactions on Energy Conversion*, vol. EC-2, no. 2, pp. 294–300, 1987.

[38] A. Cavagnino, M. Lazzari, F. Profumo, and A. Tenconi, "A comparison between the axial flux and the radial flux structures for pm synchronous motors," *IEEE Transactions on Industry Applications*, vol. 38, no. 6, pp. 1517–1524, 2002.

[39] H. S. Ordóñez, *Analysis and Design of Fault Tolerant Axial Flux Permanent Magnet Synchronous Motors*. PhD thesis, Department of Electrical Engineering, Universitat Politècnica de Catalunya, Barcelona, Spain, 2014.

[40] X. Wang, M. Zhao, L. Tang, W. Xu, and M. R. Islam, "Fault-Tolerant Analysis and Design of AFPMSM With Multi-Disc Type Coreless Open-End Winding," *IEEE Access*, vol. 8, pp. 171744–171753, 2020.

[41] A. S. McDonald, N. Al-Khayat, D. Belshaw, M. Ravilious, A. Kumaraperumal, A. M. Benatamane, M. Galbraith, D. Staton, K. Benoit, and M. Mueller, "1mw multi-stage air-cored permanent magnet generator for wind turbines," in *6th IET International Conference on Power Electronics, Machines and Drives (PEMD 2012)*, pp. 1–6, 2012.

[42] C. Bianchini, A. Torreggiani, D. David, M. Davoli, and A. Bellini, "Fault tolerance analysis of a ironless pm machine for energy storage," in *2020 IEEE Energy Conversion Congress and Exposition (ECCE)*, pp. 4499–4504, 2020.

[43] B. Xia, J.-X. Shen, P. C.-K. Luk, and W. Fei, "Comparative study of air-cored axial-flux permanent-magnet machines with different stator winding configurations," *IEEE Transactions on Industrial Electronics*, vol. 62, no. 2, pp. 846–856, 2015.

[44] M. Popescu, J. Goss, D. A. Staton, D. Hawkins, Y. C. Chong, and A. Boglietti, "Electrical vehicles—practical solutions for power traction motor systems,"

IEEE Transactions on Industry Applications, vol. 54, no. 3, pp. 2751–2762, 2018.

[45] F. Karakaya, O. S. Alemdar, and O. Keysan, "Layout based ultra-fast short-circuit protection technique for parallel connected gan hemts," *IEEE Journal of Emerging and Selected Topics in Power Electronics*, pp. 1–1, 2021.

[46] "LAUNCHXL-F28379D c2000 delfino mcu f28379d launchpad™ development kit." `https://www.ti.com/tool/LAUNCHXL-F28379D`. Accessed: 2021-08-10.

[47] R. Qu and T. Lipo, "Analysis and modeling of air-gap and zigzag leakage fluxes in a surface-mounted permanent-magnet machine," *Industry Applications, IEEE Transactions on*, vol. 40, pp. 121 – 127, 02 2004.

[48] A. Mcdonald, *Structural analysis of low speed, high torque electrical generators for direct drive renewable energy converters*. PhD thesis, 01 2008.

[49] A. Parviainen, *Design of axial-flux permanent-magnet low-speed machines and performance comparison between radial-flux and axial-flux machines*. PhD thesis, Lappeenranta University of Technology, Lappeenranta, Finland, 2005.

[50] G. Çakal and O. Keysan, "Flat winding made of aluminum or copper sheet for axial flux machines," *IET Electric Power Applications*, vol. 15, no. 4, pp. 429–440, 2021.

[51] T. Lipo, *Analysis of Synchronous Machines, Second Edition*. Taylor & Francis, 2012.

[52] M. H. Jens Schweickhardt, Kevin Hermanns, "Tips & tricks on double pulse testing," tech. rep., Munich, Germany, 2021.

[53] C. J. O'Rourke, M. M. Qasim, M. R. Overlin, and J. L. Kirtley, "A geometric interpretation of reference frames and transformations: dq0, clarke, and park," *IEEE Transactions on Energy Conversion*, vol. 34, no. 4, pp. 2070–2083, 2019.

[54] L. Parsa, *Performance improvement of permanent magnet AC motors*. PhD thesis, 2005. Copyright - Database copyright ProQuest LLC; ProQuest does not claim copyright in the individual underlying works; Last updated - 2021-05-20.

[55] H. Guzmán, M. Durán, and F. Barrero, "A comprehensive fault analysis of a five-phase induction motor drive with an open phase," in *2012 15th International Power Electronics and Motion Control Conference (EPE/PEMC)*, pp. LS5b.3–1–LS5b.3–6, 2012.

[56] J.-R. Fu and T. Lipo, "Disturbance-free operation of a multiphase current-regulated motor drive with an opened phase," *IEEE Transactions on Industry Applications*, vol. 30, no. 5, pp. 1267–1274, 1994.

[57] D. T. Vu, *Commande tolérante aux défauts des entraînements de machines synchrones à aimants permanents polyphasées non-sinusoïdales sous contraintes de courant et de tension pour les applications automobiles*. PhD thesis, 2020. Thèse de doctorat dirigée par Semail, Éric et Nguyen, Ngac Ky Génie électrique (AM) Paris, HESAM 2020.

[58] H. Qiu-Liang, C. Yong, and X. Li, "Fault-tolerant control strategy for five-phase pmsm with third-harmonic current injection," *IEEE Access*, vol. 6, pp. 58501–58509, 2018.

[59] M. J. Duran and F. Barrero, "Recent advances in the design, modeling, and control of multiphase machines—part ii," *IEEE Transactions on Industrial Electronics*, vol. 63, no. 1, pp. 459–468, 2016.

[60] G. Liu, Z. Lin, W. Zhao, Q. Chen, and G. Xu, "Third harmonic current injection in fault-tolerant five-phase permanent-magnet motor drive," *IEEE Transactions on Power Electronics*, vol. 33, no. 8, pp. 6970–6979, 2018.

[61] D. T. Vu, N. K. Nguyen, and E. Semail, "An overview of methods using reduced-ordered transformation matrices for fault-tolerant control of 5-phase machines with an open phase," in *2019 IEEE International Conference on Industrial Technology (ICIT)*, pp. 1557–1562, 2019.

[62] C. Xiong, H. Xu, T. Guan, and P. Zhou, "Fault-tolerant foc for five-phase spmsm with non-sinusoidal back emf," *IET Electric Power Applications*, vol. 13, no. 11, pp. 1734–1742, 2019.

[63] S. Dwari and L. Parsa, "Fault-tolerant control of five-phase permanent-magnet

motors with trapezoidal back emf," *IEEE Transactions on Industrial Electronics*, vol. 58, no. 2, pp. 476–485, 2011.

[64] D. T. Vu, N. K. Nguyen, E. Semail, and T. J. dos Santos Moraes, "Control strategies for non-sinusoidal multiphase pmsm drives in faulty modes under constraints on copper losses and peak phase voltage," *IET Electric Power Applications*, vol. 13, no. 11, pp. 1743–1752, 2019.

[65] H. Guzman, M. J. Duran, F. Barrero, L. Zarri, B. Bogado, I. Gonzalez Prieto, and M. R. Arahal, "Comparative study of predictive and resonant controllers in fault-tolerant five-phase induction motor drives," *IEEE Transactions on Industrial Electronics*, vol. 63, no. 1, pp. 606–617, 2016.

[66] H.-M. Ryu, J.-W. Kim, and S.-K. Sul, "Synchronous-frame current control of multiphase synchronous motor under asymmetric fault condition due to open phases," *IEEE Transactions on Industry Applications*, vol. 42, no. 4, pp. 1062–1070, 2006.

[67] M. Trabelsi, E. SEMAIL, and N. K. Nguyen, "Experimental Investigation of Inverter Open-Circuit Fault Diagnosis for Bi-Harmonic Five-Phase Permanent Magnet Drive," *IEEE Journal of Emerging and Selected Topics in Power Electronic*, p. 13, 2017.